

DETERMINATION OF RESIDUAL STRESS STATE IN SAE/AISI 8620
CARBURIZED STEEL BY NON-DESTRUCTIVE TESTING METHODS

A THESIS SUBMITTED TO
THE GRADUATE SCHOOL OF NATURAL AND APPLIED SCIENCES
OF
MIDDLE EAST TECHNICAL UNIVERSITY

BY

TUĞÇE KALELİ

IN PARTIAL FULFILLMENT OF THE REQUIREMENTS
FOR
THE DEGREE OF MASTER OF SCIENCES
IN
METALLURGICAL AND MATERIALS ENGINEERING

JANUARY 2017

Approval of the thesis:

**DETERMINATION OF RESIDUAL STRESS STATE IN SAE/AISI 8620
CARBURIZED STEEL BY NON-DESTRUCTIVE TESTING METHODS**

Submitted by **TUĞÇE KALELİ** in partial fulfillment of the requirements for the degree of **Master of Science in Metallurgical and Materials Engineering Department, Middle East Technical University** by,

Prof. Dr. Gülbin Dural Ünver
Dean, Graduate School of **Natural and Applied Sciences**

Prof. Dr. C. Hakan Gür
Head of Department, **Metallurgical and Materials Engineering**

Prof. Dr. C. Hakan Gür
Supervisor, **Metallurgical and Materials Eng. Dept., METU**

Examining Committee Members:

Prof. Dr. Tayfur Öztürk
Metallurgical and Materials Engineering Department, METU

Prof. Dr. C. Hakan Gür
Metallurgical and Materials Engineering Department, METU

Assist. Prof. Dr. Kemal Davut
Metallurgical and Materials Eng. Dept., Atılım University

Prof. Dr. Cevdet Kaynak
Metallurgical and Materials Engineering Department, METU

Assist. Prof. Dr. Mert Efe
Metallurgical and Materials Engineering Department, METU

Date: 30.01.2017

I hereby declare that all information in this document has been obtained and presented in accordance with academic rules and ethical conduct. I also declare that, as required by these rules and conduct, I have fully cited and referenced all material and results that are not original to this work.

Name, Last name: Tuğçe Kaleli

Signature :

ABSTRACT

DETERMINATION OF RESIDUAL STRESS STATE IN SAE/AISI 8620 CARBURIZED STEEL BY NON-DESTRUCTIVE TESTING METHODS

Kaleli, Tuğçe

M.Sc., Department of Metallurgical and Materials Engineering

Supervisor: Prof. Dr. C. Hakan Gür

January 2017, 147 Pages

Industrial performance of the carburized steels is mainly dependent on the residual stress state in the carburized layer that is controlled by the process parameters such as carburizing temperature and time. Non-destructive evaluation of the material properties and residual stress state has been gained importance for industrial applications due to its advantages such as measurement speed and complete control possibility of the components by automation. The aim of this thesis is to investigate the efficiency of magnetic Barkhausen noise (MBN) method for determining the residual stresses and monitoring variations in residual stress state in AISI/SAE 8620 steel. For this purpose, MBN measurements were performed to observe residual stress state on a series of samples prepared by changing carburizing time and tempering temperature, and then, the results were compared with those of X-ray diffraction methods. Microstructural examinations and micro hardness values were also investigated to analyze the results of the measurements. Increase in the carburizing time up to critical level caused to increase the compressive residual stresses in the carburized layer that is detected as a reduction in MBN emission. Moreover, it was observed that changing tempering temperature causes the change in the martensite

morphology and different stress relaxation levels. A clear relationship has been observed between residual stresses and MBN signals.

Keywords: Carburizing, Residual Stresses, Non-Destructive Evaluation, Magnetic Barkhausen Noise, X-Ray Diffraction

ÖZ

SEMENTE EDİLMİŞ AISI/SAE 8620 ÇELİĞİNDEKİ KALINTI GERİLİM DURUMUNUN TAHRİBATSIZ MUAYENE YÖNTEMLERİ İLE BELİRLENMESİ

Kaleli,Tuğçe

Yüksek Lisans, Metalurji ve Malzeme Mühendisliği Bölümü

Tez Yöneticisi: Prof. Dr. C. Hakan Gür

Ocak 2017, 147 Sayfa

Semente edilmiş çeliklerin kullanım performansı, sementasyon sıcaklığı ve süresi gibi işlem parametreleriyle kontrol edilebilen sementasyon katmanındaki kalıntı gerilmelerin durumuna bağlıdır. Kalıntı gerilim durumunun ve bazı malzeme özelliklerinin saptanmasında tahribatsız muayene yöntemlerinin kullanılması, ölçüm hızından ve otomasyon ile parçanın tamamının kontrol edilmesine olanak sağlamasından kaynaklı endüstriyel uygulamalarda oldukça önem kazanmıştır. Bu çalışmanın amacı Manyetik Barkhausen Gürültüsü (MBN) yönteminin kalıntı gerilmelerin ölçülmesindeki etkinliğini ve güvenilirliğini incelemek ve sementasyon parametrelerindeki değişimlerin AISI/SAE 8620 çeliğindeki kalıntı gerilme durumuna olan etkilerini gözlemlemektir. Bu amaçla, sementasyon süresi ve menevişleme sıcaklığı değiştirilerek AISI/SAE 8620 çeliği numunelerinden MBN ölçümleri alınarak kalıntı gerilim durumları gözlemlenmiş ve elde edilen sonuçlar X-ışını kırınımı yöntemi ile karşılaştırılmıştır. Ayrıca, menevişleme sıcaklığındaki değişimlerin martensit morfolojisinin değişmesine ve farklı gerilim giderme durumlarına neden olduğu gözlemlenmiştir. Elde edilen sonuçların analiz edilmesi için numunelerin içyapıları da incelenmiş ve mikro sertlik ölçümleri alınmıştır.

Sementasyon süresindeki artış yüzeyde basma yönündeki kalıntı gerilim miktarının artmasına sebep olmuş ve buna bağlı olarak Barkhausen sinyallerinin aktivitesini azaltmıştır. Kalıntı gerilme ve MBN sinyalleri arasında belirgin bir ilişki gözlenmiştir.

Anahtar Kelimeler: Sementasyon, Kalıntı Gerilimler, Tahribatsız Muayene, Manyetik Barkhausen Gürültüsü, X-ışını Kırınımı

To My Family

ACKNOWLEDGEMENTS

Firstly, I would like to express my deepest gratitude to my supervisor Prof. Dr. C. Hakan Gür for his guidance, understanding and continuous support throughout the study.

I would like to thank Dr. Süha Tirkeş for all his help and guidance throughout the study.

My special thanks go to Assist. Prof. Dr. Caner Şimşir for introducing me with the concept of X-Ray Diffraction residual stress measurements and Assist. Prof. Dr. Kemal Davut for helping in the MBN measurements for those from the Metal Forming Center of Excellence, Atilim University (MFCE).

I would like to thank Zeynep Öztürk for XRD measurements, Dr. Caner Batıgün for construction of CCT diagrams by JMATPRO software, Dr. İbrahim Çam for introducing me with the concept of MBN and helping with the measurements, Türk Traktör Company for manufacturing of the carburized samples, and METU Central Laboratory for the MBN measurements.

I would like to thank to my colleagues H. İlker Yelbay, Hüseyin Hızlı, Orcan Kolankaya, Seyhan Çamlıgüney, Başak Güneş Orhan, Koray Yurtışık, Burcu Anık, Murat Tolga Ertürk and Göksu Gürer from METU WTNDT / Nondestructive Testing Unit for their help, support and interest.

I would also like to thank Mert Alay, Berfu Göksel and Aykut Buğra Çetin for giving me the strength to finish my degree by sharing all the good and the bad times.

I wish to express my gratitude to my parents Muazzez and Mevlüt Kaleli for all that I am and to my sisters Nagehan Kaleli Demir, Neslihan Kaleli Dalkıran, Efsun Ülküm Kaleli. I would also like to thank to my brothers Mustafa Erkin Demir and Özgür Dalkıran for their continual support and encouragement.

Finally, I would like to thank to my little prince Ömer Kağan Demir and Princess Umay Dalkıran for giving me the magical motivation and their pure love beyond words and to teach me what endless love is.

TABLE OF CONTENTS

ABSTRACT.....	v
ÖZ	vii
ACKNOWLEDGEMENTS	x
TABLE OF CONTENTS	xi
LIST OF TABLES	xv
LIST OF FIGURES	xvi
NOMENCLATURE.....	xxi
CHAPTERS	1
1. INTRODUCTION	1
1.1. General	1
1.2. Aim of the Study	3
2. THEORY	5
2.1. Heat Treatment of Steels	5
2.1.1. Surface Treatments; Carburizing.....	8
2.1.1.1. Gas Carburizing	10
2.2. Tempering of Steels	18
2.3. Residual Stresses	19
2.3.1. Definition of Residual Stress.....	19
2.3.2. Formation of Residual Stresses during Carburizing.....	21
2.4. Measurement Techniques of Residual Stresses	27
2.4.1. Theory of X-ray Diffraction Method.....	29

2.4.2. Theory of Magnetic Barkhausen Noise Method.....	35
2.5. Magnetic Barkhausen Noise Method	36
2.5.1. Introduction to Magnetic Materials.....	36
2.5.2. Hysteresis Curves.....	38
2.5.3. Barkhausen Effect	42
2.5.4. Magnetic Barkhausen Noise (MBN) Measurement Techniques.....	43
2.5.5. The Factors Affecting the MBN Emission.....	47
2.5.5.1. The Effects of Microstructure	48
2.5.5.2. The Effects of Stress State	51
2.5.5.3. The Effects of Hardness	53
2.5.6. Residual Stress Measurement by MBN Method.....	54
3. LITERATURE REVIEW.....	57
3.1. Effect of Carburizing Parameters on RS.....	57
3.2. Characterization of Stress State by Non-Destructive Methods.....	62
3.3. Effect of Microstructure on MBN.....	64
3.4. Effect of Hardness on MBN.....	66
3.5. Effect of Stress State on MBN	67
4. EXPERIMENTAL PROCEDURE	69
4.1. Material Selection and Sample Preparation	69
4.2. Heat Treatment Processes	70
4.3. Residual Stress Measurements	73
4.3.1. Magnetic Barkhausen Noise (MBN) Method	73
4.3.2. X-Ray Diffraction (XRD) Method.....	78

4.4. Metallographic Examination	80
4.5. Hardness Measurements.....	81
5. RESULTS AND DISCUSSION	83
5.1. Microstructural Results	83
5.2. Case Depth Analysis	93
5.2.1. Depth Profile of Carbon Content.....	93
5.2.2. Depth Profile of Micro-Hardness	94
5.2.3. Depth Profile of Residual Stresses	98
5.3. Residual Stress State Analysis	101
5.3.1. XRD Results.....	101
5.3.2. MBN Measurement Results	104
5.3.2.1. Rollscan Results.....	104
5.3.2.1.1. MBN Residual Stress vs XRD Residual Stress	114
5.3.2.2. μ Scan Results.....	116
5.3.2.2.1. RMS Results of Signal Envelope.....	116
5.3.2.2.2. Hysteresis Curves.....	119
6. CONCLUSION	125
6.1. Recommendation for Further Studies	127
REFERENCES.....	129
APPENDIX.....	139
A. CCT DIAGRAMS OBTAINED BY JMATPRO SOFTWARE.....	139
B. SCANNING ELECTRON MICROSCOPE IMAGES	142

C. CORRELATION AMONG RMS, HARDNESS, MBN AND RESIDUAL STRESS.....	145
D. CALCULATION OF MAGNETIC PERMABILITY AND INFORMATION DEPTH OF MBN MEASUREMENTS	147

LIST OF TABLES

TABLES

Table 4. 1 Chemical composition of the SAE/AISI 8620 steel used (wt %)	69
Table 4. 2 Coding system of the specimens	72
Table 4. 3 Calibration sample database for XRD measurement	79
Table 5. 1 Average micro-hardness value of core and case regions of the heat-treated samples	96
Table 5. 2 XRD residual stress measurement results three phi angles; 0°,45° and 90°	102
Table 5. 3 Raw MBN emission values for different measurement directions at the surface with standard deviation	107
Table 5. 4 Residual stress values of specimens converted from MBN emission parameter by using calibration curves	114
Table 5. 5 Remanence, coercivity and differential permeability values of the carburized (900°C) and tempered AISI/SAE 8620 steel specimens	123
Table D 1 Electrical and magnetic properties of normalized and carburized (900°C/12 hrs) AISI/SAE 8620 steel specimens	147

LIST OF FIGURES

FIGURES

Figure 2. 1 Fe-C phase diagram demonstrated to solubility of carbon in austenite phase regions of different steel grades	9
Figure 2. 2 Schematic demonstration of carburizing process	10
Figure 2. 3 Schematic demonstrations of the stages of carburizing process; mass transformation of carbon in the gaseous environment, chemical reaction at the interphase and diffusion of carbon in the austenite β is used as the mass transfer coefficient of carbon and D_c indicates the diffusion coefficient of carbon in austenite	11
Figure 2. 4 Representative CCT diagram of AISI/SAE 8620 Steel with the average grain size ASTM 9 and austenitized at 880°C	17
Figure 2. 5 Relationships between residual stress and several factors	20
Figure 2. 6 Demonstration of two possible cooling case during quenching of carburized specimens	22
Figure 2. 7 Demonstration of the residual stress evolution gradually for the Case I ; cooling rate of the surface is enough to obtain martensitic transformation, but core of the specimen does not show	25
Figure 2. 8 Demonstration of the residual stress evolution gradually for the Case II; the differences in cooling rate of the surface and core is not high.....	26
Figure 2. 9 Demonstration of residual stress measurement method with respect to penetration depth, spatial resolution	28
Figure 2. 10 Schematic of X-ray diffraction paths and peak position (a) unstrained state and (b) under tensile strain due to an applied load	31
Figure 2. 11 Demonstration of S_i (sample coordinate system) and L_i (laboratory coordinate system).....	31
Figure 2. 12 Schematic demonstration of domains in the ferromagnetic materials and the domain wall alignments	37

Figure 2. 13 Representative hysteresis curve of magnetized samples that shows the both reversible and irreversible magnetization behavior together	40
Figure 2. 14 Examples of comparison between hysteresis curves of soft and hard magnetic materials a)ASTM 410 Stainless Steel b)ASTM 4340	41
Figure 2. 15 Schematic demonstration of Barkhausen jumps with high-resolution examination	43
Figure 2. 16 Schematic demonstration of Barkhausen sensor and measurement set-up	44
Figure 2. 17 Analyzed parameters from μ Scan software a) amplitude spectrum b)MBN fingerprint c) frequency spectrum d) Pulse Height Distribution.....	47
Figure 2. 18 Representative demonstration of interaction between domain wall and inclusions and passage of the domain wall	49
Figure 2. 19 The MBN RMS value as a function of applied magnetic field with different microstructures	51
Figure 2. 20 The relationship of MBN signal level under tensile and compressive stresses for the positive magnetostrictive materials	53
Figure 3. 1 The relationships between the carburizing time and temperature and the total case depth.....	59
Figure 3. 2 The relationship between stress and case depth in carburized steel which has 0,2%C, 0,77%Cr, 0, 7 %Ni and 0,0 5 7% Mo. 0,8%C in the surface	60
Figure 3. 3 Tangential residual stresses of a carburized cylinder quenched from 927°C in oil at 20°C.; comparison between experimentally determined and calculated tangential residual stresses.	62
Figure 3. 4 Calibration curves for various steel types showing the relationship between MBN emission and compressive/tensile stress	64
Figure 4. 1 The specimen for calibration with the standard geometry stated in ASTM E8-E8M.....	70
Figure 4. 2 MBN emission parameter distribution for five different positions	73
Figure 4. 3 Magnetic saturation curves for the calibration of process parameters	74

Figure 4. 4 MBN measurement system; a)The Stresstech Rollscan μ Scan 500-2 device Magnetic Barkhausen Noise Equipment b) Probe has more powerful magnetization ability.....	75
Figure 4. 5 Schematic demonstration of MBN measurement positions.....	76
Figure 4. 6 Schematic demonstration of calibration tensile/compressive loading test specimen and the position of the strain gauges and barhausen coil relatively.....	77
Figure 4. 7 XStress 3000 G2/G2R Systems	78
Figure 5. 1 Optical micrographs (1000X) taken from core region of the samples	85
Figure 5. 2 Optical micrographs (1000X-500X-250X, respectively) taken from case region of the samples.....	86
Figure 5. 3 Optical micrographs (1000X) taken from case region of the carburized (900°C/5hrs) samples after tempering at 180°C for 3 hrs.	88
Figure 5. 4 Optical micrographs (1000X) taken from case region of the carburized (900°C/5hrs) samples after tempering at 240°C for 3 hrs.	89
Figure 5. 5 Optical micrographs (1000X) taken from case region of the carburized (900°C/5hrs) samples after tempering at 600°C for 3 hrs.	89
Figure 5. 6 Optical micrographs (2800X) taken from core region of the carburized (900°C/5hrs) samples after tempering at 180°C for 3 hrs.	90
Figure 5. 7 Optical micrographs (2800X) taken from core region of the carburized (900°C/5hrs) samples after tempering at 240°C and 600°C for 3 hrs.	90
Figure 5. 8 Optical micrographs (1000X) taken from case and core region of the carburized (900°C/9hrs) samples after tempering at 180°C, 240°C and 600°C for 3 hrs.	91
Figure 5. 9 Optical micrographs (1000X) taken from case and core region of the carburized (900°C/12hrs) samples after tempering at 180°C, 240°C and 600°C.....	92
Figure 5. 10 Variation of depth profile of % C in SAE/AISI 8620 steel with carburizing time at 900°C.....	94
Figure 5. 11 Variation of depth profiles of hardness in SAE/AISI 8620 steel with carburizing time at 900°C	95

Figure 5. 12 Depth profiles of the effective RS obtained by XRD method for the carburized AISI/SAE 8620 steel at 900°C for different carburizing times (5, 9 and 12 hrs)	100
Figure 5. 13 d vs. $\sin^2\psi$ curve fitted to the diffraction data of $\Phi=0^\circ$ (900°C/5hrs carburized sample)	102
Figure 5. 14 Effects of carburizing time and tempering temperature on the surface residual stress of the ca SAE/AISI 8620 samples	104
Figure 5. 15 Effect of carburizing time at 900°C on the average MBN activity for AISI/SAE 8620 steel (different measurement directions at the surface)	108
Figure 5. 16 Effect of tempering temperature on the Average MBN activity for the carburized AISI/SAE 8620 steel (900°C/5hrs)	108
Figure 5. 17 Effect of tempering temperature on the Average MBN activity for the carburized AISI/SAE 8620 steel (900°C/9hrs)	109
Figure 5. 18 Effect of tempering temperature on the Average MBN activity for the carburized AISI/SAE 8620 steel (900°C/12hrs)	109
Figure 5. 19 MBN vs stress calibration curves of carburized AISI/SAE 8620 steel specimen (900°C/5, 9, 12hrs).....	112
Figure 5. 20 MBN vs stress calibration curves of carburized and tempered AISI/SAE 8620 steel specimens (900°C/5hr)	112
Figure 5. 21 MBN vs stress calibration curves of carburized and tempered AISI/SAE 8620 steel specimen (900°C/ 9 hrs)	113
Figure 5. 22 MBN vs stress calibration curves of carburized and tempered AISI/SAE 8620 steel specimen (900°C/12hrs)	113
Figure 5. 23 Comparison of the residual stress values obtained by MBN and XRD methods.	115
Figure 5. 24 RMS signal envelope of normalized and carburized specimens	118
Figure 5. 25 RMS signal envelope of the carburized and tempered specimens	118
Figure 5. 26 Representative hysteresis curves of the specimens	119

Figure 5. 27 Representative hysteresis curves of the carburized (900°C/5hr) and tempered specimens	121
Figure 5. 28 Representative hysteresis curves of the carburized (900°C/9hr) and tempered specimens	122
Figure 5. 29 Representative hysteresis curves of the carburized (900°C/12hr) and tempered specimens	122
Figure A. 1 Simulated a) CCT diagram and b) phase % vol. distribution diagram of 5 hour-carburized specimens.....	139
Figure A. 2 Simulated a) CCT diagram and b) phase % vol. distribution diagram of 9 hours-carburized specimens	140
Figure A. 3 Simulated a) CCT diagram and b) phase % vol. distribution diagram of 12 hours-carburized specimens	141
Figure B 1 SEM micrographs of carburized samples (900°C/5hrs) that were tempered at different temperature for 3 hrs.....	142
Figure B 2 SEM micrographs of carburized samples (900°C/9hrs) that were tempered at different temperature for 3 hrs.....	143
Figure B 3 SEM micrographs of carburized samples (900°C/12hrs) that were tempered at different temperature for 3 hrs.....	144
Figure C 1 Correlation between relative RMS values of MBN measurements and Hardness values taken from the same position	145
Figure C 2 Correlation between relative RMS values of MBN Residual Stress measurements taken from the same position.....	146

NOMENCLATURE

ABBREVIATIONS

RS	Residual Stresses
MBN	Magnetic Barkhausen Noise
XRD	X-Ray Diffraction
BN	Barkhausen Noise
NDT	Non-Destructive Testing
HV	Vickers Hardness
ND	Normal Direction
RMS	Root Mean Square
SEM	Scanning Electron Microscopy
OES	Optical Emission Spectrometer
CHD	Case Hardened Depth
FWHM	Full-Width Half Maximum
TTT	Time-Transformation Temperature
CCT	Continuous Cooling Transformation

SYMBOLS

N	Normalizing heat treatment
C	Carburizing heat treatment
T	Tempering temperature [$^{\circ}\text{C}$]
f	Magnetizing frequency [Hz]
V_{pp}	Magnetizing voltage [Volts]
B	Magnetic flux [Weber]
H	Applied magnetic field [A/m]
H_c	Coercivity [A/m]
H_s	Saturation magnetization [A/m]
B_r	Remanence [Weber]
M_s	Martensite start temperature [$^{\circ}\text{C}$]
M_f	Martensite finish temperature [$^{\circ}\text{C}$]
D_c	Diffusion coefficient of carbon in austenite [m^2/s]
C_x	Carbon concentration as a function of distance from the surface [% weight]
C_o	Initial carbon content of steel [% weight]
C_s	Surface carbon concentration [% weight]
P	Partial pressure of the species [Pa]
K	Equilibrium constant

L_i	Laboratory coordinates system
S_i	Simple coordinate system
E	Elastic Modulus [GPa]
hkl	Miller indices
a_c	Activity of carbon
d	Distance between diffracting lattice planes [Å]

GREEK LETTERS

μ	<i>Permeability [N/A⁻²]</i>
μ_r	<i>Relative permeability</i>
μ_0	<i>Permeability of vacuum [N/A⁻²]</i>
δ	<i>Penetration depth of Barkhausen noise signal [μm]</i>
σ	<i>Conductivity of a material under test [ohm]</i>
λ	<i>X-ray wavelength [Å]</i>
Θ_B	<i>Bragg's angle [°]</i>

CHAPTER 1

INTRODUCTION

1.1. General

In industry, all engineering components are exposed to different service conditions. These service conditions play an important role in service life of them that defines as the resistance to failure under severe service conditions. The failure of engineering structure is caused by external loads, and residual stress state should be responsible for this. Hence, the residual stress should be taken into account as much as external loads.

Any manufacturing process introduces a residual stress that may cause either positive or negative effect. There is an increasing interest in how the state of residual stress changes the mechanical properties and structure of a material. For instance, compressive residual stress at the surface improves fatigue performance while tensile residual stress will increase the tendency for stress corrosion cracking in a corrosive environment. Especially, fatigue performance of the machine parts is very important for the service life of them. It is mainly related to surface conditions since fatigue failures are initiated from the surface or near surface cracks and these cracks propagate to the interior part of components. Then the failure occurs when they have reached the critical length. Generally, the external and/or internal tensile loads cause the crack initiation and enhance the crack propagation. Under these service conditions,

probability of catastrophic failures at the early stage of service life is increased. This causes deterioration in the mechanical performance of the component.

Residual stresses have been gained an importance for the design and production of engineering components to obtain sufficient reliability and increase service life of them. They are defined as self-equilibrating stresses. In other words, they are local areas of tensile and compressive residual stresses and they corresponds each other to create zero force and moment within the bulk material. They can be formed during the each step of the production. Metallurgical and mechanical history of the part during its manufacture is quite critical to control magnitude and type of the residual stresses. Therefore, residual stress has to be taken into account to make the component safe and reliable and its value must be controlled and measured accurately.

Measurement of the residual stresses has been applied by using various methods from past to present. These methods can be destructive or nondestructive. Each method has some advantages and limitations. Non-destructive evaluation of the material properties has become more of an issue for industrial applications due to its advantages such as measurement speed and 100% control possibility of the components by automation. The most common and accurate nondestructive technique is based on the diffraction characteristics of x-rays which is called X-Ray Diffraction (XRD). It accurately determines the residual stress; however, measurement from the single point takes long time and may have limitations in the field measurements. Hence, easy, quick and reliable nondestructive techniques have been investigating in industry. Nowadays, it has been found that micro-magnetic techniques can be an alternative way to determine residual stress quickly in ferromagnetic steels. The most popular and important technique is Magnetic Barkhausen Noise (MBN) technique that is based on the movement of ferromagnetic domains in the material. Transportability, short exposure

times, and the ability to work under severe environmental conditions are the main advantages of this technique. On the other hand, the utilization of this technique is restricted with the unknown parameters since obtained data do not give the actual stress state without calibration [1].

1.2. Aim of the Study

Carburizing is a special surface treatment method that provides the compressive residual stress layer to the surface. By changing the carburizing process parameters, the depth of this layer can be controlled and service life can be optimized. Hence, monitoring the residual stress state and controlling the case depth in the carburized components are vital to guarantee the service life and the performance demands of industrial components.

Recently, expectations from the nondestructive methods for residual stress measurement have being increased in industry. For example, producers have demanded the reduction in testing time and increase in the ability to automatization. For this reasons, in addition to XRD method, MBN technique has been gained an importance for residual stress characterization because it is cheap, fast, transportable and usable in severe environmental conditions.

One of the aim of this study is to control the case depth of carburized component by changing the critical process parameters such as carburizing time, temperature and then to monitor the created compressive residual stress level, which provides the improvement of the service life. Moreover, the quality and homogeneity of carburizing process will be controlled quickly by MBN method. The other and more important aim

is to investigate the feasibility of MBN technique in order to monitor the residual stress level with the high accuracy.

CHAPTER 2

THEORY

2.1. Heat Treatment of Steels

Most of the engineering components require special functional properties such as electrical, optical, physical, chemical, and mechanical. Especially mechanical properties are quite important for the industry in order to control the service life of component. Industrial applications have gain an importance and become more complicated, in the meantime, engineering materials should have also developing continuously. Heat treatment represents the technically attractive method to improve the intended mechanical properties of the materials by applying specific thermal process. This phenomenon adjusts the functional mechanical properties by controlling microstructures of materials.

Heat treatment processes are most commonly applied to the metals and alloys. In industry, commonly used material is steel which is defined as an alloy of iron and carbon with the carbon content up to about %2 [3]. The properties of the steel undergo the most dramatic increase when they are thermally treated. Therefore structural changes in iron–carbon alloys should be considered well [2].

To understand heat treatment mechanisms of metals, crystal structures and phases of metals should be comprehended. The basis of heat treatments of steels is related to the phase diagram of Fe-C. From the well-known Fe-C phase diagram, stable phases at

the certain temperature under one atmosphere pressure can be determined for the equilibrium cooling conditions. As observed in the equilibrium phase diagram of steel, different phases exist at different temperature and %C conditions; austenite (γ), ferrite (α), δ -ferrite, cementite (Fe_3C). However, under the non-equilibrium cooling conditions, different metastable phases form in the steel microstructures; martensite, bainite. In this case, Time-Temperature-Transformation (TTT) or Continuous Cooling Transformation (CCT) diagrams should be used rather than the equilibrium Fe-C phase diagram. In these diagrams, martensite and bainite phase regions are indicated. In order to understand the hardening mechanisms of heat treatment processes, phase properties and phase transformation kinetics should be investigated carefully. Properties of the phases are mainly related to the atomic structures. The arrangement of atoms indicates the structure of the steel and this determines the physical, mechanical, electrical and even magnetic properties of steel. There are two common crystal structures in iron that are body-centered-cubic (BCC) and face-centered-cubic (FCC). FCC structure is denser than BCC structure. Austenite is stable phase at high temperature. Only austenite can transform into the other phases when temperature changes. Therefore, in the steel heat treatment, first thing is heating of the steel up to the austenite phase region where is started from the 50°C above eutectoid temperature. At this temperature level, the steel is maintained for the sufficient time to get homogeneous and fully austenitic microstructure. Then, the steel is cooled down to the room temperature with different cooling rates that are chosen in respect to desired microstructures. Cooling rate is adjusted by using different cooling media such as furnace atmosphere, air, oil, liquid salt. When the heated steel cools down to room temperature in the furnace atmosphere with the cooling rate of about $20^\circ\text{C}/\text{hr}$, this process is called annealing. On the other hand, cooling in air atmosphere with natural convection is known as normalizing. Annealing provides mechanically softer material than that of the normalized material since microstructure of annealed component includes the coarser pearlite ($\alpha+\text{Fe}_3\text{C}$) and ferrite phases. However, phases in microstructures of normalized steels become finer due to the phase transformation kinetics that is

controlled by diffusion mechanisms. Faster cooling rate allows finer lamellar and smaller ferrite grains due to the limited time to growth mechanism. A pearlitic structure is relatively soft with low physical properties. If the steel is cooled very rapidly, a very hard and strong structure forms. It is called martensite, which is a metastable phase of dissolved carbon in iron.

In heat treatment applications, one of the most important phases is martensite since it is the mechanically hardest structure. Unlike to the ferritic and pearlitic transformation, martensitic transformation from austenite phase is controlled by shear-like diffusionless mechanism, which leads severe elastic strains in both the martensite and surrounding austenite matrix [4]. It has a tetragonal body-centered lattice with interstitial carbon atoms in solid solution. Moreover, it has a high dislocation density that is formed during shear type of transformation mechanism. Martensite is a supersaturated solid solution of carbon in ferrite matrix. During the transformation, thermodynamically preferred phase is ferrite; however, there is no enough time to occur the diffusional transformation. Instead of it, transformation kinetics allows to diffusionless shear transformation to create the new phases. The carbon atoms tend to order in such a way that the crystal structure change from body-centered cubic to body centered tetragonal. The tetragonality is measured by the ratio between the axes, c/a , and it increases with carbon content. The tetragonality of martensite arises as a direct result of interstitial solution of carbon atoms in the bcc lattice, together with the preference for a particular type of octahedral site imposed by the diffusionless character of the reaction [5]. Both lattice distortion and interstitial solid solution cause to strengthen the material.

2.1.1. Surface Treatments; Carburizing

There are several types of heat treatment methods. Thermochemical surface treatment is one kind of heat treatment processes. It is also called as case hardening. Case hardening is the special kind of engineering application that represents the technically attractive and economically viable technique in order to create the superficial layer of materials. The objective of case hardening is to improve material surface properties such as wear resistance, hardness, strength. The surface properties are different from those of the interior part of the base material. The combination of hard surface and tough interior material have been preferred in the ring gear since it should have hard surface to resist wear, along with a tough interior to resist the failure under impact loading conditions. Moreover, the surface hardening of steel is more economical method than through hardening since less expensive low-carbon or medium carbon steels could be used in surface hardening without any cracking problems. Thermochemical case hardening could be achieved by different methods; nitriding, carbonitriding and carburizing.

Carburizing is most widely used surface treatment method due to its low cost and easier applicability. Similar to other thermochemical heat treatment methods, it is based on the variation of the surface composition by diffusion of carbon until the desired depth from the surface. The carburizing process is made up of two steps: *carbon diffusion*, which is accompanied by the carbon gradient between the core and case, and *quenching*, which provides the hardness difference in the core and case. As a result of these two steps, *residual stresses* are created [6].

During carburizing, the steel is exposed to an environment that has high carbon activity. The environment can be gaseous, liquid or solid form. The steel is heated up to certain temperature range at which the microstructure is composed of only austenite. It is the range between typically 880-930°C, and maintained at there for several hours

in order to obtain homogeneous austenitic microstructure. The temperature range depends on the solubility of carbon in austenite indicated in Fe-C phase diagram. The solubility range of carbon in austenite is 0.8%C at the eutectoid temperature and 2.0%C at the eutectic temperature shown in Figure 2. 1. As it is understood from this diagram, maximum surface carbon content is limited to the solubility of carbon in the austenite at certain temperature. Different steel grades can change the solubility range (Figure 2. 1). Moreover, carburizing temperature influences the solubility limit of carbon in austenite. If the increase in solubility of carbon is wanted, temperature should be increased. Typically, the carburizing is done in two stages. In the initial stage, steel is heated up to elevated temperature and the carbon potential is maintained at a level that is close to the solubility limit of carbon in austenite. At the second stage, carbon potential of the atmosphere is decreased to a level that provides to maintain surface carbon potential ranging between 0.8 and 0.9%C. At this stage, carbon is liberated from carbon-rich source and the liberated carbon dissolves in the austenite and diffuses into the surface of steel, shown in Figure 2. 2. The two-step process is often referred to as boost-diffuse carburizing [8,9].

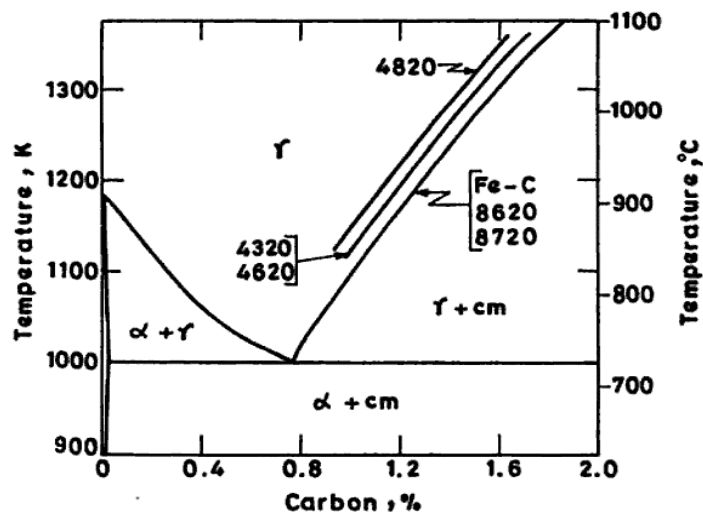


Figure 2. 1 Fe-C phase diagram demonstrated to solubility of carbon in austenite phase regions of different steel grades [7].

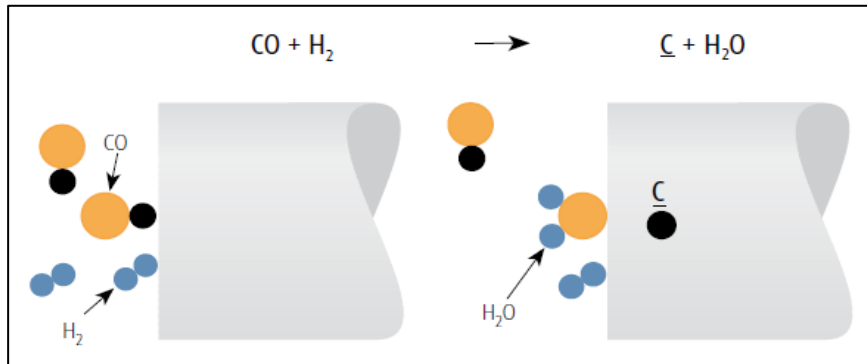


Figure 2. 2 Schematic demonstration of carburizing process

2.1.1.1. Gas Carburizing

Soaking of carbon into the surface of low carbon steel is aimed during carburizing. For this reason, special environments, which have higher carbon activity than that of the surface of the related steel, should be used to create higher carbon concentration on the surface of the steel. This situation is achieved by embedding the liberated carbon into the surface of the steel. The liberated carbon atoms are originated from the reactions of chemical species in the environments and they diffuse into the steel. The used environments can be the gas (atmospheric-gas, plasma, and vacuum carburizing), the liquids (salt bath carburizing), or the solid compounds (pack carburizing). Each of them has some disadvantageous and advantages. The most commonly used one is gas carburizing for large-scale production because the effects of process parameters are understood very well and control of them is easier [10]. To control and model the carburizing process, three parameters should be determined carefully; carburizing time, temperature and atmosphere composition. These are major process parameters. In addition to these, carburizing performance strongly depends on some secondary factors such as operating furnace type, chemical features of used materials, geometry of specimens, charging of furnace, specimen positions in the furnace during carburizing processes. Some of these parameters influence the kinetics of the process by contributing to either the mass transfer coefficient or carbon diffusivity in austenite

whereas some of them change the metallurgical phase transformation path thermodynamically. If the operating of well-controlled process is aimed, all of them must be investigated carefully.

Carbon is introduced into the iron structure by diffusion mechanism in order to create martensitic superficial layers [11]. This mechanism is strongly influenced by the process temperature and the used steel that determines the carbon diffusivity in the austenite phase. Three stages exist in the carburizing process when viewed from the aspects of the process kinetics; *mass transport of carbon* from atmosphere into the surface, *chemical reactions* at the gas-steel surface to get liberated carbon atoms and then *diffusion of the liberated carbon* in austenite phase of the steel (Figure 2. 3).

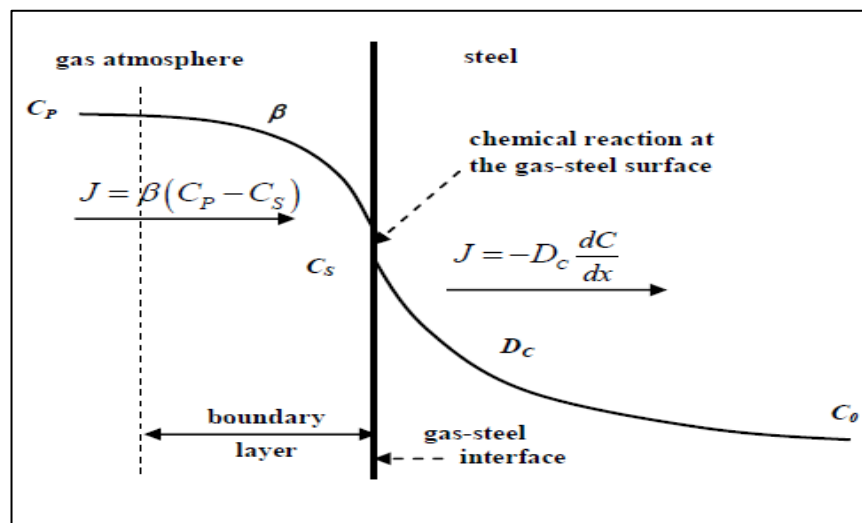


Figure 2. 3 Schematic demonstrations of the stages of carburizing process; mass transformation of carbon in the gaseous environment, chemical reaction at the interphase and diffusion of carbon in the austenite β is used as the mass transfer coefficient of carbon and D_c indicates the diffusion coefficient of carbon in austenite [13].

The first stage of carburizing is the mass transport of carbon in gaseous atmosphere. The second stage is the chemical reactions occurred at the gas-steel surface. From the thermodynamic point of view, chemical composition of furnace atmosphere and carburizing temperature should be chosen carefully to control the output of the carburizing process. In this technique, carbon-rich gaseous atmosphere is commonly used. The gaseous atmosphere is the mixture of carrier gas and enriching gas that is the main source of the carbon. The carrier gas is composed of endothermic carburizing atmospheres that is the blend of carbon monoxide, hydrogen, and nitrogen produced by interaction the hydrocarbon gas such as natural gas (primarily methane), propane, or butane with air [12]. When the carrier gas enters the heated furnace atmosphere, some reversible reactions take place;



In the above reactions, carbon monoxide (CO) and hydrogen (H₂) react with each other. Carbon (C) is deposited on the steel surface and then water vapor (H₂O) is formed. This reaction is rate-determining reaction since it is the fastest reaction. Moreover, decomposition of methane is the slowest one [14]. The furnace atmosphere must contain sufficient CO and H₂ to allow that the carburizing process proceeds in a uniform and reproducible fashion. Since the endogas is not sufficient to obtain large flow rate, the endothermic carrier gas is enriched by adding a hydrocarbon gas [15]. The purpose of the enriching gas is to react with CO₂ and H₂O;



Despite the enriching reactions (4) and (5) do not reach equilibrium, the efficiency of the process is decided by the atmosphere carbon potential obtained from these reactions. This carbon potential is controlled by the ratio of CO/CO₂, H₂/H₂O components and oxygen partial pressure in the heterogeneous water-gas reaction. Reaction (1) is resulted from the combination of reactions (5) and the reverse of the reaction (4). By examining reaction (1) carbon activity could be obtained by using Eq.1;

$$a_C = \frac{P_{CO}^2}{P_{CO_2}} * \exp\left(\frac{20530,65}{T} - 20,98\right) \quad \text{Eq. 1}$$

From the Eq. 1, the ratio of CO / CO₂, H₂ / H₂O could be calculated easily at certain temperature, as in the form of Kelvin (°K). On the other hand, carbon potential of atmosphere is quite important issue to achieve process quality. The definition of carbon potential (C_P) is the amount of carbon in the furnace atmosphere that is in thermodynamic equilibrium with the surface carbon content. The partial pressure of oxygen can also be used to monitor the carbon potential.

Once the CO molecules reach the surface and dissociate into adsorbed carbon atoms and carbon dioxide, the remained carbon atoms transport by diffusion-controlled mechanisms. As such, the diffusion coefficient of carbon in austenite is another parameter to decide the performance of process. Carbon diffusivity (*D*) in austenite varies with both carbon concentration and carburizing temperature [16]. Moreover, the steel grade and the alloying elements can affect the diffusivity of carbon in austenite because interstitial carbon diffusivity is strongly affected by the atomic interactions between interstitial carbon and substitutional solute [17, 18]. Although alloying elements significantly contribute the diffusivity of carbon in austenite, there is less

theoretical and experimental knowledge to decide the effect of alloying elements on the carbon diffusivity quantitatively. Hence, most applications assume that carbon diffusivity should be either constant at fixed temperature or changeable with carbon concentration only. In order to develop a basic analytical model to calculate the effect of steel type on the diffusion of carbon, it should be assumed that the diffusion direction is perpendicular to the surface. Moreover, the diffusion coefficients and component temperature should be accepted as constant if the carbon concentration changes [16, 19]. From the engineering point of view, proper modelling of these stages and selection of these parameters are quite important since they decide the desired mechanical properties after carburizing; the case hardness and effective case depth. Effective case depth is defined as the critical distance from the surface that shows the effective mechanical properties of hardened sample. The case depth of specimens is the function of the carbon concentration varying with time. It could be calculated by using following equations;

$$x = 2\sqrt{D_c t} \quad \text{Eq. 2}$$

where x is the case-depth, D_c is the diffusion coefficient of carbon in austenite and t is the carburizing time. The equation gives only time-dependent case depth. However, as mentioned earlier, the depth of case also depends on the concentration of the carbon on the surface. Hence, the case depth should be calculated precisely by using Fick's second law of diffusion as a function of time and distance;

$$\frac{c_x - c_s}{c_0 - c_s} = \text{erf} \left(\frac{x}{2\sqrt{D_c t}} \right) \quad \text{Eq. 3}$$

C_x is the carbon concentration, which is the function of the distance from the surface, C_s is the surface carbon concentration, C_0 is the initial carbon content of steel [16, 19, 20].

In the literature, the effective case depth is also determined from the carbon content or micro-hardness value taken from related distance. It is accepted that the steel that has 0.4 wt %C corresponds to approximately 50 HRC (500 HV) hardness values. The desired depth from the surface relies on the carburizing time that is mainly related to the diffusion of carbon in the austenite phase. Considering the carbon diffusivity in the austenite phase of related steel, optimum carburizing time can be selected with respect to the expected case depth [21].

Once the consideration of both thermodynamic and kinetic parameters, optimum carburizing parameters should be selected to accomplish the process properly. First consideration must be the adjustment of carburizing atmosphere in order to maintain constant surface carbon potential during process. It is generally obtained by mixing of $C_3H_8(g)$ and the shielding gas which is composed of 33 wt% H_2 , 28 wt% CO, 0,8 wt% CH_4 . From the thermodynamic and metallurgical standpoint, optimum-carburizing temperature should be in the range of 900-950°C to prevent decarburization and provide optimum carbon activity on the steel surface [12].

As mentioned in earlier, carburizing process is made up of two major steps. The first one is *carbon embedding* into the surface in the controlled atmosphere. In addition, the second step is *quenching* which is special kind of cooling from carburizing temperature to the service temperature. Quenching is very critical process to attain required material properties since phase transformations, formation of strain and stress are

occurred during this stage. If it is wanted to optimize and control the output of the heat treatment, it should be called more attention to steel quenching.

The first thing considered in quenching process is quenching media, which is called quenchant. After the steel specimen is held enough time at carburizing temperature, it is quenched by using different quenchant, which determines the cooling rate of the steel. Depending on the cooling rate, austenite phase can transformed into final phases such as ferrite, pearlite, bainite, and martensite. In some case, it cannot transform and it remains in the microstructure as a retained austenite. Quenching medium can be selected as furnace atmosphere, which causes very sluggish cooling, air, oil or water. Water quenching provides the fastest cooling and almost entire austenite convert into martensite phase; however, it tends to unintended cracks due to impact volume change from the FCC to the BCT structure. Aqueous polymers are generally preferred as quenching media rather than the water to attain optimum cooling rates.

Phase transformation occurred during steel quenching can be appraised with the thermochemical point of view. Variation of temperature is the major driving force for the phase transformation. To evaluate the transformation kinetics of phases, the most straightforward approach is investigation of Time Temperature Transformation (TTT) or Continuous Cooling Transformation (CCT) diagrams of the steel. The one of the examples of CCT diagram is shown in Figure 2. 4, which is the representative CCT, diagram of SAE/AISI 8620 steel. Actually, CCT diagrams of the steels are varied for the same steel with respect to heat treatment histories. For each heat-treated steel, special CCT diagrams should be drawn by using different methods; dilatometer method or some advanced computer simulation programming. From the CCT diagrams, critical cooling rates for the desired phases cab be calculated.

Quenchant temperature is another important parameter to control the cooling rate since it determines the temperature gradient that is the main driving force of the phase transformation. The temperature should be selected by taking into consideration of CCT diagram of related steel. The critical point is martensite finish temperature (M_f). Some of the austenite phase could not transform and retain in the microstructure unless the temperature of quenchant is lower than the M_f temperature.

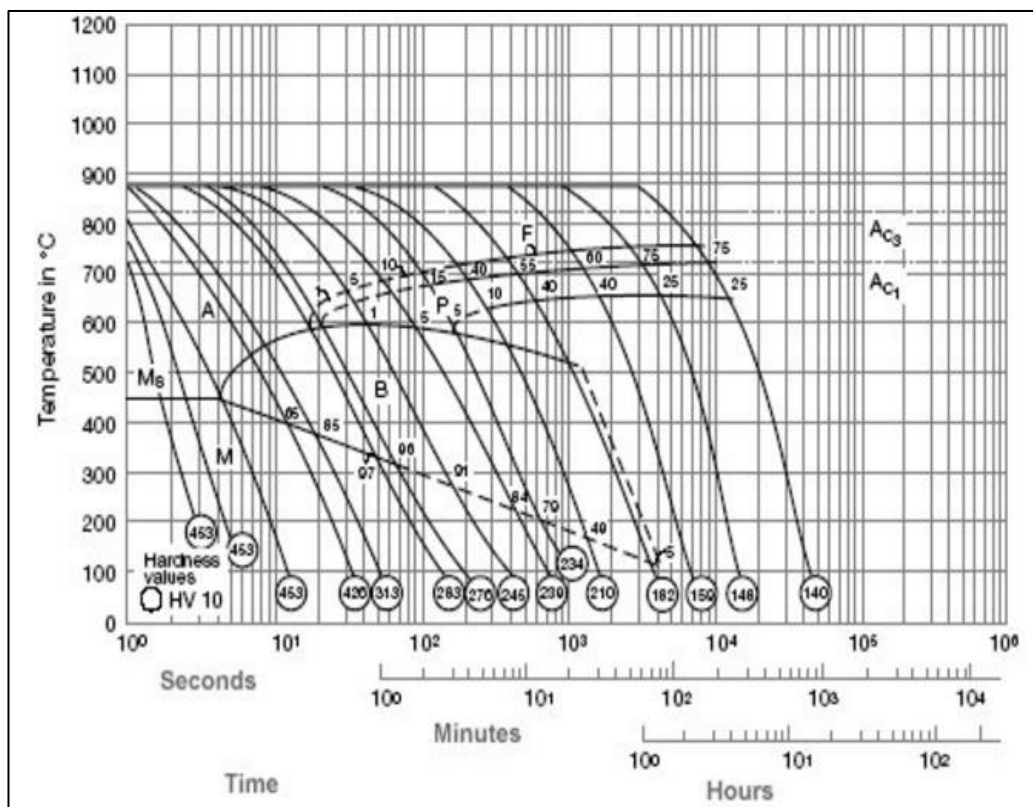


Figure 2. 4 Representative CCT diagram of AISI/SAE 8620 Steel with the average grain size ASTM 9 and austenitized at 880°C [22].

2.2. Tempering of Steels

As pointed out in the carburizing and quenching heat treatment part, martensitic microstructure is desired due to the high hardness that originated from the strong super saturation of carbon and the high density of crystal defects such as dislocations, and high- and low-angle boundaries within the lattice [23]. On the other hand, this hard phase has insufficient toughness for some engineering applications. At this time, tempering process can be the solution to provide the strength for greater ductility via reduction of the carbon super saturation and it causes the transformation of martensite into more stable structures, in other words, tempering usually results in an increase in toughness and a simultaneous reduction in hardness. During tempering, hardened steel is heated up to some critical temperature and maintained at this temperature for a sufficient time. Meanwhile, martensite is transformed into tempered martensite that consists of uniformly dispersed spheroids of cementite (carbides) in a soft matrix of ferrite. It causes to reduction in hardness and increase in toughness. Hardness reduction occurs due to the decomposition of martensite into cementite and softer ferrite phase. The degree of the tempering effect depends on the temperature and time of the process [24, 25]. The tempering temperature may be selected up to the lower critical temperature (A_{c1}). During reheating of steel up to elevated temperature level, several reactions such as carbon segregation, carbides precipitation, retained austenite decomposition and recrystallization of martensite can occur. For a better understanding of the mechanism of tempering, four main stages of tempering should be examined with respect to rising temperature.

First stage of tempering occurs in the temperature range 25-200°C. In this temperature range, formation of transition carbides such as ϵ -carbides (Fe_2C_4) begins due to the precipitation of excess carbon by the short-range diffusion of carbon to the dislocations and martensite plate boundaries. Further increase in temperature range 200-300°C causes that if retained austenite exists, it decomposes into the cementite and ferrite. In

some special cases, retained austenite might be transformed into lower bainite on the condition that the thermodynamic and kinetic conditions are provided [26, 27].

At higher temperature up to 400°C, third stage of tempering occurs. In this stage, nucleated and transformed cementite particles begin to grow and lead to tempered martensite embrittlement phenomena occurred in the temperature range 240-400°C due to the segregation of impurities at grain boundaries. This phenomenon is called as tempered martensite embrittlement. Because of this situation, toughness could not be increased as expected whereas hardness of tempered martensite might be higher than that of the as-quenched form. Upon further increase in tempering temperature or tempering time, stage four could be defined as carbide coalescence stage. At the 600°C, tempering leads to become sphere like-martensite and carbides. In some alloy steel, secondary embrittlement occurs due to impurity segregation at the grain boundaries and decohesion of the grain boundaries. It tends to intergranular fracture that corresponds the loss of toughness [23].

2.3. Residual Stresses

2.3.1. Definition of Residual Stress

The failure of an engineering structure or component occurs not only due to external loads; residual stress state should also be taken into account. Any manufacturing process introduces a state of residual stress that may result in either positive or negative effect. For instance, compressive residual stress at the surface improves fatigue performance while in a corrosive environment tensile residual stress at the surface increases the tendency for stress corrosion cracking.

Residual stresses are defined that the stresses exist without any external load on the part and they are formed by the consequence of interactions among time, temperature, deformation, and microstructure (Figure 2. 5). In some sources, these stresses are classified as self-equilibrating stress due to the compensation of local tensile and compressive stresses with respect to force and moment within the bulk material or structure. It is the result of the metallurgical and mechanical history of each point in the part.

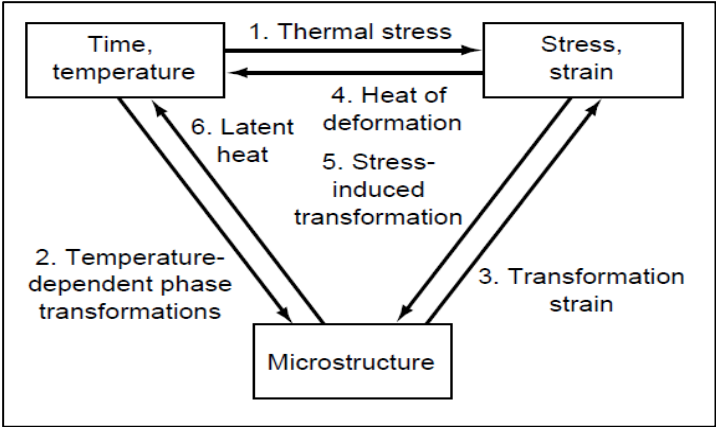


Figure 2. 5 Relationships between residual stress and several factors [28].

Residual stresses can be classified in three groups, macroscopic residual stresses, when the enlargement of the volume is large compared to the grain size (Type I), microscopic residual stresses, which occurs in the size of the grains (Type II) and submicroscopic residual stresses that the enlargement of the volume is smaller than the grain size (Type III) [28].

Almost all manufacturing processes cause the residual stresses. In some cases, they are intended within the material whereas they are sometimes created inevitably. There are

several reasons for the formation of residual stresses. They are mainly differential plastic deformation, inhomogeneous thermal gradient and phase transformations.

2.3.2. Formation of Residual Stresses during Carburizing

Control of heat treatment process is one of the most common concern for the metal processing industry. Carburizing process is commonly used technique for the hardening of the surface of the steel specimen by creating hard martensitic layer on the surface. However, especially martensitic transformation can cause to the evolution of large residual stresses. When the mechanism of residual stress formation after carburizing is examined, the first thing that must be understood is thermal and microstructural variations and gradients in the each step of carburizing process.

The main step, which causes residual stress, is quenching. Due to the high cooling rate at the beginning of the quenching part, high thermal gradients are implemented between case and core region without any phase transformation. This situation causes the thermal shrinkage between case and core region. Moreover, carbon content of surface and core region is invariant through the depth. CCT diagrams are varied by changing carbon content and alloying elements. In carburized conditions, surface and core region have actually different cooling curve diagrams. Especially the martensite transformation temperatures and pearlite start cooling curve significantly change with varying carbon content. Martensite start and finish temperatures reduce with increasing carbon content which tends to retard the phase transformation stage during quenching. Although the temperature gradient of surface is higher than that of the core, transformation could be started later than the core phase transformation and the inhomogeneous carbon distribution within a distinct depth is responsible for the final residual stress state. Hence, knowledge of corresponding continuous-cooling-transformation (CCT) diagrams plays a significant role in the formation of final residual stress state.

To understand the formation and evolution of residual stress between core and case region, three possible cases can be deduced. The first theoretical case can be that the surface region transforms earlier than the core, which is shown in Figure 2. 6 as case I. The other possibility is that the transformation of the core region occurs firstly and then the transformation of surface region precedes, seen in the same figure as case II. The last situation could be that there is no priority concerning the sequence of the transformation between the case and core.

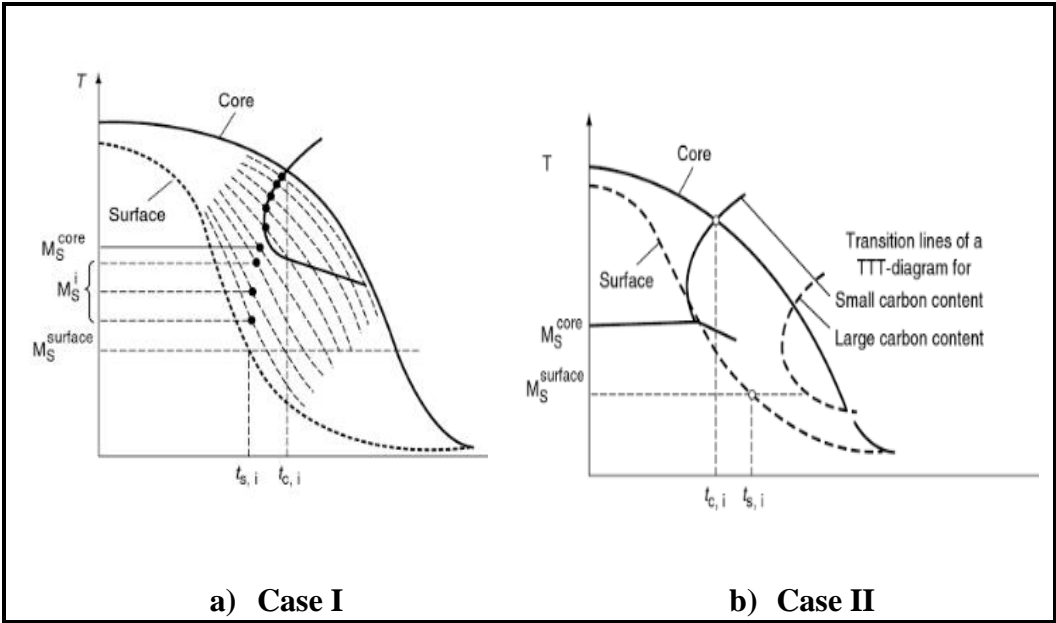


Figure 2. 6 Demonstration of two possible cooling case during quenching of carburized specimens [29].

When the case I is considered in detailed manner, the surface of the samples cools down faster than the core region, which tends to thermal shrinkage. Because of this, tensile type stresses are created on the steel surface and compressive stresses in the core region arise. Figure 2. 7 demonstrates the residual stress evolution gradually for the special cooling condition in which cooling rate of the surface is enough to occur martensitic transformation whereas core region of the specimen does not show this

type of displacive transformation. As seen in this figure, tensile stresses increase on the surface and compressive stresses arise in the core until starting of the phase transformations. In addition, the other metallurgical reason of the evolution of residual stress is phase transformation during cooling, which can be reconstructive or displacive. According to the transformation mechanism, certain lattice distortions and dislocations induced by plastic deformation during transformation determine the type of created residual stresses. Therefore, the second stage of quenching can be investigated with respect to metallurgical phase transformation. In case I, second stage of quenching commences as soon as the martensitic transformation starts on the surface. When the surface temperature cools down to the M_s temperature, the surface region starts to transform. Due to volume differences between austenite and martensite phases, surface of the steel shows the tendency to expand due to the increase in volume after martensitic transformation. Then, thermal tensile stresses are counteracted. A large amount of the compressive stresses is created on the surface. The next stage in the quenching starts once the phase transformations start in the inner region, which is core region. In this stage, the material at the surface is transformed into martensite completely and it cools down. However, at that time, expansions caused by martensitic transformations are restricted due to the surface and near-surface regions that are relatively cool and rigid. As a result, compressive residual stresses are formed on the outer region whereas tensile residual stresses are created in the inner region. At the end of the carburizing and quenching processes, the surface region of the specimen has tensile residual stresses similar to the through hardening process. The situation can be occurred when the difference of carbon content between the core and the surface is relatively lower than that of the case II. Carburizing process of medium carbon steel can show this type of residual stress formation sequence.

The case II is observed especially in case hardening of the low carbon steel. Firstly, the core region transformation occurs and then the surface transformation precedes.

The sequence of residual stress formation is demonstrated in Figure 2. 8. At the beginning of the quenching, the surface of the component cools down and hence shrinks faster than the core of the component, similar to the case I. An Eigen stress field is formed within the component. Tension on the surface in axial and tangential direction occurs with the opposite direction of the shrinkage tendency of the surface, whereas the core is loaded on compression in order to balance. Then, the thermal gradients reduces on the surface and the temperature difference between the surface and core starts to vanish. It causes the decrease in the strength of the tensile stress field on the surface. Meanwhile, the magnitude of the compressive stresses also starts to decrease at the core region in order to equilibrate stresses at the surface. The stress variation is related to only thermal contradictions. However, at the same time, phase transformations of the core and the case region are happened. They cause the final distribution of the stress state. At the time $t_{c,i}$ shown in Figure 2. 8, austenite phase begins to transform into pearlite phase in the core region. It causes the compressive stress formed by the contraction of the part in the core. It is balanced by corresponding tensile surface residual stresses. And near-surface of the specimen that has a lower carbon content than that of the surface the specimen transforms from austenite to martensite between the time $t_{c,i}$ and $t_{s,i}$. When the time $t_{s,i}$ is reached, the surface of the component transform into the martensite phase. However, at that time, the expansion caused by martensitic transformation is restricted due to the surface and the near-surface region that are relatively cooler and more rigid. The thermal equilibrium is almost reached at the end of quenching. All phase transformations complete and compressive residual stresses are created on the surface region of specimens. On the other hand, tensile residual stresses are created in the core region.

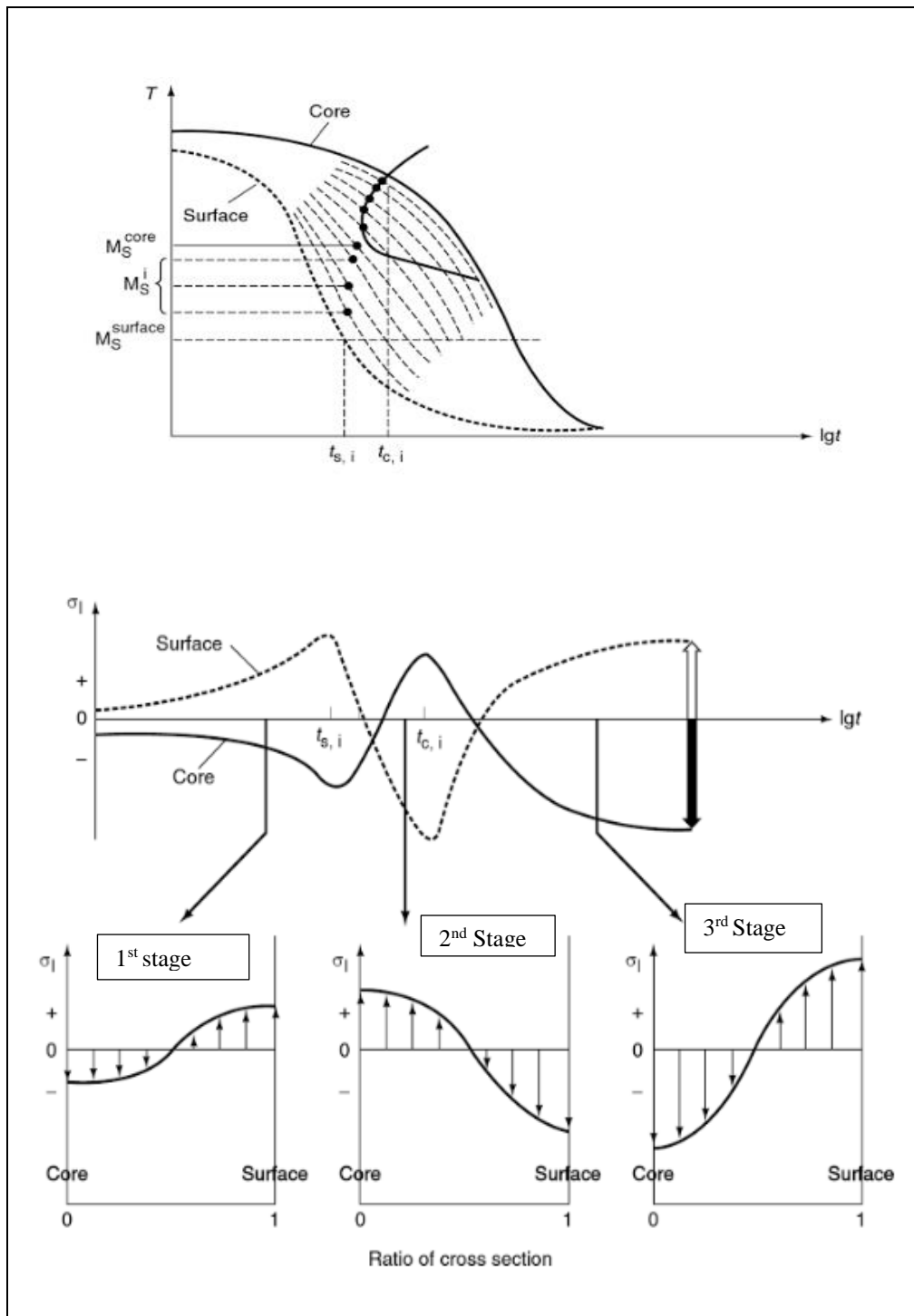


Figure 2. 7 Demonstration of the residual stress evolution gradually for the Case I ; cooling rate of the surface is enough to obtain martensitic transformation, but core of the specimen does not show [29]

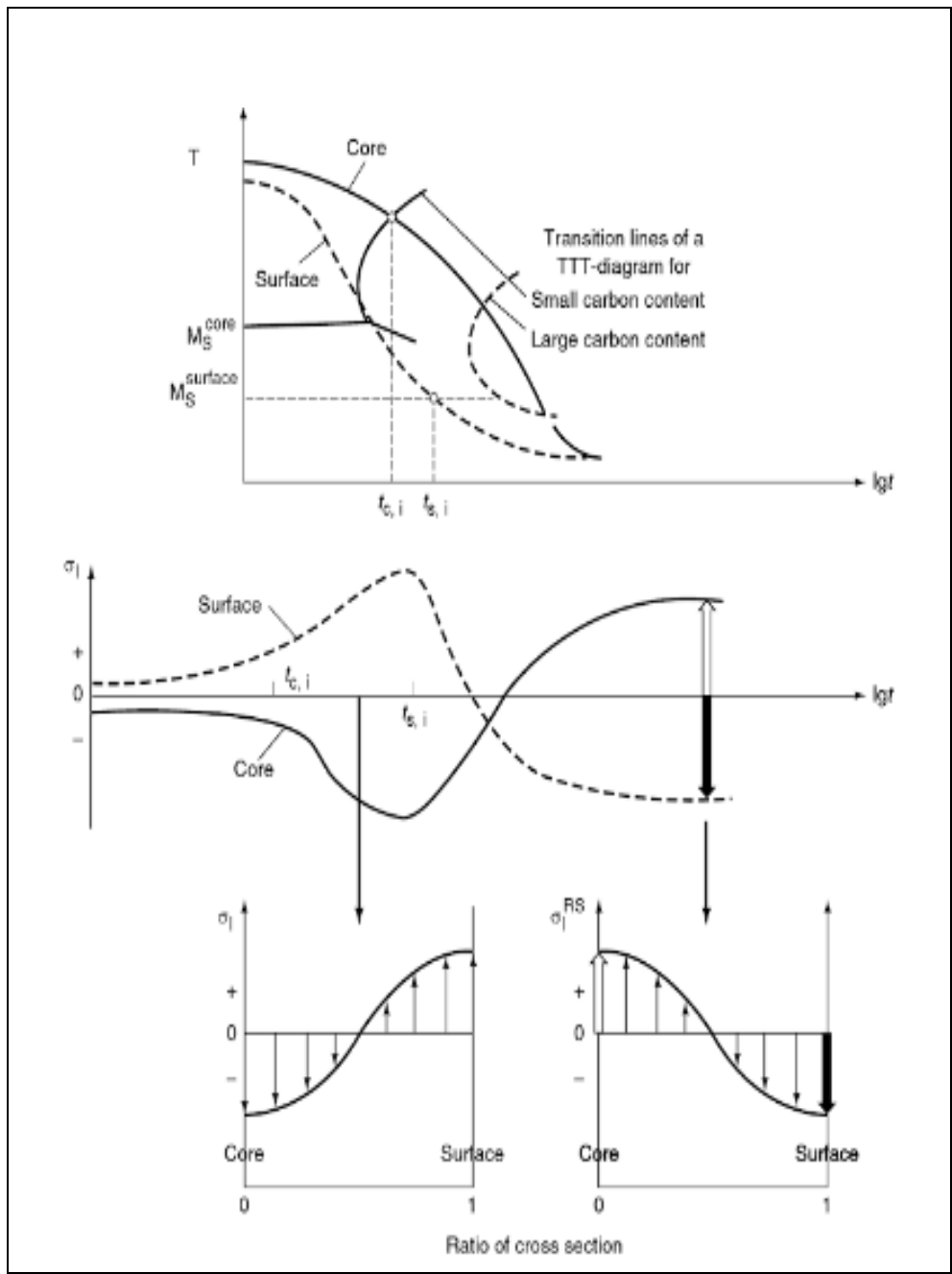


Figure 2. 8 Demonstration of the residual stress evolution gradually for the Case II; the differences in cooling rate of the surface and core is not high [29].

2.4. Measurement Techniques of Residual Stresses

The field of stress analysis has gained an importance from widespread applications in industry. An increasing interest in how the state of residual stress changes the mechanical properties of a material and its structure has been attracted. All engineering components and structures must be designed and produced with sufficient reliability. Hence, the relation between local stresses and strength should be considered. Therefore, the residual stress has to be taken into account in the design to make the component safer and more reliable. In real life, the residual stress cannot be measured directly. They can be defined as locked-in stresses and the evaluation of them becomes very challenging issue because of the locked-in characteristic. Similar to the measurement of the external stress, residual stresses can be measured indirectly by measuring strain or displacement.

In the earlier stages, the residual stress was identified by observing the dimensional change that was occurred after cutting of the material. However, the material could not be used hereafter since the cutting process has destruct the material. Hence, destructive methods caused the very high volume of material scrap. With the passage of time, residual stresses have become more sophisticated and quantitative. Then, non-destructive methods were simultaneously invented by using different physical and metallurgical background such as X-ray diffraction phenomena, ultrasonic and magnetic wave characteristics. They are largely based on the early historical roots; however, they require great conceptual knowledge of the measurement and computational capabilities in order to understand them. When they are classified in respect to degree of harmfulness, they are called as destructive, non-destructive or semi-destructive measurement methods. These techniques are shown in Figure 2. 9.

The most commonly used destructive techniques in industry are the ring core technique, the bending deflection method, the sectioning method and the hole-drilling method. They are based on the measurement of the macroscopic residual stress [30]. On the other hand, non-destructive techniques are improved with the development of the metallurgical science and technology. Especially, diffraction techniques have made great strides in this field. Among various methods, which are available to measure residual stress, the X-Ray Diffraction (XRD) method gives a knowledge that is more accurate about residual stress state with the appropriate spatial and volumetric resolution. It adequately characterizes the residual stress distributions. However, it is relatively expensive and it requires long measurement periods [31].

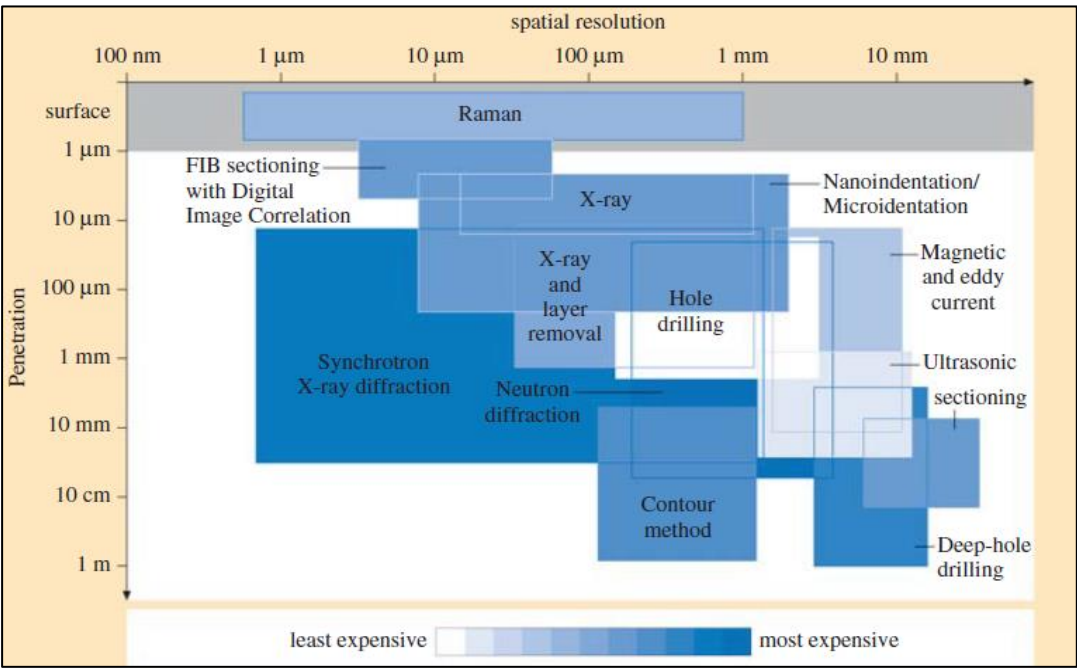


Figure 2. 9 Demonstration of residual stress measurement method with respect to penetration depth, spatial resolution [32].

Industry has been requesting alternative ways to measure the residual stress with high accuracy, quickly and easily without damaging the material being tested. For this

purpose, a less traditional approach, which is the magnetic Barkhausen noise (MBN) technique, is of particular interest since it has several advantages over other techniques. It is the non-destructive industrial tool to monitor and measure residual stress and the other microstructural features of material quickly. This technique comprises the main aim of the study and theory of the technique will be discussed upcoming theory parts in detailed manner.

2.4.1. Theory of X-ray Diffraction Method

X-ray Diffraction (XRD) method is leading technique to evaluate residual stress state non-destructively. The XRD method has the appropriate spatial and volumetric resolution that adequately characterizes the residual stress distributions. However, critical assumptions should be made to calculate the residual stress value. In addition, with each evolutionary step of practice of this technique, these assumptions could be sometimes erroneous that reduces its reliability [33]. In this part of the study, XRD technique will be introduced in detailed with respect to physical background, advantages and limitations.

In diffraction phenomena, X-rays diffract from crystalline materials according to the Bragg's Law. Atoms within the perfect crystalline materials are arranged regularly with the periodic atomic planes that are separated each other with the certain lattice distance [34]. This distance is called interplanar atomic spacing. X-Ray diffractions occur when the radiation interacts with atoms or crystallites arranged in a regular array with the certain diffraction angle (2θ). Interplanar atomic spacing of diffracted planes are directly related to the diffraction angle for certain wavelength and could be calculated by using Bragg's Law;

$$n\lambda = 2d_{hkl} \sin \theta \quad \text{Eq. 4}$$

therein d_{hkl} is the interplanar spacing of the plane with the Miller's indices $\{hkl\}$, θ is the Bragg's angle, and n the order of the interference, which is usually combined with the Miller's indices [35].

XRD method is based on the change in the interplanar atomic spacing of the material under some external or internal stress field. The elastic strain is created within the material under these stress fields. This tends to distortion in crystal structure and atoms move to new equilibrium positions. Because of the movement of atoms, characteristic diffraction peaks of related crystal shift. By considering the amount of shifting, change in the interplanar atomic spacing of crystal (d) can be directly measured by XRD method, demonstrated in Figure 2. 10. By using the value of the change, the total stress tensor within the surface of material can be calculated [36,37].

There are several stress calculation approaches in the literature, which differ from each other in respect to assumptions taken during the conversion of strain into the stress tensor. To establish mathematical relationship between strain and stress tensor by using interplanar atomic spacing, special coordinate systems should be defined; sample (S_i) and laboratory coordinate systems (L_i), seen in Figure 2. 11. In this figure, Φ and Ψ angles are also showed. The axes \vec{S} define the surface of the specimen. The laboratory system \vec{L} is defined such that \vec{L}_1 is in the direction of the normal to the family of planes $\{hkl\}$ whose spacing is measured by X-rays. \vec{L}_2 is defined by \vec{S}_1 and \vec{S}_2 . And it makes an angle Φ [32].

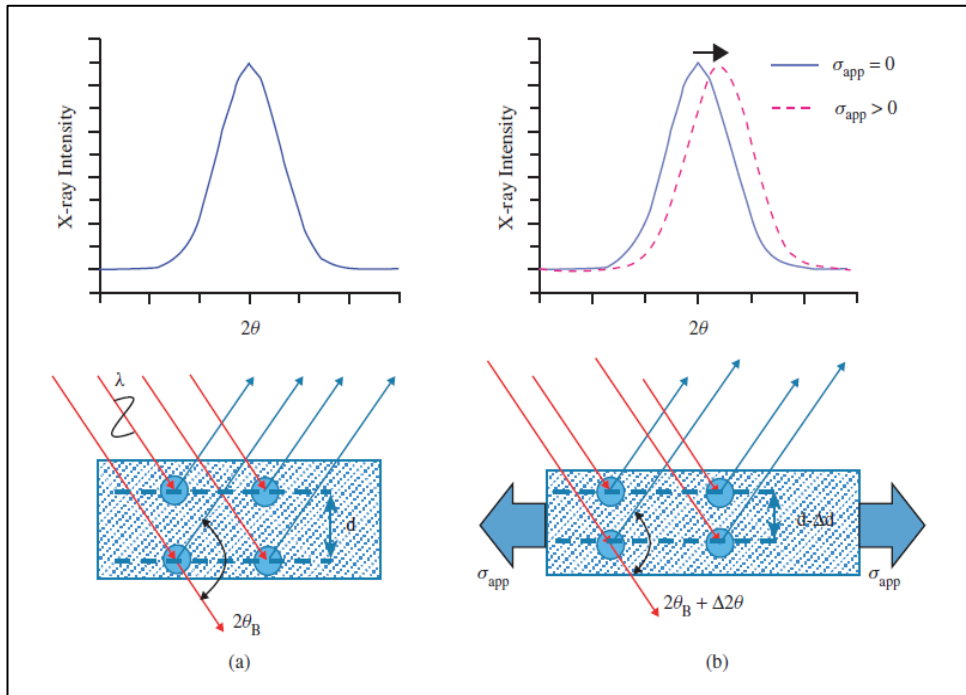


Figure 2. 10 Schematic of X-ray diffraction paths and peak position (a) unstrained state and (b) under tensile strain due to an applied load [32].

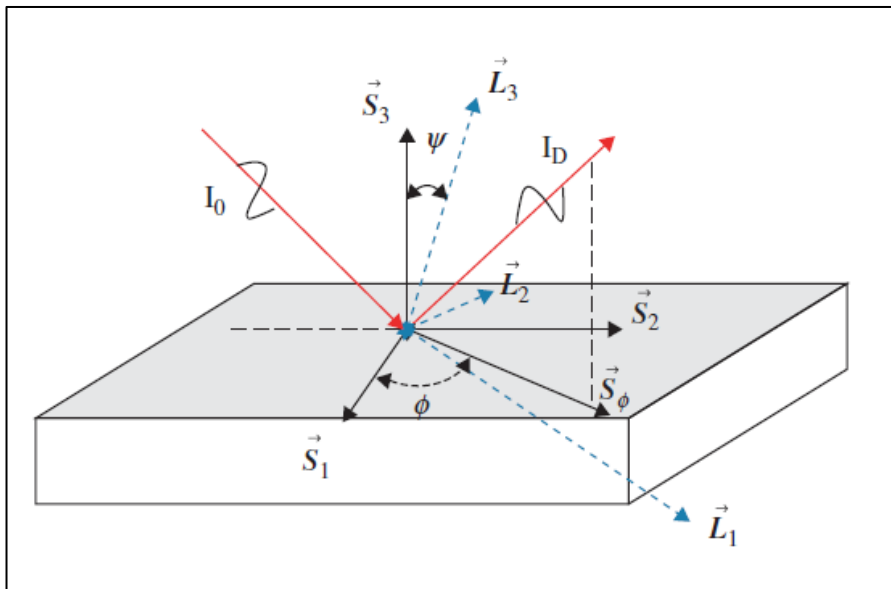


Figure 2. 11 Demonstration of S_i (sample coordinate system) and L_i (laboratory coordinate system)

After setting Φ and Ψ angles by diffractometer, diffraction peak is obtained at the position of certain Brag's angle θ_B and lattice spacing $d_{\Phi\Psi}$ is obtained from using Brag's law for the used wavelength. Once calculating the lattice spacing $d_{\Phi\Psi}$, the strain along ϵ'_{33} may be obtained from the formula;

$$(\epsilon'_{33})_{\Phi\Psi} = \frac{(d_{hkl})_{\Phi\Psi} - d_0}{d_0} \quad \text{Eq. 5}$$

From integrating stress tensor knowledge of direction cosines a_{3k} and a_{3l} described and derived in ASTM E2860 standard [33], the fundamental equation of strain could also be expressed

$$(\epsilon'_{33})_{\Phi\Psi} = \frac{(d_{hkl})_{\Phi\Psi} - d_0}{d_0} = \epsilon_{11} \cos^2 \Phi \sin^2 \Psi + \epsilon_{12} \sin 2\Phi \cos^2 \Psi + \epsilon_{22} \sin^2 \Phi \sin^2 \Psi + \epsilon_{33} \cos^2 \Psi + \epsilon_{13} \cos \Phi \sin 2\Psi + \epsilon_{23} \sin \Phi \sin 2\Psi \quad \text{Eq. 6}$$

This equation takes into consideration that all stress and shear components with whole dimensions are present and hence there are many unknown stress tensor terms. To overcome such difficulties, some assumptions could be made such that the principal stress which is normal to the specimen surface can accepted zero; that is $\sigma_3 = 0$. However, strain ϵ_z will not be equal to zero. If the material under investigation is isotropic and well-known Hooke's Law ($\sigma = E \cdot \epsilon$) is integrated above equation, it becomes;

$$\frac{(d_{hkl})_{\Phi\Psi} - d_0}{d_0} = \frac{1+\nu}{E} \{ \sigma_{11} \cos^2 \Phi + \sigma_{12} \sin 2\Phi + \sigma_{22} \sin^2 \Phi - \sigma_{33} \} \sin^2 \Psi - \frac{\nu}{E} (\sigma_{11} + \sigma_{22} + \sigma_{33}) + \frac{1+\nu}{E} \{ \epsilon_{13} \cos \Phi + \epsilon_{23} \sin \Phi \} \sin 2\Psi \quad \text{Eq. 7}$$

where ν is the Poisson's ratio and E is the Young Modulus of used material. To calculate strain values, two techniques are commonly used; $\sin^2 \Psi$ technique which is based on the shearless biaxial stress state and Dölle-Hauk Method [38, 39]. In the shearless biaxial stress state, stress tensor is considered as,

$$\begin{bmatrix} \sigma_{11} & 0 & 0 \\ 0 & \sigma_{22} & 0 \\ 0 & 0 & 0 \end{bmatrix}$$

Moreover, Eq. 7 can be written by considering the matrix form to facilitate a least-squares analysis as;

$$\frac{(d_{hkl})_{\phi\Psi} - d_0}{d_0} = \frac{1+\nu}{E} \{ \sigma_{11} \cos^2 \phi + \sigma_{22} \sin^2 \phi \} \sin^2 \Psi - \frac{\nu}{E} (\sigma_{11} - \sigma_{22}) \quad \text{Eq. 8}$$

Eq. 8 predicts a linear variation of \mathbf{d} vs $\sin^2 \Psi$. The stress in the S_ϕ direction could be get directly from the slope of a least-squares fitted line to experimental data, collected at different Ψ in the case of that the elastic constants E , ν and the unstressed plane spacing, d_0 , are known. This calculation method is called as the $\sin^2 \Psi$ technique. In this procedure, if the maximum elastic strain is less than 2%, the value of d_0 may be taken as the plane spacing at zero tilt, $d_{\psi=0}$ [32].

The other most frequently used technique is Dölle-Hauk technique, which considers the triaxle loading/stress tensor conditions; i.e.; σ_3 is not zero. By applying this technique, ϵ_{33} could be calculated by using below equation;

$$\epsilon'_{33} = \frac{(d_{hkl})_{\phi\Psi} - d_0}{d_0} = \frac{1+\nu}{E} \{ \sigma_{11} \cos^2 \phi + \sigma_{12} \sin^2 \phi + \sigma_{22} \sin^2 \phi \} \sin^2 \Psi + \sigma_{33} \cos^2 \Psi - \frac{\nu}{E} \{ \epsilon_{23} \sin \phi \} \sin 2\Psi \quad \text{Eq. 9}$$

In this approach two terms, which are based on above equation, should be defined as;

$$a_1 = \frac{1+\nu}{E} \{ \sigma_{11} \cos^2 \phi + \sigma_{12} \sin 2\phi + \sigma_{22} \sin^2 \phi \} \sin^2 \Psi + \epsilon_{33} \quad \text{Eq. 10}$$

$$a_2 = \{ \epsilon_{13} \cos \phi + \epsilon_{23} \sin \phi \} \sin 2\Psi \quad \text{Eq. 11}$$

If $\epsilon_{\phi\Psi}$ data are obtained over a range of positive and negative Ψ tilts at (least) three ϕ independent measurement directions (i.e. 0° , 45° , 90°), the unknown in-plane strains (ϵ_{11} , ϵ_{12} , ϵ_{22}) can be obtained from the slopes of a_1 vs $\sin^2\Psi$ plots; while ϵ_{33} can be obtained from their intercepts. Out-of-plane shear strain terms (ϵ_{13} , ϵ_{23}) can be obtained from the slopes of a_2 vs $\sin^2\Psi$ plots. Desired stress tensor could be obtained by multiplying the strain vector with the Young modulus matrix or stiffness matrix for isotropic linear elasticity for plane-stress condition [32].

Up to here, stress state is idealized by making some certain assumptions with respect to stress/strain condition and material type of the specimen. When the idealized system is changed, several approaches should be tried by considering the main relationship between strain and interplanar atomic spacing of specimen. Despite making some assumptions, XRD technique has been commonly used for over years since its reliability has been proved and reported by many scientists. Even so, XRD technique has some disadvantageous such that it is restricted for the field measurement. The need

for surface preparation also restricts the scope of its application. Moreover, its time-consuming feature and high cost do not correspond industrial demands.

2.4.2. Theory of Magnetic Barkhausen Noise Method

The new mainstream of industry is to find alternative ways to measure residual stresses accurately, quickly and easily without damaging the material. Nowadays, magnetic methods have been gain importance for ferromagnetic material evaluation due to its speed. Magnetic Barkhausen Noise (MBN) method is the quite compelling issue for industry and scientists. Although the measurement speed is high, this method has also some contradictions since it is strongly influenced by several factors. The MBN results generally correspond to the combined effects of stress state and the other factors such as phase composition, grain size, strain hardening, crystallographic texture, grain shape, grain orientation, carbide size and distribution, and other microstructural characteristics. Hence, the interpreting of the results is more difficult than the other techniques. To vanish this, theoretical background of magnetic materials, MBN measurement method and the influencing factors must be well comprehended.

In this study, the main aim is the monitoring of residual stress state by using MBN technique. In the next part of the thesis, the physical background of MBN technique which includes the magnetic properties of steel, domain movement mechanism, software types, MBN devices and measurement requirements will be explained and then the effects of three main factors will be discussed; microstructure, hardness and stress state.

2.5. Magnetic Barkhausen Noise Method

2.5.1. Introduction to Magnetic Materials

Magnetic Barkhausen Noise was discovered by Prof. Barkhausen in 1919 [40]. He ascertains the secret behind the discontinuous character of the motion of the magnetic domain walls of ferromagnetic materials. Before the formation mechanism of Barkhausen Noise Signals is explained, magnetic properties of the materials and domain theory should be stated for a better understanding. The magnetic properties of materials are originated from the orbital and spin movement of the electrons [41]. The movement of an electron around the nucleus may be considered like a current in a loop of wire, which has no resistance whereas spin movement of electron in the orbital is a universal property. It is associated with directly the magnetic moments and angular momentum. The atom contains many electrons and each of them spins at its own axis and moves in its own orbit. The created magnetic moment vector is parallel to the axis of spin and normal to the plane of the orbit, respectively [41]. The sum of these two magnetic moment vectors can cause two possible situations. The first one is that the magnetic moments of all electrons are well oriented. This means that they cancel each other. It tends to exist no net magnetic moment. This behavior is called diamagnetism. The other scenario is that the partial cancellation of the magnetic moments is occurred. Materials possessed such kind of magnetic moment can be called paramagnetic, antiferromagnetic, ferrimagnetic or ferromagnetic. Ferromagnetism plays an important role for the generation of Magnetic Barkhausen Noise. In ferromagnetic materials like iron, cobalt and nickel, one of the electrons has occupied at the 4s energy level before the filling of the 3d shell. It causes the spontaneous domain magnetization generated by the unpaired electron spins from partially filled shells.

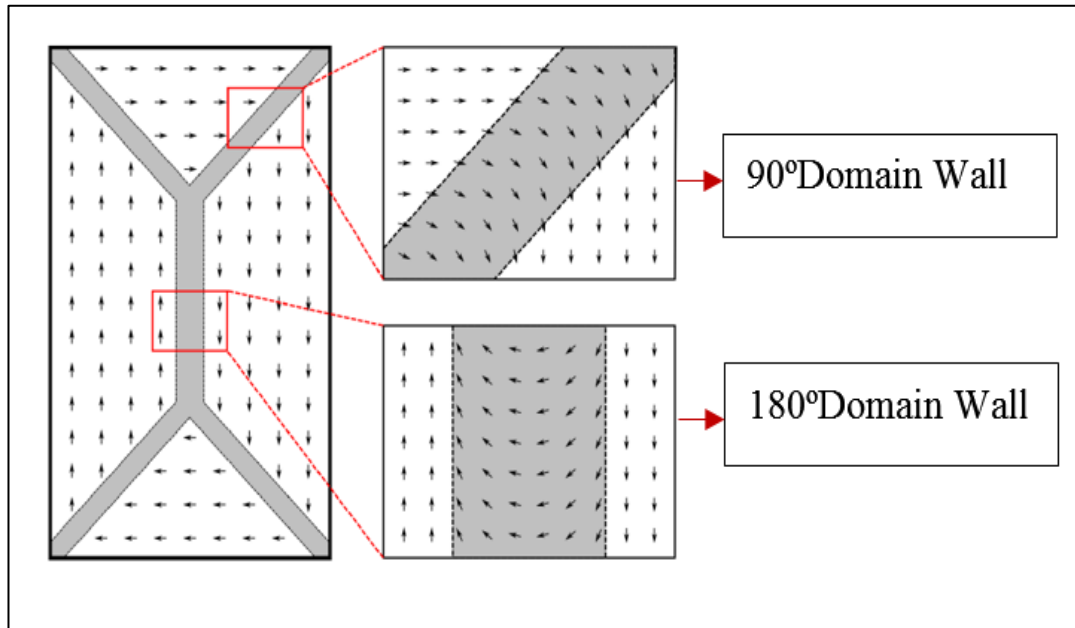


Figure 2. 12 Schematic demonstration of domains in the ferromagnetic materials and the domain wall alignments [41].

According to the theory of magnetism [42], ferromagnetic materials are consisted of the magnetically ordered small regions that are called domains. The orientation direction of domains generally follows one of the crystallographic axes that are preferred rather than the others. These preferred axes are called the "*easy axes*". The magnetocrystalline anisotropy depends on the internal energy of domains on the direction of inner magnetization, which is the minimum for domains located parallel to easy directions of magnetization [43, 44]. The boundaries between domains are known as domain walls. The magnetic dipoles change their alignment when they across them [42]. Figure 2. 12 shows the ferromagnetic domains and domain walls that are 90° and 180° domains walls. The 180° domain walls occur in all materials. They are not affected by stress whereas the other non-180° domain walls are influenced due to the anisotropy. Hence, MBN activity is dominated by the motion of 180° walls.

Moreover, when the ferromagnetic material is magnetized, it can respond by changing its dimensions. The resulting change in direction tends to strain that is called the magnetostriction. It occurs due to the spin-orbit coupling of valence electrons in ferromagnets. From a phenomenological point of view, two main types of magnetostriction exist: spontaneous magnetostriction arising from the orientation of the magnetic moments within the domains at the Curie temperature; and the field induced magnetostriction. In the case of magnetostriction, the volume of the ferromagnetic material remains constant despite its dimensions change upon the application of magnetic field.

To generate Barkhausen noise, the ordered domains in ferromagnetic materials must be oriented by the external magnetization. When magnetostrictive materials are exposed to external magnetic field (H), the preferred magnetic domain orientations are altered. When the magnetic field (H) has been generated in the ferromagnetic material by a current, in accordance with the Ampere's law, the magnetic flux (B) is induced in the related material as the response of the medium. This is also called magnetic induction. The relationship of these two term B and H gives magnetic permeability of material (μ);

$$\mathbf{B} = \mu\mathbf{H} \qquad \text{Eq. 12}$$

2.5.2. Hysteresis Curves

When material is magnetized, magnetic field strength can be applied positively and negatively. Moreover, the change in the magnetization may be in either reversible or irreversible direction. A reversible change in magnetization is defined that

magnetization returns to its initial value after removing of magnetic field. Generally, both reversible and irreversible changes occur together, so the magnetization does not return to its initial value. Because of this type of magnetizing loop, hysteresis curve is obtained, shown in Figure 2. 13. At the beginning of the applying magnetic field, the domain walls relax. When the applied field is removed, they start to orient themselves into the non-magnetized state. Until that point, the process is reversible. Further increase in the applied magnetic field, the wall motion shows the irreversible behavior. This means that the growth of domains arises until the single domain is obtained in the easy axes direction. It is aligned parallel to applied field. At that point, the ferromagnetic material reaches the magnetic saturation [41, 45, 46]. Figure 2. 13 shows the steps of the magnetization.

Each ferromagnetic material has special hysteresis behavior in respect to its magnetic permeability, microstructural features, stress state within the material etc. Moreover, the characteristic curves provide information about some magnetic parameters of materials; coercivity (H_c), remanence (B_r), permeability (μ_r), hysteresis loss (WH), magnetic saturation (M_s).

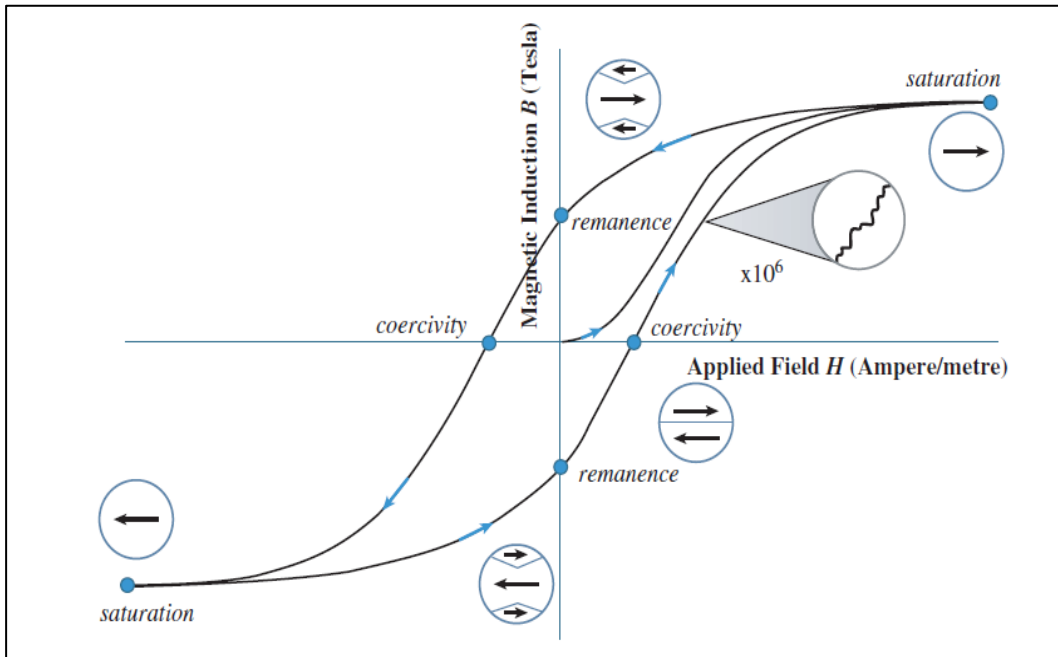


Figure 2. 13 Representative hysteresis curve of magnetized samples that shows the both reversible and irreversible magnetization behavior together [41].

The *coercivity* is defined as the reverse magnetic field at which the magnetic induction comes down from saturation (B_s) to zero [41]. The coercivity value of ferromagnetic materials provides the rough attribution of magnetic softness. If the coercivity value is lower than that of the Earth's, the material is called magnetically soft material. It is also called as mechanically soft material. It means that mechanically hard material has high coercivity. One of the examples of the situation is shown in Figure 2. 14. Hence, the terms 'hard' and 'soft' are used to distinguish ferromagnets based on their coercivity. Generally, 'hard' magnetic materials are those with coercivities above 10 kA/m(125 Oe) while 'soft' magnetic materials are those with coercivities of below 1 kA/m(12.5 Oe) [42,48]. The *remanence* is defined as the retained magnetic induction when the magnetic field is reduced from saturation (H_s) value to zero.

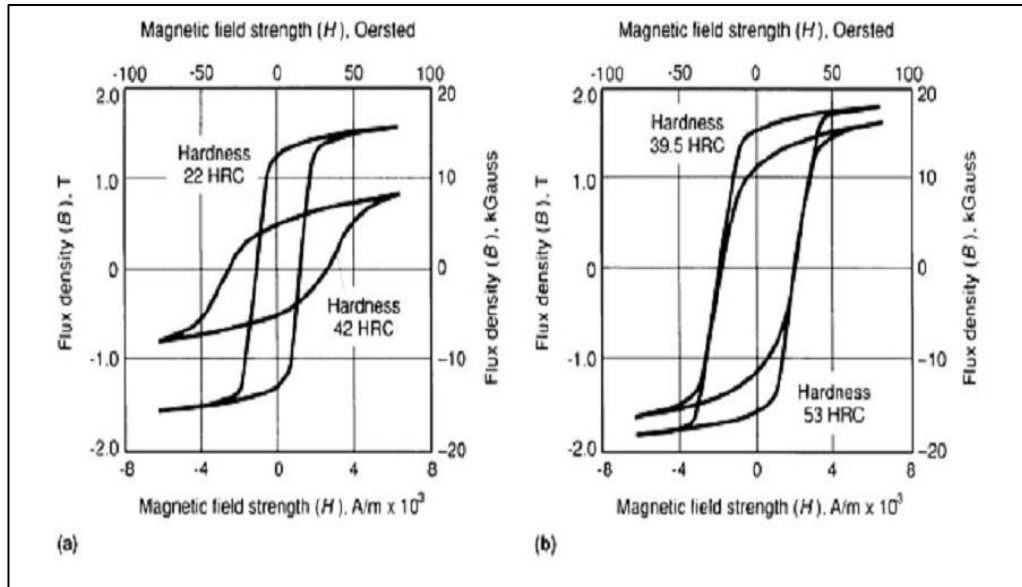


Figure 2. 14 Examples of comparison between hysteresis curves of soft and hard magnetic materials a)ASTM 410 Stainless Steel b)ASTM 4340 [49].

The other important parameter of ferromagnetic materials is *permeability* that is also related to the relationship between B and H. Permeability is defined as the degree of the magnetization of the material. Various types of permeability can be given in the literature; the initial permeability (μ_0), the maximum permeability μ_{\max} and differential/relative permeability (μ_r). The relative permeability of the material indicates how it varies magnetic induction relative to the induction that exist in the free space. The local slope of the B, H curve gives the relative permeability value. Permeability could be used for the comparison and characterization of materials since it is strongly structure-sensitive. It also depends on purity, heat treatment, deformation, etc. In the explanation of the hysteresis curves, *magnetic saturation* represents a condition where all the magnetic moment vectors within the material are aligned in the direction of the applied magnetic field. *Hysteresis loss* is related to the reducing energy of the loop area that also represents the magnetic energy. It is dissipated if the material is to be completely cycled around the loop. The energy loss is related to the irreversible

motion of magnetic domain walls within the material. It exists in the material as heat. When the loop area is high, the magnetized material is magnetically and mechanically hard. On the other hand, when the small amount of pinning sites which obstruct the movement of domain walls exist, the loop area is narrow [34, 49].

2.5.3. Barkhausen Effect

There are two types of domain movement; domain wall bowing and domain wall translation [42]. The former is reversible process. It occurs up to the certain degree of the domain wall deformation when the domain wall has low surface energy. On the other hand, the domain wall translation is irreversible process when the material is not pure. Hysteresis curves look like very smooth loops. It means that variation of magnetic flux with the applied magnetic field shows smooth and continuous behavior. However, high-resolution examination of the hysteresis curve shows that discontinuous change in the magnetic flux with the applied magnetic field is observed. The discontinuities can be explained by the existence of some microstructural defects and imperfections. When the domain wall is encountered with the imperfections during bowing or translation movement, the motion stops suddenly. If the threshold magnetic field value is reached, the domain wall is freed and it continues to the movement. The energy resulted from the interactions among the defects and the domain wall states the blocking capacity of the crystalline defect. It causes the abrupt domain movement. The discontinuous increments are called Barkhausen jumps, seen in Figure 2. 15. They are also defined as the voltage spikes. This effect is discovered by Prof. Barkhausen in 1919 and named as Barkhausen effect [41]. A secondary coil was wound on a piece of iron and connected to an amplifier and loudspeaker. Then, the ferromagnetic material that were exposed to the external magnetic field was placed near the coil. He observed that as the magnetic field strength (H) was increased smoothly, a series of clicks were heard over the loudspeaker. These clicks were generated thanks to the small voltage pulses induced in the secondary coil. The voltage spikes were caused by small changes

in flux density through the coil arising from voltage sweeps caused by the Barkhausen jumps [42]. After these observations, he concluded that the total domain wall movements created noise like signals; the Magnetic Barkhausen Noise (MBN) signals.

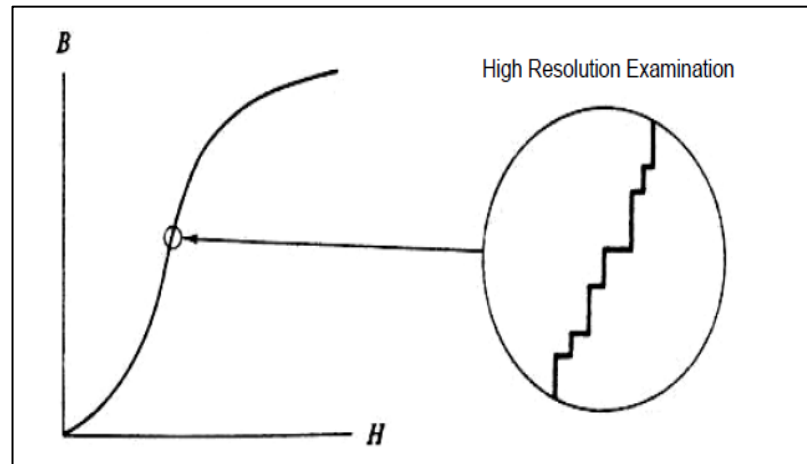


Figure 2. 15 Schematic demonstration of Barkhausen jumps with high-resolution examination [42].

2.5.4. Magnetic Barkhausen Noise (MBN) Measurement Techniques

The Magnetic Barkhausen Noise (MBN) technique is concerned with the measurement of the abrupt magnetic reorientations of domains in terms of the number and magnitude. The reorientations occur by applying the magnetic field alternatively. As indicated in previous part, the conductive secondary coil is used to gather the noise like signals created during the movements of the domain walls when they encounter some imperfections.

As demonstrated in Figure 2. 16, measurement set-up of MBN technique is made up of the signal generator with power amplifier, biasing magnet with an inductive search coil in it and a display record device for the data storage. Special C-shaped electromagnet, which is called sensor or probe, is also used to generate the time-varying magnetic field. The pick-up coil sitting on the specimen surface provides the

local magnetic field changes due to the abrupt movements of the magnetic domains. The obtained signals are in the form of burst of noise like pulses.

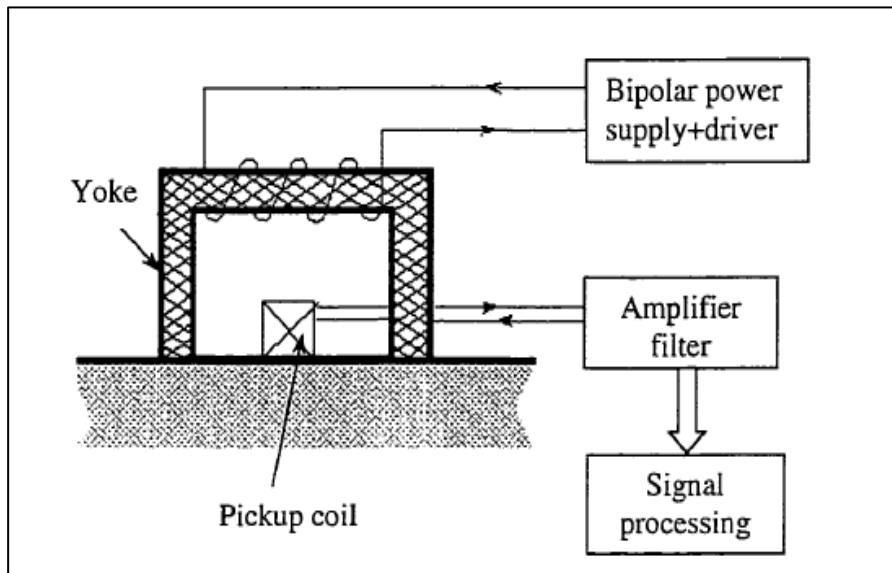


Figure 2. 16 Schematic demonstration of Barkhausen sensor and measurement set-up

With respect to used software types, which are Rollscan or μ Scan (μ Scan) software, several properties of signals are acquired. They provide to make characterization of some material properties; composition and microstructural features such as grain size, inclusions, precipitates, dislocations. Rollscan software is the kind of digital noise analyzer. It reads directly total noise like signals and converts them to the Magnetic Parameter (MP) that is also called as raw MBN parameter or MBN emission parameter in some sources. The raw MBN data consists of series of voltage pulses and applied field values obtained as a function of time. They can be converted to actual stress value with proper calibration technique, which should consider and eliminate the effects of other variables. Hence, Rollscan data plays the important role to get the residual stress profile of the specimen. On the other hand, μ Scan software gives the information about MBN fingerprints, frequency spectrum, pulse height

distribution, RMS values of obtained one single signal envelope and representative B-H curves. μ Scan software has an advantage over the Rollscan software. It provides the possibility of adjusting frequency and filtering.

To perform accurate MBN measurement, typical measurement parameters should be considered carefully. Magnetizing voltage, waveform, magnetizing frequency, magnetizing field strength and number of burst are quite significant. At the beginning of the measurement, waveform of the magnetization should be determined. Different waveforms can be used for the alternating excitation field to obtain MBN signals. Most commonly used waveform is sinusoidal. After that, magnetizing voltage should be determined carefully since it affects the magnetic field strength within the material. It can be also varied by changing magnetizing frequency. Changing of the strength value is preferred instead of varying magnetizing voltage for MBN signal analysis. Thus, MBN measurement should be implemented by using properly selected constant magnetizing voltage value. Number of burst indicates the magnetizing half cycles stored for signal analysis and determines the reliability of measurement. Increase in the number of burst causes data that are more reliable.

The other and the most important parameter of MBN measurement is magnetizing frequency. Increase in magnetizing frequency can cause to excite of more domains and increase in the domain wall activity. Because of this, the peak height of the signal and root-mean-square (RMS) values of voltage can also increase. Moreover, magnetizing frequency decides depth of created magnetization. When the other parameters are kept at constant value, penetration of magnetization reduces as increasing in magnetizing frequency. During the magnetization of the ferromagnetic and conductive materials, special Eddy currents are created due to the change in the magnetization direction [50]. Increase in the magnetizing frequency causes to improve the strength of the Eddy currents. This tends to attenuate the MBN signals and they can reach to the limited

depth. The associated depth of measurement is called as skin depth and calculated as [51];

$$\delta = \frac{1}{\sqrt{\pi f \sigma \mu_r \mu_0}} \quad \text{Eq. 13}$$

where f is the magnetizing frequency, σ is the electrical conductivity of material, μ_r is relative magnetic permeability of material and μ_0 is the magnetic permeability of air. Once the proper MBN measurement set-up parameters is chosen, MBN probe is placed on the surface of the material and collect the noise like signals from the skin depth. According to used software, obtained parameters show the variation. As mentioned earlier, Rollscan software analyzes the signal and gives the raw MBN parameter (MP). On the other hand, μ Scan supplies different knowledge about the magnetic characteristic of the material. From this software program, amplitude frequency of one burst, MBN fingerprint, frequency spectrum, pulse height distribution and representative hysteresis curves can be obtained, seen in Figure 2. 17. Among the obtained results, the most important one is MBN fingerprint that gives the graph plotted of root mean square (RMS) values of voltage against the applied magnetic field strength. The height of the graph indicates the domain wall activity whereas the peak position along the x-axis could provide the information about the microstructural features of material.

The other important analyzing result from software is representative hysteresis curves. The sum integral of rectified bursts gives a simulation of the hysteresis loop. From the curves, important magnetic properties of samples such as coercivity, remanence and permeability can be determined. However, they cannot correspond actual values of whole material since material is magnetized locally and saturation of whole material can be different from that of the locally magnetized region.

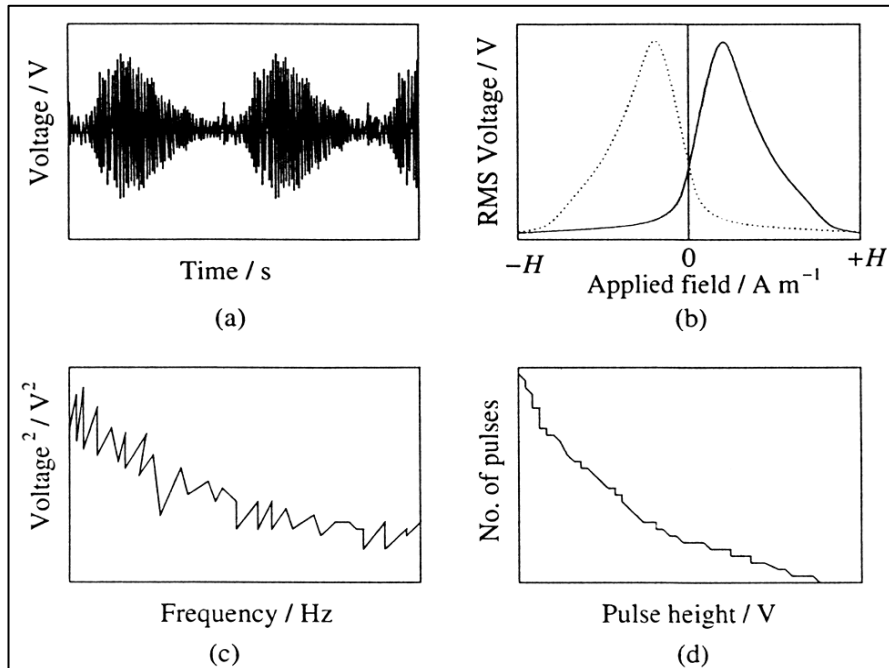


Figure 2. 17 Analyzed parameters from μ Scan software a) amplitude spectrum b)MBN fingerprint c) frequency spectrum d) Pulse Height Distribution

2.5.5. The Factors Affecting the MBN Emission

Barkhausen noise activity is strongly affected by three important material characteristics; microstructure, stress state and hardness. The presence and distribution of stresses influence the direction of the magnetic moments within the domains and they lock into the domain wall movement in their easy direction of magnetization. Microstructure is consisted of grains and phases. Their distribution, sizes and types strongly affect the domain nucleation and the domain wall movement. Hardness is related to dislocation density and impurity atoms in addition to the other microstructural factors such as atomic structure, grain size. Even though MBN is simultaneously affected by the stress, hardness and microstructure, the individual effect cannot be separated, yet. Moreover, some contradictory results exist in the literature.

2.5.5.1. The Effects of Microstructure

Microstructures of the materials are mainly composed of the grains, grain boundaries, phases and some defects, which might be inclusions, voids, cracks, dislocations or some precipitates. The average grain size strongly affects the domain wall movement [52]. Since the grain boundaries act as pinning sites, when the grain size is reduced, domain wall encounters more grain boundaries and this reduces the domain wall energy. Thus, domain wall motion is impeded and Barkhausen noise activity reduces. The same situation is valid with the existence of the microstructural barriers. They pin the movement of the domain wall. In addition, they reduce the velocity of the moving domain wall by decreasing wall energy, and reduce the mean free path. Inclusion is the one of them. It can be particles of a second phase in an alloy, oxide or sulfide particles, holes or cracks, etc. [52]. On the other hand, when it is wanted to define with the magnetic point of view, it could be explained as a region that its magnetization character differs from the surrounding material or it has no magnetization at all. In steel microstructure, cementite (Fe_3C) is accepted as the well-known example of magnetic inclusions. Figure 2.18 (a-d) shows the passage of a domain wall when it encounters the inclusion. From the stage (a) to the (b), closure domains shown in stage (a) are dragged into the form of tubes and it causes the creating new domains at the right of the inclusions. If the domain continues to move further, it leads to broaden the tubular domains shown in stage (c). The conversion of domain walls from (a) to (b) to (c) is reversible that means the domain arrangement of (a) could be reformed if the applied magnetic field is withdrawn. However, further increase in magnetic field do not lengthen of the created tubular domains since increase in its surface area tends to improve the energy of the system. At that point, the main wall suddenly splits off the tubular domains irreversibly and jumps a distance to the right shown in the stage (d). The Barkhausen jump is detected in the form of voltage pulses induced in a used search coil. This mechanism is also valid for the effects of the other microstructural features such as grain boundaries, dislocations or voids on the movement of domain walls [52].

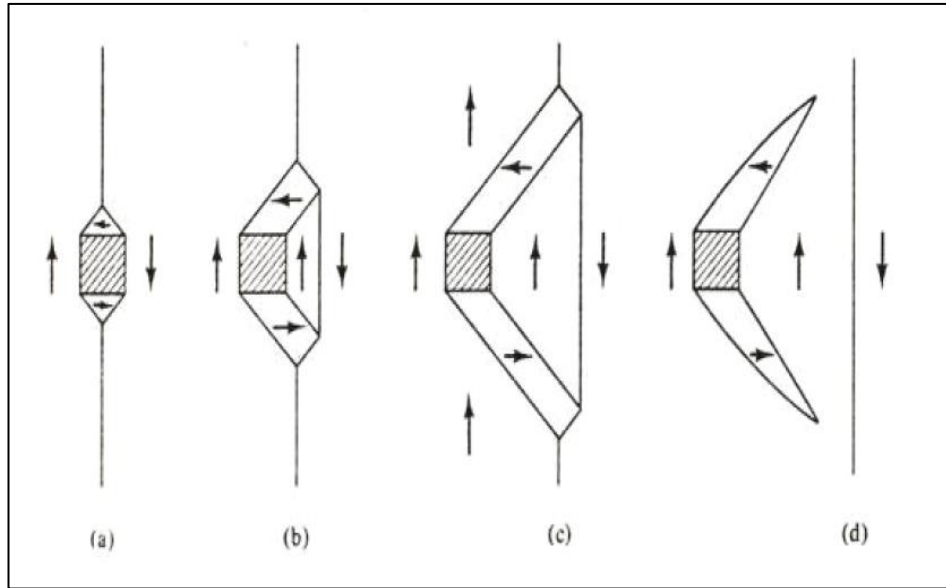


Figure 2. 18 Representative demonstration of interaction between domain wall and inclusions and passage of the domain wall [52].

The most important features of microstructures of the material is phases. As the phases varies, the crystal structure, configuration of atoms and their interaction energies can be changed significantly. Especially in the steel microstructure studied in the study, several phases could be obtained by applying different heat treatment. In addition, the phases have different crystal structures and magnetic properties. Since each phases gives the distinct form of BN envelope, the effect of the different microstructure of steel to the Barkhausen noise signal should be analyzed carefully. The mechanically and magnetically softest phase in steel is **α -ferrite**, which has the BCC crystal structure. In the ferrite structure, only grain boundaries play an important role for the pinning of the domain wall motion unless structure includes much amount of second phase particles. Hence, it causes to require the low magnetic field in order to magnetized structure [48]. Because of the soft magnetic feature of ferrite, ferritic steels gives the higher MBN peak amplitude, lower coercivity and hysteresis loss value.

Normalized mild steels that contain reasonably large grains of ferrite is considered as an example of this situation. The second phase, which must be considered in this part, is **pearlite** that is composed of the alternating α -ferrite and Fe_3C (cementite) laths. If the large variety exists in the magnetic properties of these laths, then the wall movement is pinned by the phase boundary. It tends to enhance the coercivity and cause to enlarge the hysteresis loop. Then, the material becomes to magnetically harder. If the domain walls and the cementite lamellae are aligned parallel to each other, domain walls are more strongly hindered rather than in the case of the lamellae that are aligned normal to the domain walls [53]. Relatively high carbon steel or air-cooled steel can be considered with that point of view. On the other hand, low carbon steel or medium carbon steel may be cooled faster or quenched or surface treated to produce a **martensitic** microstructure that has a fine structure with dissolved carbon. Body-centered tetragonal crystal structure strongly pins the movement of domain walls. Moreover, transformation from austenite (FCC) to martensite (BCT) causes the volume expansion. Then the crystal structure is heavily strained. This tends to increase dislocation density and generate a residual stress. Because of these, the local permeability changes [47]. When the steel, which is composed of the martensite, is examined for the Barkhausen Noise measurement, the MBN signal is much lower than the ferritic and/or pearlitic structure due to the strong hindrance of domain wall movement by the existence of high amount of dislocation density and residual stresses [54]. The RMS values of MBN signals with respect to different microstructures is shown in the Figure 2. 19.

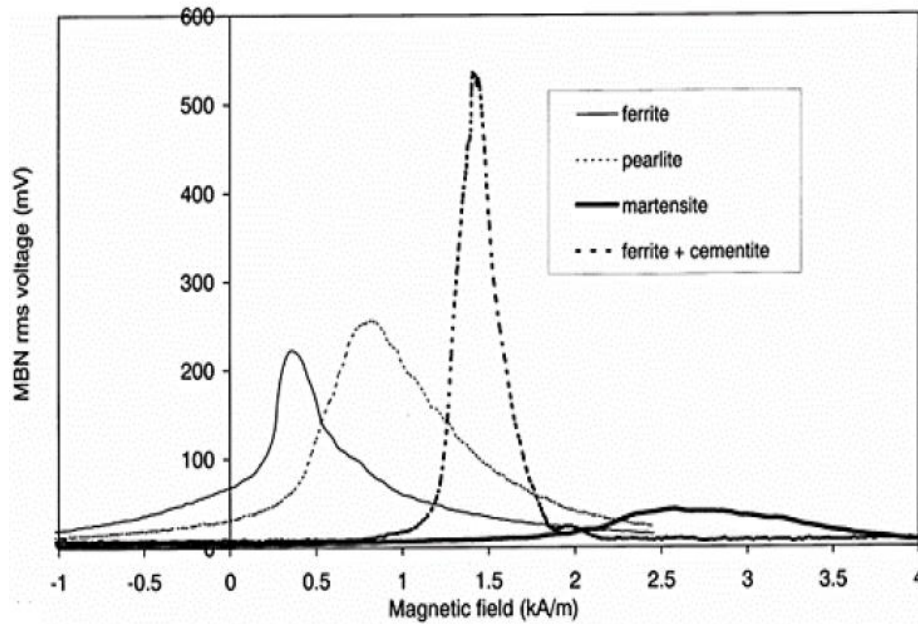


Figure 2. 19 The MBN RMS value as a function of applied magnetic field with different microstructures [54]

The other possible phase generated in the steel microstructure is **retained austenite**, which is a non-magnetic phase. This phase leads to internal demagnetizing field so that the domain walls cannot overcome these areas. Since the austenite is not ferromagnetic, retained austenite in the phase structure of specimen acts as a strong obstacle for the movements of domain walls even in the presence of high tensile stress.

2.5.5.2. The Effects of Stress State

The existence of magnetostriction induced by both an applied mechanical stress and residual stress could alter the domain structure and generate a new source of magnetic anisotropy. This kind of hindrance to domain wall motion can be macro or micro residual stresses. The effect of stress on magnetization is sometimes called magnetomechanical effect. Magnetostriction of material (λ) and magnetic behavior of

material is strongly related to each other under the applied stress [55]. Magnetostriction behavior of materials could be positive or negative. The coefficient of polycrystalline iron is positive at low applied magnetic field (H); however, further increase in H tends to that the magnetostrictive coefficient of iron becomes to zero, then negative at higher fields [41]. When the material, which has the positive magnetostriction coefficient value, is loaded in the elastic region with the tensile direction, increase in the MBN signals reveals in the direction of the applied stress whereas the MBN signals diminish with the application of compressive stresses in the materials [41]. The magnetic behavior of iron under stress is complicated. When considering stress anisotropy of soft magnetic steel generated by the applied or residual stress under low magnetic field, these stresses could be generated in easy axis of magnetization. If the applied tensile stress is considered, domains aligned as parallel with the applied/residual tensile stress increase the volume of the 180° domain wall and hence domain wall activity. In addition, in the case of compressive stress, perpendicularly aligned domains with the compressive stress causes to increase 90° domain walls. These domain walls impede the domain wall movement and reduce the MBN activity. This relationship is shown in the Figure 2. 20 for the positive magnetostrictive materials such as iron. As shown in the right hand side of the Figure 2. 20, tensile stress to the demagnetized specimen, as in Figure 2. 20(b), leads to orient domain walls. They move by the way that to decrease the volume of domains magnetized at 90° angles to the stress axis since these domains have a high magnetoelastic energy. At the situation (c), magnetoelastic energy of domain wall (E_{me}) is a minimum, which provides the requirement of small applied field to obtain single domain structure (case d). And the transition from case (c) to case (d) can be accomplished by the relatively easy process of 180° wall motion. Because of this, it is generalized that both the Barkhausen noise emissions and observed RMS values are increased when the tensile stress state exists for the positive magnetostrictive material. In contrast to this behavior, compressive stress state exhibits opposite effects on them.

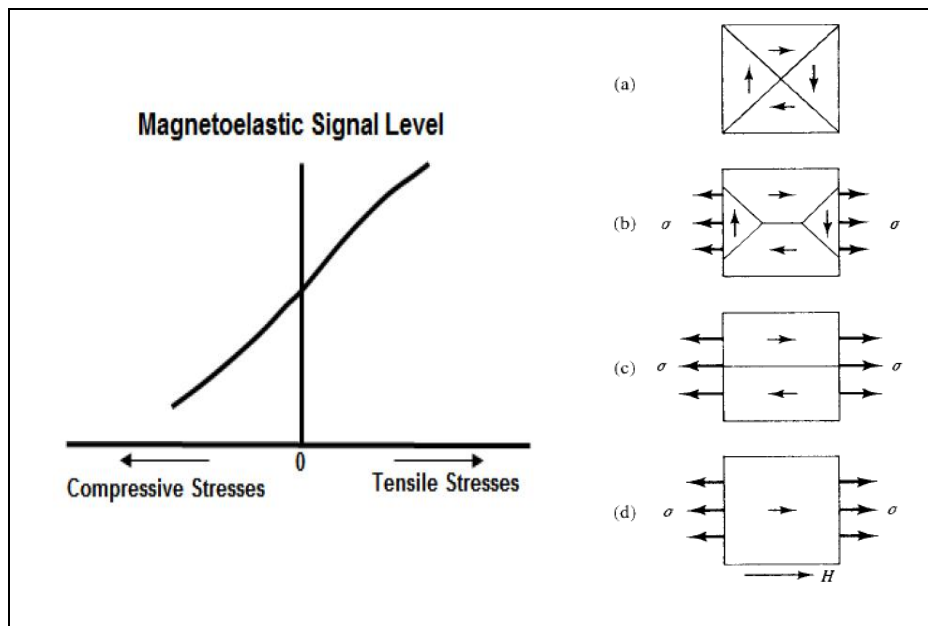


Figure 2. 20 The relationship of MBN signal level under tensile and compressive stresses for the positive magnetostrictive materials [56].

2.5.5.3. The Effects of Hardness

Mechanical hardness of steel is strongly related to dislocation density and carbon amount of steel. High amount of dislocations into the material represents the mechanically hard materials since dislocations prevent the slip mechanism during deformation stages. Under the yield point, elastic deformation occurs. It does not cause the strain and permanent deformation within the structure. On the other hand, beyond the elastic limit, plastic deformation causes the strain that distorts the atoms within the crystal lattice and increases the dislocation density and some crystal defects. They act as pinning sites during the domain wall motion and cost the more difficult magnetization. Because of this, MBN measurement parameters alter significantly. The hysteresis loop rotates clockwise and area of the curve becomes wider. It means that

the hysteresis loss increases and coercivity of material increases. During hardening, some distortion may create. It causes the microstrain in the lattice that impedes both domain wall motion and domain rotation. This means that increase in the mechanical hardness also causes to make difficult magnetization of materials; i.e, soft magnetic materials become hard magnetic materials due to the hardening processes. Unlike the coercivity value, the maximum permeability shows the opposite response when the material hardness is increased. Permeability decreases with even a small amount of increase in hardness. The other factor that affects the hardness of the material is carbon amount. The high carbon steel has higher mechanic and magnetic hardness value. In general, increase in mechanic hardness also enhances the magnetic hardness.

2.5.6. Residual Stress Measurement by MBN Method

The basic set-up of the Barkhausen Noise measurement is simple unlike the theoretical background of it. As demonstrated in Figure 2.16, it is made up of a signal generator with power amplifier, a biasing magnet with an inductive search coil, and a display record device for the data storage. Special C-shaped electromagnet, which is called sensor or probe, is used to generate the time-varying magnetic field by applying alternating current. The strikes or jumps induced by the variations of the magnetic domains are detected by the coil. Then, the signals are amplified and recorded as raw MBN emission data. Obtained data are analyzed and converted to various output forms by a software. For instance, the root mean square (RMS) of the noise is calculated by using the graph of MBN amplitude versus the applied magnetic field strength. During the calculation, some smoothening algorithms can be used;

$$\mathbf{RMS} = \sqrt{\frac{1}{n} \sum_{i=0}^{n-1} x_i^2} \quad \text{Eq. 14}$$

where n is the total number of acquired points and x_i is the i -th sampled Barkhausen signal data. The excitation frequency determines the information depth and volume of the MBN analysis. Two different modes of MBN measurement can be chosen according to the desired information depth. If information from the surface is requested, high-frequency mode (20-1000 kHz) is applied. Contrarily, low-frequency mode (0,1-100 kHz) can be utilized to obtain information from the deeper region. The high-frequency mode is selected, for example, to detect grinding burns in the ground components.

Residual stress monitoring by MBN method is rather complicated since MBN emission is influenced by various measurement and material parameters. This technique strongly depends on the electromagnetic probe, applied field strength, excitation and analyzing frequency etc. In addition to them, material properties, which are mainly microstructural features, residual stress, hardness and geometry of the test component, have a strong influence on the magnetization of specimens. Geometry of the specimens is quite important due to the demagnetization effects of the component that occurs within the magnetized material and decreases the effective field strength. Aspect ratio (length/width) of the specimen determines the strength of this effect and final hysteresis loop. The wider surface area of specimen causes spreading of magnetic field to larger area and tends to dilute the flux concentration [47]. As an example of this situation, MBN measurement comparison of flat bar specimen and gear tooth could be given. Because of the combination of all these parameters, it is required essentially to make proper calibration for each test geometry, microstructure and measurement parameter carefully to determine the single effects of stress on MBN and to access the residual stress values quantitatively.

Moreover, some critical points should be considered carefully during the calibration. Although the measurements are made from a surface, a plane stress assumption is made. Therefore, it is important that the calibration procedure carried out under the biaxial stress condition. It provides to estimate the stress value accurately. If the uniaxial stress is applied rather than the biaxial stress condition, calculated stress values could not correspond the exact value. This situation is taken into consideration with the comparison of the actual stress value. Moreover, it takes account of the fact that local tensile and compressive load should be calculated from the local strain values which are collected from strain gauges when controlled static loading is applied in a suitable loading machine. The strain gauges can be bonded to related region of test samples. It is important for the material that has different microstructures, especially for case-hardened material. In addition, MBN data should be collected simultaneously. Before the calibration tests, it is advised that calibration samples are stress-relieved by proper heat-treatment procedure to eliminate the prior stress effects. Unknown parameters and assumptions, which are taken during calibration and whole measurements, can cause a systematic error for stress measurement.

CHAPTER 3

LITERATURE REVIEW

In the literature, it exists many studies examined the residual stress monitoring by using different techniques. From the metallurgical point of view, the residual stresses could be generated by various processes and significant amount of parameters affect the monitoring of them. In this part of the thesis, several studies in the literature were analyzed and reviewed to create scientific background for the better understanding of the measurement methods of the residual stresses. Some of the researchers investigated and discussed the effects of carburizing parameters on the generated residual stress state and their measurements. On the other hand, some of them examined the residual stress measurement methods individually and then the comparison of these methods were investigated. Many researchers also studied about the accuracy of MBN technique and the parameters that affect the results obtained from MBN technique.

3.1. Effect of Carburizing Parameters on RS

Successful carburizing performance strongly depends on three major process variables: temperature, time and the carburizing atmosphere. They are dominate the carburizing process by varying the mass transfer coefficient and diffusion coefficient of carbon in austenite [57-60]. An increase in the carburizing temperature increases the rate of mass transfer both in the furnace atmosphere and within the steel. It also promotes excessive austenite grain growth. *Karabelchtchikova et al.* [61] studied the

effect of carburizing time, temperature and carbon potential on the kinetic parameters and obtained case depth. They observed that increase in carburizing temperature improves mass transfer coefficient and carbon diffusivity. This causes to allow embedding of more carbon into the surface and diffusing into the material up to deeper region. It means that deeper carburized cases were achieved by operating the higher carburizing temperature. Some researchers examined also another topic related to the effects of the chemical composition of steel on the carburizing kinetics [62]. They examined the different steel grades, which had nearly the same amount of carbon but varying alloy composition; AISI 1018, 4820, 5120 and 8620 steels. The results indicated that medium- and high-alloy steels with high-Cr and low-Ni concentrations significantly had the lower carbon diffusivity in steel. Hence, it was deduced that longer carburizing time provided the desired case depth, and thus, the desired mechanical properties, especially in terms of fatigue and wear resistance. The effect of time and temperature on the total case depth is demonstrated in Figure 3. 1. It is seen that carburizing time and temperature have an additive effect on the case depth [62].

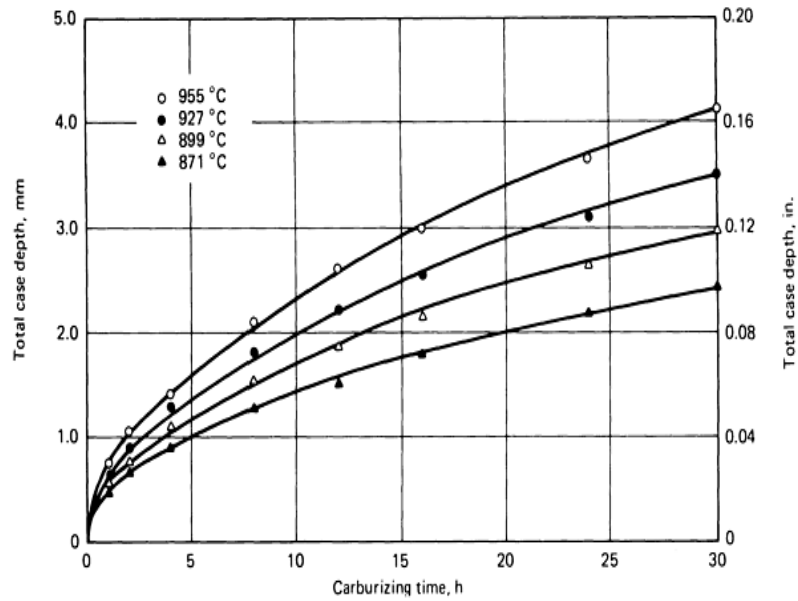


Figure 3. 1 The relationships between the carburizing time and temperature and the total case depth [62].

To observe the effects of carburizing parameters on these mechanical properties, *Asi et al.* performed gas carburizing at 940°C for 3 and 5 hours and at 980°C for 1 and 2 hours. They observed higher microhardness values on the surface of the high temperature carburized specimens rather than that of the low temperature carburized ones. Higher effective case depth was also observed in the samples carburized at high temperature. Similarly, the results indicated that carburizing time also enhanced the deeper carburized case at the same carburizing temperature condition. In the meantime, residual stresses on the surfaces of the specimens were also measured and obtained data demonstrated that the higher compressive residual stress state in the specimen was achieved in the specimens carburized at higher temperature for longer time [63].

Schröder et al. had studied also the residual stress measurement at the subsurface of the carburized C22 steels. Steels had been carburized to obtain 0.2, 0.4, and 0.8 mm, which were achieved by increasing the carburizing time. Then they were quenched from 880°C into the water. Compressive residual stress values increased in parallel with an increase in case depth, and the maximum residual stress location shifts towards the core [64]. Earlier studies stated that the maximum compressive residual stress value is achieved at the little below the surface in carburized steel (Figure 3. 2). *Coleman and Simpson (1950)* [66] and *Hildenwall and Ericsson (1980)* [65] explained that lower value of compressive stress at the surface were caused by the presence of retained austenite content in the surface [65, 66].

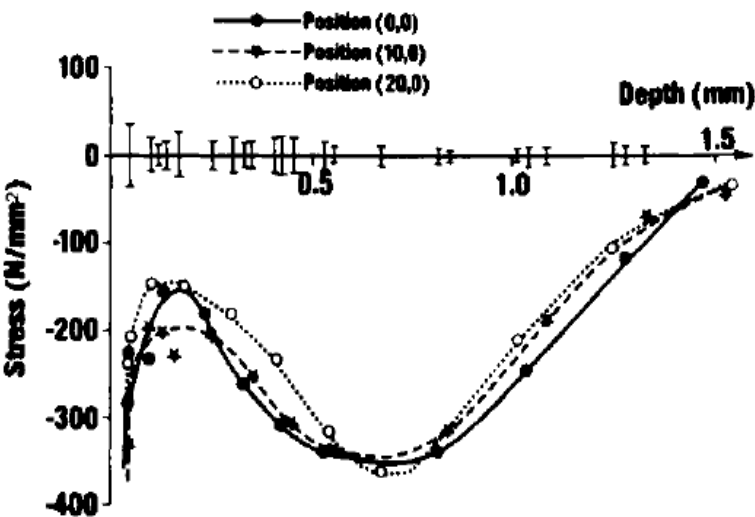


Figure 3. 2 The relationship between stress and case depth in carburized steel which has 0,2%C, 0,77%Cr, 0, 7 %Ni and 0,0 5 7% Mo. 0,8%C in the surface [65].

The other important factors that influence strongly the residual stress distribution in the carburized specimens are quenching and tempering. These have been studied by many researchers. *Coleman and Simpson* investigated the effects of quenchant type on

the stress state of the material. It was stated that a more severe quenching like water quenching instead of oil quenching, leads to give larger compressive stresses [66-68]. It is also supported by calculations in the study of *Ericsson et al.* [69]. The temperature of the quenching medium has a marked effect on the created residual stress since its ability to extract heat changes. When the temperature of water quenchant increases, cooling rate reduces since water loses its cooling power as it approaches its boiling point whereas the reverse effect is observed in the oil quenchant because oil becomes less viscous as the temperature is increased. *Shea et al.* considered the quenchant temperature and it was obtained from the experimental results that an increase in the oil quenchant temperature had increased the compressive residual stress developed on the sample [70].

In literature, effects of tempering on the residual stress state is also interested in some researchers. *Vatavuk et al.* were studied the tempering effects on the residual stresses of carburized specimens. Their hardness results indicated that it did not exist significant variations in hardness of the as-quenched and tempered specimens whereas the residual stresses of specimens differ from each other. Decrease in residual stresses was caused in the higher tempering temperatures due to changing of core microstructures [71]. Tempering at low temperature yields a harder and higher tensile strength for used steels. In other aspect, this type of tempering does not provide the improvement in other mechanical properties such as ductility, toughness, and fatigue life. It was explained by *Parrish et al.* with a reason that the low temperature is not sufficient for the relaxation of crystal structure. Therefore, it does not provide to enhancement of these properties. To achieve desired mechanical properties, the specific tempering temperature for each steel type should be considered carefully [72].

3.2. Characterization of Stress State by Non-Destructive Methods

Residual stress measurement has been gained an importance in both industry and scientific researches. There are several methods to measure the residual stresses; yet, only the X-ray diffraction has the appropriate spatial and volumetric resolution for adequate characterization of residual stress distributions. Many researchers have attempted to measure residual stress state by using X-ray diffraction, or other techniques that have generally been verified by XRD technique.

Burnett et al. applied carburizing process to the cylindrical AISI/SAE 8620 steel of 12.7 mm diameter. A surface carbon content of 1.2 wt% was achieved and then quenched from 927°C in 20°C-oil. Figure 3. 3 demonstrates the variations of tangential residual stress values through the center of the cylindrical specimen. X-ray measurement distribution and finite element method gave the same trend, and nearly the same stress values being valid from the near surface regions of the cylinder [73].

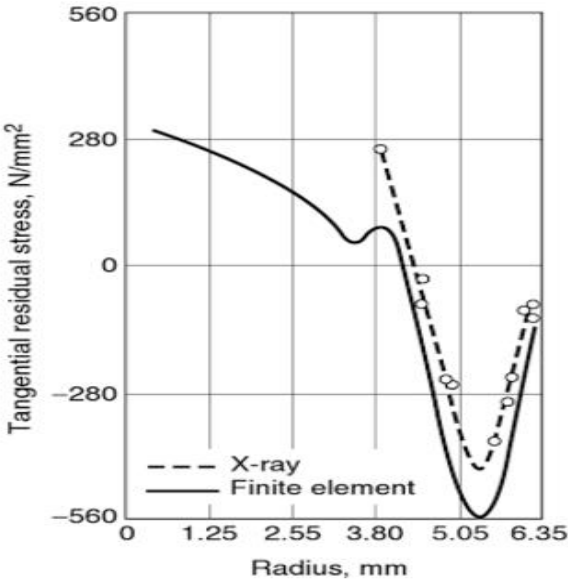


Figure 3. 3 Tangential residual stresses of a carburized cylinder quenched from 927°C in oil at 20°C.; comparison between experimentally determined and calculated tangential residual stresses. [73].

Sorsa et al. were aimed to determine the residual stress and hardness of a case-hardened 18CrNiMo7 steel specimens by using MBN measurement methods and then correlated by MBN simulation model designed by this research group and XRD measurement [74]. Carburizing processes were performed at 940°C for 20h and then tempering was applied. Tempering temperature range was between 180-350°C and the tempering times was in the range of 90-240 minutes. These process variations were designed to create different residual stress and hardness conditions. Obtained results showed that higher hardness tends to reduction of the remanence values which were strongly dependent on the saturating magnetization of the material and hence to the maximum Barkhausen activity. They also observed that increase in hardness caused to decrease Barkhausen activity. After the stress measurements were taken from two different techniques, the stress values were compared. They were highly correlated with each other.

Savaş et al. demanded the monitoring of surface residual stress state in the shot-peened steel samples by MBN methods. The steel samples were shot-peened with variable parameters such as peening intensity, impact angle and coverage values to obtain wide range of compressive residual stress state. They concluded that MBN emission reduced with increase in the magnitude of compressive residual stress. This explained by the reason that the total area of the 180° domain walls were reduced by the compressive residual stresses [75].

L.Suominen and K. Tiitto investigated the shot peened 4330 and 4340 steel specimens by MBN and X-Ray techniques. They performed the uniaxial tension and compression tests to obtain calibration curves for the transformation of the MBN raw signals to the stress values (Figure 3. 4). The MBN and XRD results showed a good correlation [76].

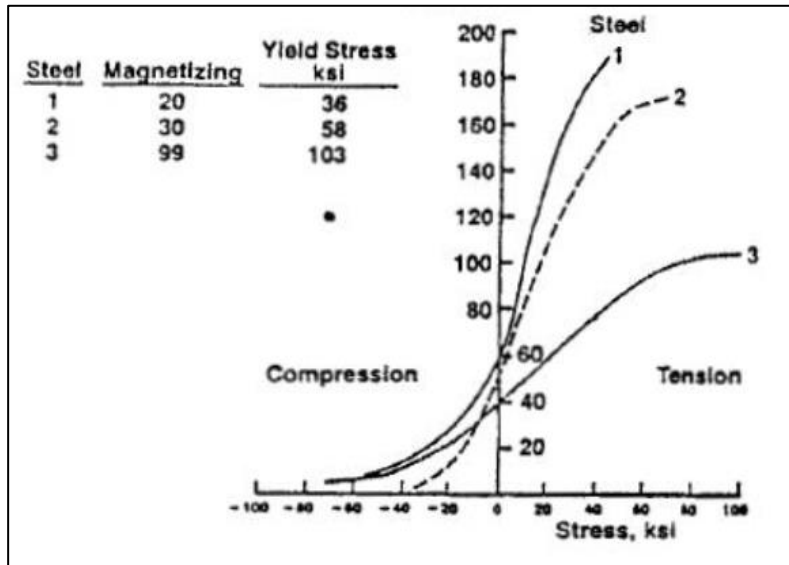


Figure 3. 4 Calibration curves for various steel types showing the relationship between MBN emission and compressive/tensile stress [76].

Hızlı et al. [102] studied the monitoring of the variations in residual stress distributions in the carburized 19CrNi5H steels by using non-destructive and semi-destructive measurement methods, Magnetic Barkhausen Noise (MBN), X-Ray Diffraction (XRD) and Electronic Speckle Pattern Interferometry (ESPI). Although there was a difference in the quantitative residual stress values, the same trend in the variations of residual stress states were observed among the three different measurement methods. Moreover, RMS values obtained from MBN measurements were compared with the residual stress values acquired from the XRD measurements. It was observed that MBN measurements with the optimum parameters gave the good correlation with the XRD measurement.

3.3. Effect of Microstructure on MBN

Moorthy et al. [54] investigated the quenched and tempered 0.2%C steel. Their experiments indicated that MBN signals with two peaks and change in MBN peak

position with different microstructures occurred. A single peak was observed in the samples tempered for 0.5 and 1 hour whereas MBN fingerprints showed two clear peaks in the samples that were tempered for 5 hours. The results were conducted by the presence of two-phase structure within the region where the magnetization was occurred. Moreover, variations in peak position was correlated as a function of tempering time. *O. Saquet et al.* also carried out some experimental studies about tempering induced changes on MBN emission. XC 55 steels were austenitized at 875°C, water quenched and then tempered at various temperatures ranging from 100°C to 600°C, respectively. The peak height of the MBN signal envelopes showed the increasing tendency and they observed simultaneously that the peak positions shifted to lower magnetic fields as tempering temperature increased [77].

Hug et al. [78] also observed two-peak MBN signals. They interpreted these signals to change in percentage of martensite and carbon and existence of two-phase regions. *Gupta et al.* [79] claimed that the broadness of the MBN signals could be changed by the microstructure. *Thompson and Tanner* [80] deduced the same interpretation; however, they detailed the results in such a manner that MBN profile of ferritic–pearlitic steel yielded a single peak in the case of that volume fraction of pearlite was high. On the other hand, the profile was transformed into a double peak when the volume fraction of ferrite increased. *Neslusan et al.* interpreted that peak position was dominantly related to the strength of magnetic field. This means that the shifting of peak to the relatively high field strength value corresponds also the higher pinning strength. The higher magnetic field is required to unpin domain wall to start its motion [81].

Some studies were carried out to establish a correlation between MBN hysteresis curves and microstructural features. From the metallurgical point of view, the

mechanically softer material is used, the narrower hysteresis loop is observed. In addition, mechanically soft structures could be defined as the material consisted of the small volume of the pinning sites of low pinning strength. They also require the high remanence with small coercive force. In contrast, the hard structures have larger hysteresis loops of low remanence and large coercive force [82].

3.4. Effect of Hardness on MBN

MBN emission is sensitive to both hardness and stress. Generally, correlations between the peak height of MBN profile and hardness have been studied in the literature. Another parameter that reflects the MBN behavior is the root mean square (RMS) of the Barkhausen signal. In addition to these, hysteresis loops and some magnetic features obtained from the curves have been analyzed in terms of varying hardness values of related materials [83-88]. Some studies [89-91] have been examined to observe the effects of microstructure and hardness on the MBN signal.

Santo-aho et al. observed that an increase in the hardness of the case-hardened steel bars caused to reduce RMS and peak position values. Moreover, RMS values increased exponentially as the hardness of the specimens reduced whereas increase in the tensile stress led to a linear increase in RMS values [84].

Davut and Gür [89] studied the effects of hardness on the magnetic features of the steel samples. They indicated that coercivity strongly depended on the microstructure rather than hardness. Although, the coercivity increased with increasing mechanical hardness in the stress-free state, compressive stress state was more dominant on the coercive force to reverse the magnetization. It had been shown that peak position was proportional with the hardness instead of coercivity. Good correlation between the peak position and the hardness had also been reported [89].

3.5. Effect of Stress State on MBN

From the historical point of view, the discovery of the relationship between stress and magnetic features was found by *Joule* in 1842 [92]. He carried out several experiments related to the deformation of ferromagnetic materials by applying magnetic field. A several years later, *Villari* tried to change the magnetic properties of ferromagnetic materials with an externally applied stress that was the reverse phenomena of Joule's effect [93]. The last discovery has provided an opportunity for the usage of magnetism in the monitoring of stress state non-destructively. As mentioned in the theory part, applied and residual stresses have significant role on the domain wall movement and hence magnetic features of specimens such as permeability, coercivity and remanence can be changed substantially. Hence, scientists have been interested in this relatively new phenomenon in terms of several parameters.

Krause et al [94] studied the stress dependency of MBN energy under uniaxial tensile loading in pipeline steel specimens. They concluded that tensile strains generated by uniaxial tensile loading caused to improve MBN energy, whereas compressive strains resulted the reduction of MBN energy. Moreover, their study also demonstrated that this increase in MBN energy continued up to some critical stress level where the saturation of magnetization occurred. In the reverse situation, it was observed that the MBN energy variation responses were less sensitive.

The study of *Silva and Mansur* [95] indicated that there is a strong linear relation between RMS value of MBN signals and applied/residual stress values. On the other hand, this relationship deviated from linearity in the case of exceeding the limiting stress value. The same results were observed also in the study of *Wojtas et al*. They interpreted the situation with the stress that approached and exceeded the elastic limit of the material [96].

Peak height of the MBN signal is also influenced by the applied and residual stress state. *Sorsa et al.* also discussed the effect of stress on the peak height and the width of the signals [97]. They observed the increase in peak height during increasing tensile stress. Moreover, the peak position shifted to the lower applied magnetic field strength value.

CHAPTER 4

EXPERIMENTAL PROCEDURE

4.1. Material Selection and Sample Preparation

AISI/SAE 8620 low-alloy, low-C steel was selected since it has high hardenability and provides high toughness in the core after carburizing. This steel is suitable for the measurement of residual stress by MBN method required for ferromagnetic material since possibility of carbide formation that is undesirable for the magnetization is very low due to its low carbon amount. Chemical composition of this steel was determined by arc emission spectroscopy via WAS Foundry Master Spectroscope (Table 4. 1).

Table 4. 1 Chemical composition of the SAE/AISI 8620 steel used (wt %)

C	Si	Mn	P	S	Cr	Ni	Mo
0,22	0,21	0,85	0,009	0,003	0,56	0,47	0,19

All samples were prepared in the premises of the Türk Traktör Company. First, the hot rolled steel rods were machined and ground to the rectangular geometry having dimensions of 165mmx40mmx10mm. Thirty-nine rectangular samples were prepared, and additionally thirteen tensile test samples were prepared with the standard geometry given in ASTM E8-E8M. The diameter and gauge length of them were 12,5 mm±0,5 and 50 mm, respectively (Figure 4. 1).



Figure 4. 1 The specimen for calibration with the standard geometry stated in ASTM E8-E8M

4.2. Heat Treatment Processes

After machining of the samples, first normalizing heat treatment was carried out to relieve residual stresses and to obtain uniform grain size. It was processed in the batch type furnace at 880°C for 3 hours. The process parameters were selected based on the CCT diagram of AISI 8620 steel, obtained by JmatPro software. After three of normalized specimens were chosen as a reference samples that are under stress-free condition, carburizing process parameters were designed carefully to get different case depth and stress state with regard to researches in the literature and processes applied. Batch type atmosphere controlled gas carburizing furnace was used. Carburizing temperature was kept constant at 900°C. Furnace atmosphere composition was obtained by using the mixture of C₃H₈ (g) and the shielding gas (33% H₂, 28% CO, 0,8% CH₄). This gas mixture held the furnace atmosphere with 1.1% C potential initially for two hours that is called boost steep. And then, carburizing process was proceeded with the atmosphere containing 0.8% C, not to exceed the surface carbon concentration of 0.9% C. %C potential of furnace was adjusted by the oxygen probe equipment in the furnace to kept the carbon content at a certain level on the surface of the samples. Samples were carburized for three different 5, 9 and 12 hours separately. After cooling down to the shell oxidation temperature of 880°C, the samples were quenched in oil tank at 60°C. Specimens cool down to this temperature for a duration of 20 minutes. With regard to these heat treatment procedures and parameters, special CCT diagrams were prepared for each set by the JmatPro software (see Appendix A). Tempering treatments were applied at 180°C, 240°C and 600°C for 3 hours, while one

set was left in the as-quenched form. Whole heat treatment processes were shown in the Figure 4.4. Specimens were classified and coded with respect to the applied treatment processes and it is shown on the Table 4. 2.

At the end of the processes, surfaces of samples were oxidized due to quenching and air cooling conditions. To take stress measurement non-destructively, the surfaces should be flat and in the non-oxidized condition. Oxide removing from surface must be applied. In literature, electro-polishing and sand blasting processes were used for this purpose commonly. To observe their effects on the stress state, electro-polishing and sandblasting were applied to two identical specimens, which were carburized at 900°C for 9 hrs and then tempered at 240°C. One of the samples was electro-polished by 20 μm and the other was sand blasted to remove oxide layer. For electro-polishing, A2 electrolyte that was made up to mixture of mainly perchloric acid and water was used. The applied voltage is 30V and the area of polishing is approximately 9 mm in diameter. MBN and XRD methods were carried out to behold the stress distribution of two identical specimens. Rough MBN measurements were applied to these two samples using $\mu\text{Scan/Rollscan 500-2}$ by generating the excitation magnetic field with 125 Hz and 10 V, which corresponds to the information depth of approximately 150 μm (Appendix D, Table D.1). In XRD measurements by Stresstech Xstress 3000 G2/G2R, Cr $K\alpha$ radiation was employed by focusing on the ferrite {211} planes at $2\theta \approx 156^\circ$. The results of both techniques showed that after sand blasting uniform and identical MBN signals could be obtained. Sand blasted and electro-polished specimens gave nearly the same stress values in XRD measurement, but sand blasted specimen gave more uniform MBN signals (Figure 4. 2). Based on these observations from surface, the surfaces of all samples were sand blasted to remove oxide layer.

Table 4. 2 Coding system of the specimens

HEAT TREATMENT CONDITION	TEMPERING CONDITION	CODE of SPECIMEN (*)
Normalized at 880°C	-	N0
Carburized at 900°C for 5 Hour	Not Tempered	C5T0
	180°C	C5T180
	240°C	C5T240
	600°C	C5T600
Carburized at 900°C for 9 Hour	Not Tempered	C9T0
	180°C	C9T180
	240°C	C9T240
	600°C	C9T600
Carburized at 900°C for 12 Hour	Not Tempered	C12T0
	180°C	C12T180
	240°C	C12T240
	600°C	C12T600

(*) 3 identical specimens were produced for each code.

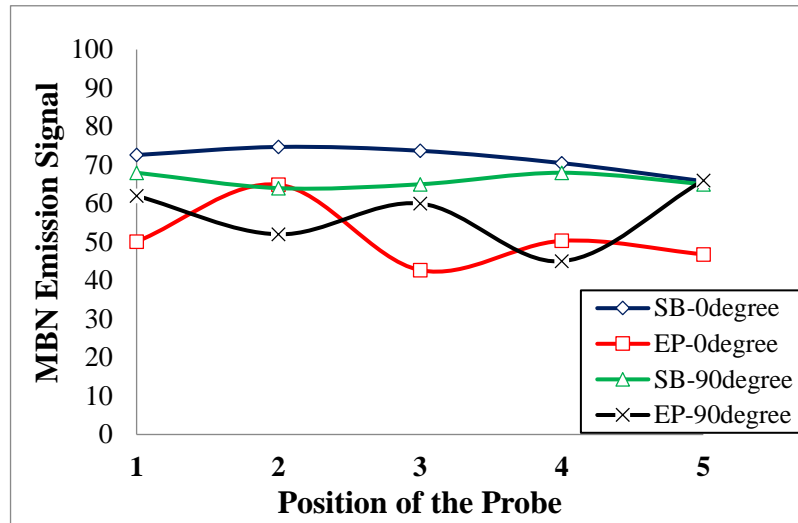


Figure 4. 2 MBN emission parameter distribution for five different positions

4.3. Residual Stress Measurements

4.3.1. Magnetic Barkhausen Noise (MBN) Method

After surface preparation, to obtain symmetrical magnetization and a corresponding symmetrical MBN signal in the magnetizing cycle, all samples were demagnetized in a demagnetizing tunnel. Then, in order to determine the optimum magnetization parameters, four specimens, i.e., normalized, 5 hrs, 9 hrs and 12 hrs-carburized specimens were selected since they represent the range between the lowest and the highest compressive residual stress state.

Then MBN emission signal were taken from the surfaces of each sample by using μ Scan/Rollscan 500-2 by generating the excitation magnetic field frequency with 125 Hz and 10 V. The relations between MBN emission and magnetization gain voltage for each specimen is given in Figure 4.3. The gain was amplified so that smooth sine-waveform excitation could be achieved. Common linear region of these curves gives

the optimum magnetic saturation parameters (Figure 4. 3). Then, 40 dB magnetization gain voltage and 30 for the amplification was selected for the MBN analyses.

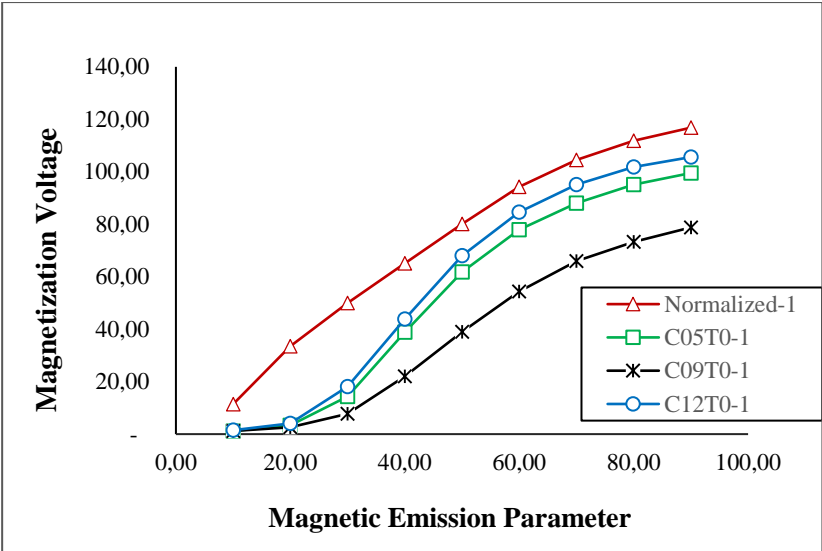


Figure 4. 3 Magnetic saturation curves for the calibration of process parameters

In Magnetic Barkhausen Noise measurements, Stresstech Rollscan μ Scan 500-2 device which is given in Figure 4. 4(a) was used. This device consists of a sensor, a computer and software for data acquisition. Magnetic field was 125 Hz, magnetizing voltage was 10 V, filtering was done mainly between 10 – 500 kHz and the number of bursts was 186. The probe used for the MBN measurements is given in Figure 4. 4(b).

MBN measurement data were taken from both front and back surfaces of all specimen. MBN raw signals were taken from 9 points designated with equal spacing through the axial direction and 5 points marked through the tangential direction with the same distance in three measuring directions, namely 0°, 45° and 90° with respect to rolling direction (Figure 4. 5).

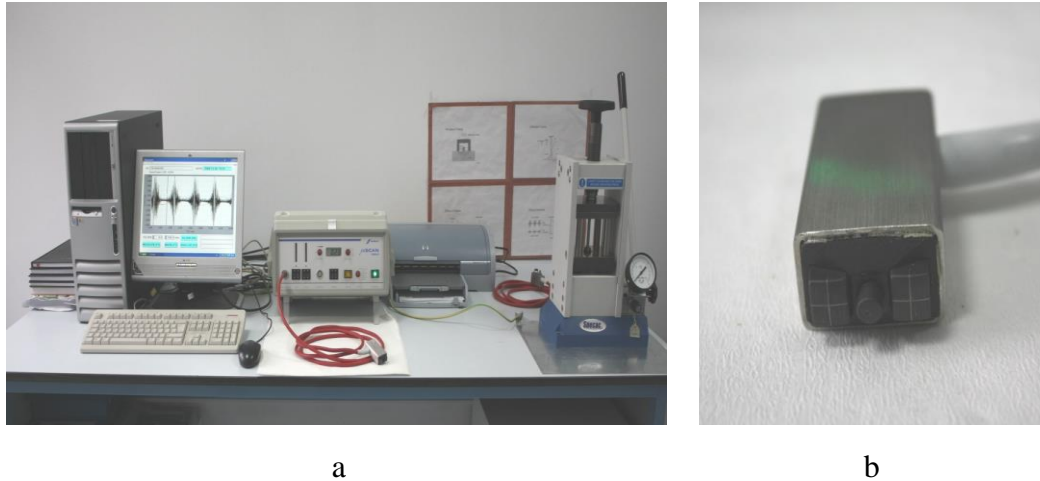


Figure 4. 4 MBN measurement system; a)The Stresstech Rollscan μ Scan 500-2 device Magnetic Barkhausen Noise Equipment b) Probe has more powerful magnetization ability

The central unit of MBN probe has two sensor connectors; Rollscan and μ SCAN. In this study, measurements were carried out using both two-sensor connectors. With Rollscan connector, total MBN signals, which were gathered from many factors, were taken while by using μ SCAN connectors some special features such as RMS values of envelope, hysteresis curves, coercivity and remanence value of material could be obtained. After whole measurements were taken from the decided positions and directions with both Rollscan and μ SCAN, calibration specimens were used to make a connection between raw MBN signals and residual stress value of specimens. For this purpose, thirteen calibration specimens were prepared for each heat treatment condition. They were normalized, carburized and tempered similar to major test specimens. Then they were stress-relieved at 600°C for 1 hours in order to eliminate residual stresses created by applied heat treatment processes

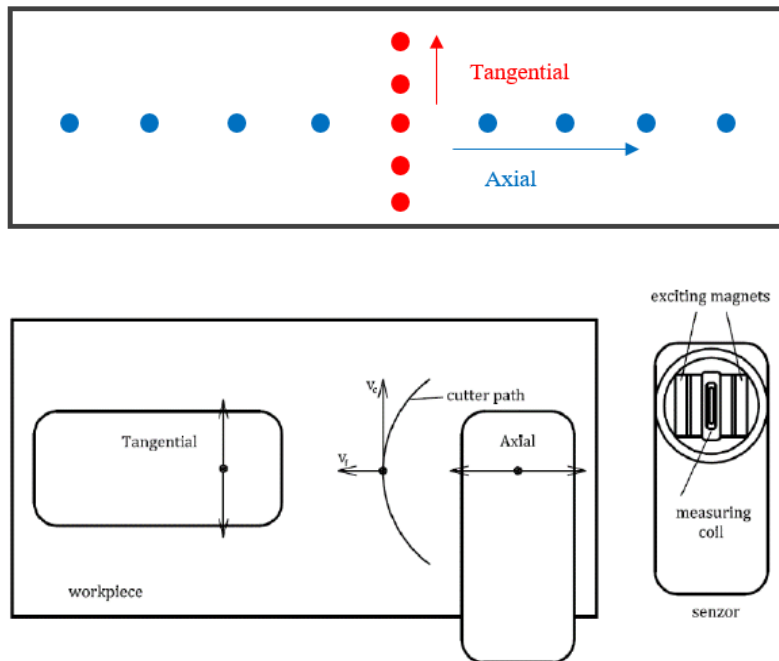


Figure 4. 5 Schematic demonstration of MBN measurement positions

Calibration should be done since raw MBN signals are strongly dependent to many factors such as microstructures, residual stress state, dislocation density, impurity atoms etc. To demonstrate the effects of residual stress state on the domain wall movements and hence MBN signal level, heat-treated and stress-relieved cylindrical specimens were loaded externally. Compressive and tensile load were applied up to ± 20 kN which is the upper and lower value not to exceed yielding point for the hardened SAE/AISI 8620 steels. When specimen was loaded with Zwick/Roell Z300E All- round Universal Testing Machine, MBN probe was fixed on the surfaces of the samples and strain gauges was attached to the other side of surface of the cylindrical specimen (Figure 4. 6).

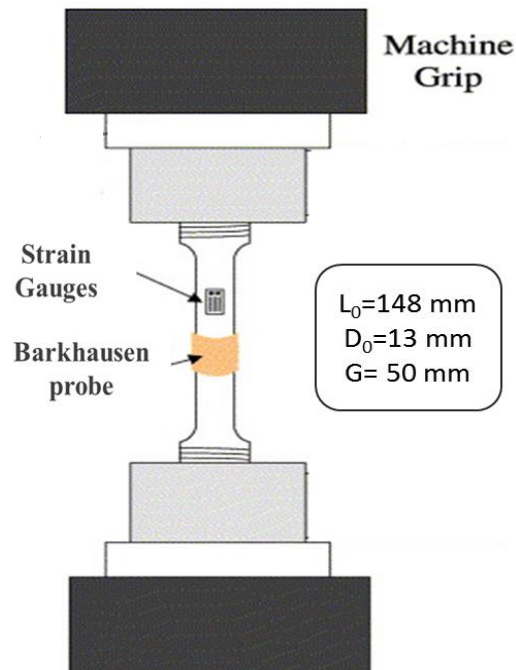


Figure 4. 6 Schematic demonstration of calibration tensile/compressive loading test specimen and the position of the strain gauges and barhausen coil relatively.

MBN probe and strain gauge took data that were MBN parameters and strain values, simultaneously. These test specimens were carburized, so their surface and core had different amount of carbon. Hence, these regions should behave like a different material. Moreover, stress distribution over the cross-section of the test specimen must differ from core to surface. Thus, for each test specimen the actual stress on the surface was calculated by Hooke's law based on the strain value measured via strain gauges. Moreover, surface stress values of each specimen was calculated. Calculated stress values and corresponding MBN signals were used to construct the calibration curves for each sample (Figure 5.19- 5. 22). Since MBN emission signals are influenced by shape and thickness of the material, the estimated stress values were corrected by multiplying shape factor that was obtained by the ratio of MBN signal of carburized rectangular shape specimen and cylindrical shape carburized but not stress-relieved specimens.

At the end of the MBN measurements, the magnetic permeability of normalized and carburized specimens were measured in order to obtain information depth of the MBN measurements by using Eq.13 for the used magnetizing parameters. The electrical conductivity of material (σ) and the magnetic permeability of air (μ_0) were taken from the literature (103). Information depth of normalized and carburized specimens were calculated nearly 100 μm and 150 μm , respectively (see Appendix D).

4.3.2. X-Ray Diffraction (XRD) Method

X-Ray Diffraction (XRD) residual stress measurements were performed by using commercially available XStress 3000 G2/G2R manufactured by Stresstech Group (Figure 4. 7) in the Metal Forming Center of Excellence at Atılım University. To obtain accurate stress value and minimize the instrumental error, device was calibrated by stress-free calibration sample with known material properties given in Table 4. 3. After the calibration, adjustment of the measurement system and the effect of specimen curvature on the results were checked by measuring residual stresses repeatedly at the same point on iron powder. Elastic modulus obtained by tensile test.



Figure 4. 7 XStress 3000 G2/G2R Systems

The X-ray source was Chromium radiation with $K\alpha$ wavelength of 2.289649 Å. Then, to optimize diffracted peak intensity and broadening, proper exposure time, tube voltage and current were selected as 30 seconds, 30 kV and 6.7 mA, respectively. Collimator diameter is important for information depth of measurement. Hence, smallest collimator of 3 mm in diameter was used. The completion of stress measurement from one point was required 20 minutes. Finally, the stress was calculated by the linear regression analysis by considering the slope of the regression line of the lattice strain versus $\sin^2\psi$ plot and multiplying by the elastic modulus of the material.

Table 4. 3 Calibration sample database for XRD measurement

<i>Calibration Sample Database</i>	
Material	Iron
Radiation Type	Cr-K α
Bragg Angle	156.08°
Lattice Plane	(211)
Young's Modulus	211.96 GPa
Poisson's Ratio	0.3

When material has randomly oriented grains, (211) planes could be found at various orientations with respect to the sample surface. To get the d_{hkl} value of (211) planes at every possible orientation with regard to the surface, the sample should be rotated around an axis, which is perpendicular to its surface normal, at a minimum number of two Ψ angles. In this study, specimens were measured by using 5 tilt angles for both negative and positive Ψ angles ranging from -45° and +45°. At each tilt, a 20° scan for (211) plane is performed to obtain the diffraction peak. Three angles were stated for φ axis to obtain stress tensor. 0°, 45° and 90° were selected angles. From the same position with MBN measurement, samples were mounted on the goniometer and XRD

measurement were applied. Modified χ mode was used as a standard measurement mode. Stress values were derived from the change in the interplanar atomic spacing by using special correction methods. These corrections are quite important to localize and determine the maximum peak intensity accurately. Lorentz, Polarization, Background corrections and Smoothing were made in the software program. In addition, cross-correlation method was chosen to localize the peak position. After surface stress measurement, depth profile of residual stress measurement was performed by using Movipol electro 84 polisher by Struers with an A2 acid solution, which were prepared by mixing 50 mL perchloric acid , 500 mL ethylene glycol monobutyl ether, 600 mL ethanol and 200 mL water.

4.4. Metallographic Examination

All specimens were cut to obtain small rectangular samples with 40 mm width and 10 mm in thickness and 10 mm in length for metallographic inspection with standard grinding and polishing techniques that consist of grinding with 240,320, 600 and 800 grit SiC papers and polished by using 3 μm , and 1 μm size diamond suspensions. Microstructures of same samples were also analyzed by using Huvitz HDS-5800 and FEI Nova NanoSEM scanning electron microscopy (SEM) imaging systems to get high magnified images ranging from 1500X to 10,000X with scanning electron microscopy while optical microscope provides magnification ranging from 50X to 1000X with optical system.

Arc emission spectroscopy via WAS Foundry Master Spectroscope was used for the depth profile of carbon. For this purposes, elemental analysis was applied by using layer removal method to carburized samples, which were not tempered, for each 100 microns from case to core.

4.5. Hardness Measurements

Micro-hardness values were taken from the cross-section part of the carburized samples in order to determine the depth of the hardened case. Carburized samples were cut, and sixty indentations along four parallel lines through the cross-section were applied. In micro-hardness measurement, the surfaces should be ground and well-polished. After surface preparation, hardness values were obtained by using Shimadzu HMV-2T. 9.806 N load was implemented for 10 seconds. Moreover, each indentation was taken by controlling the condition that two adjacent indentations were 2.5 times greater than their diagonal and the distance between each indentation from the surface was not greater than the 0.1 mm. The indentation measurement was done at 100X magnification. At the end of the hardness measurement, changes in the hardness values as a function of distance from surface to core region was obtained.

CHAPTER 5

RESULTS AND DISCUSSION

In this part, the residual stresses measured by MBN and XRD methods are compared considering variations in %C, microstructure and hardness. First, effects of the heat treatment processes on the microstructures were discussed and their expected effects on the stress state on samples were analyzed. Then, MBN measurement results were examined in two parts; Rollscan and μ Scan. Residual stress value that was derived from signal obtained by Rollscan and developed calibration systems were introduced. Next, XRD residual stress results and depth profile with respect to carbon content, stress value and hardness measurements were examined, respectively. Finally, the optimum measurement method for industry was decided for residual stress measurement.

5.1. Microstructural Results

In this part, expected microstructures after heat treatment processes were discussed and compared with the microstructural results obtained from optical and scanning electron microscope. To predict the phases that are present in the case and core region of carburized steel before specimens were cut for the metallographic examination, special CCT diagrams should be used. For this purpose, CCT diagrams were drawn for the specimens, which were only carburized for five, nine and twelve hours. They were evaluated separately since carbon content of them at their case regions are not

the same. To construct these CCT diagrams, JMatPro the Materials Property Simulation Package and Sente Software were used. Both CCT and phase distribution diagrams were shown in Appendix A in Figure A. 1, Figure A. 2 and Figure A. 3.

As shown in these diagrams, at the room temperature, 5-hrs carburized specimens could include insignificant amount of retained austenite phase whereas 12-hrs carburized specimen showed the highest amount of retained austenite as nearly 15 wt% in the case region. This situation is compromised with the carbon content of the 12-hrs carburized specimens since they had the highest carbon amount at the case region. Increase in the carbon content reduces the martensite start and finish temperatures to lower values. If martensite finish temperature is below the room temperature, some austenite phase remains as the metastable phase in the microstructure after quenching.

To observe phases and their distributions between the case and core regions, optical microscope images were taken from both case and core regions with the 1000X magnification. Figure 5. 1 shows the optical microscope images of core regions of only carburized samples; normalized, 5-hr, 9-hr and 12-hr carburized ones. As observed in there, microstructures of all specimens at the interior part are all the same nearly and they consist of ferritic-pearlitic-bainitic microstructures. From the CCT diagram of SAE/AISI 8620 steel (Figure 2. 4), in the case of furnace cooling, it is expected to have ferrite and pearlite phase in the microstructure. On the other hand, air-cooling tends to create additional bainite phases due to the faster cooling characteristic. As expected from the CCT curve, normalized specimens have the phase mixture of ferrite, pearlite and bainite phases in the core regions (Figure 5. 1, case a,b,c,d).

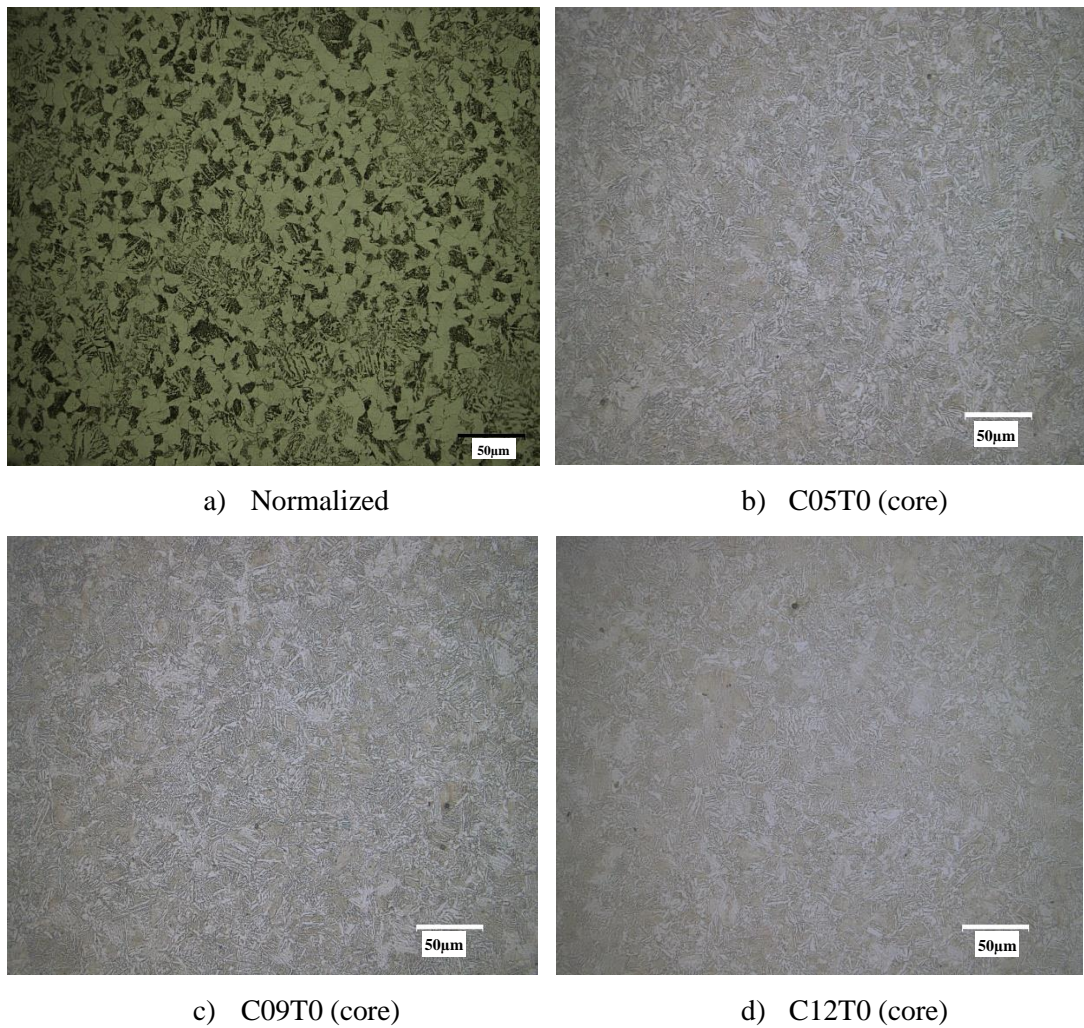


Figure 5. 1 Optical micrographs (1000X) taken from core region of the samples

Once the thermochemical treatment and quenching operations, microstructures of case regions converted to the typically martensitic and tempered martensitic structures for the SAE/AISI 8620 steel specimens. Representative micrographs of case regions of only carburized specimens are shown in Figure 5. 2. As expected from the CCT diagram of each specimen, martensite should exist as a dominant phase in all of them and this is observed in all micrographs of only carburized specimens. It is observed that the carburized samples have a martensitic structure in the case region. Especially in 12-hr carburized specimens, retained austenite could be seen, the white

areas in Figure 5. 2. Tempering was also applied for these specimens with three different temperatures to observe both reduction in hardness and residual stress. From the simulated CCT diagrams of 5-hr, 9-hr and 12-hr carburized specimens, decrease in the martensite start temperatures was observed clearly. In 5-hr carburized ones, this temperature is simulated about 240°C whereas it decreases down to nearly 190°C in the 12-hr carburized ones.

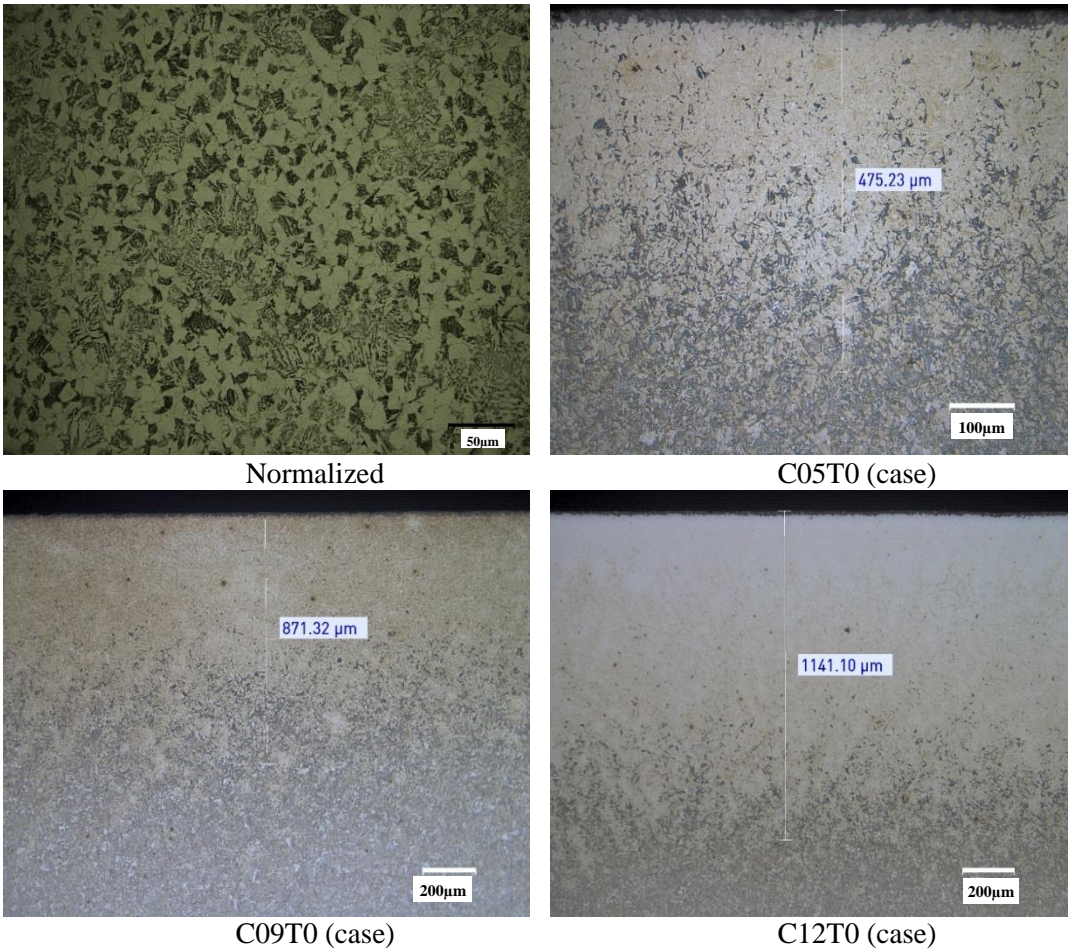


Figure 5. 2 Optical micrographs (1000X-500X-250X, respectively) taken from case region of the samples

When considering the tempering at 180°C, any phase transformation might not be expected since this temperature is not enough for both the diffusional and martensitic transformations. On the other hand, as mentioned in the theory part, tempering at 180°C causes the ϵ -carbide precipitation, and decrease in the tetragonality of the martensite phase partially. At this temperature level, ϵ -carbide has the hexagonal close-packed crystal structure that has the better lattice-matching characteristic with the matrix. Therefore, the coherent nucleation can occur without much strain energy and causes the reduction in prior strain. Because of this type of carbide precipitation at this temperature level, some amount of relaxation of strain occurs although microstructural changes were not observed.

On the other hand, 240°C temperature is above the martensite start temperatures of all specimens. Hence, both microstructural changes and relaxation of stress occur during tempering at 240°C. At the tempering at 240°C, retained austenite phase in the case region of 12 hour carburized specimens could transform to martensite phase or it might be transformed to even bainite phase if the kinetic requirements of this transformation is provided. Moreover, ϵ -carbide converted into the cementite that has the plate-like structures in the microstructure with dimensions of approximately 200 nm long and about 15 nm thick. The cementite is nucleated at the interfaces between ϵ -carbide and the matrix. This also causes to decrease dislocation density. However, the variation in microstructures mentioned above could not be identified clearly in optical microscope. So, SEM micrographs were examined carefully (Appendix B).

Upon further increase in tempering temperature or tempering time, stage four could be defined as carbide coalescence stage. At the 600 ° C, tempering leads to become sphere like-martensite and carbides. Moreover, this temperature tends to decrease nearly complete residual stress within the structures. The microstructural examinations of

these carburized AISI/SAE 8620 steel specimens indicated that when the tempering temperature is above the martensite start temperature of the steel, martensite phase start to transform to obtain more stable phases in the structure (Figure 5. 3 – 5.5). Moreover, upon further increase in tempering temperature yields the decrease in the hardness and compressive residual stress values of specimens. However, these variations could not be observed with the metallographic examinations. They were considered in the following sections of this chapter.



Figure 5. 3 Optical micrographs (1000X) taken from case region of the carburized (900°C/5hrs) samples after tempering at 180°C for 3 hrs.

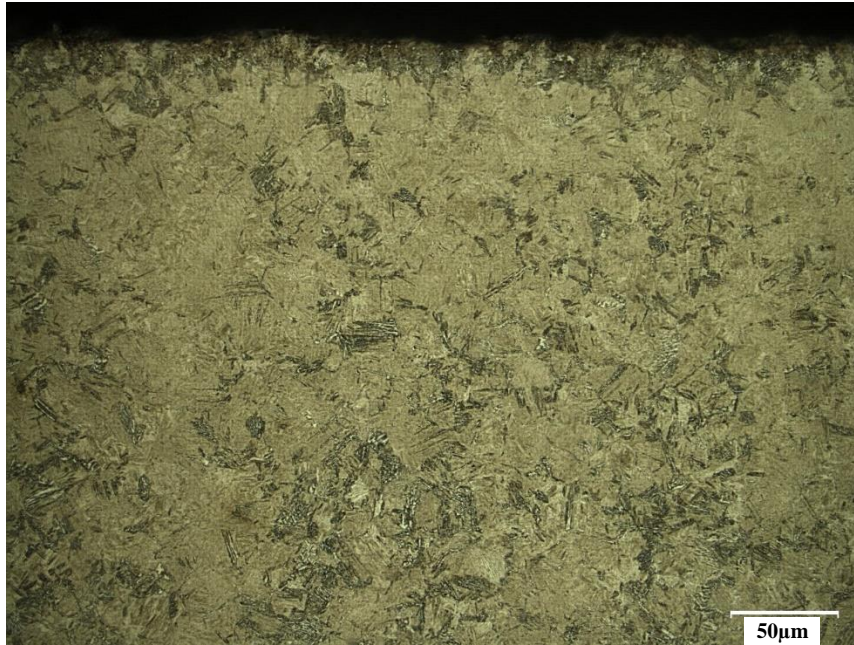


Figure 5. 4 Optical micrographs (1000X) taken from case region of the carburized (900°C/5hrs) samples after tempering at 240°C for 3 hrs.

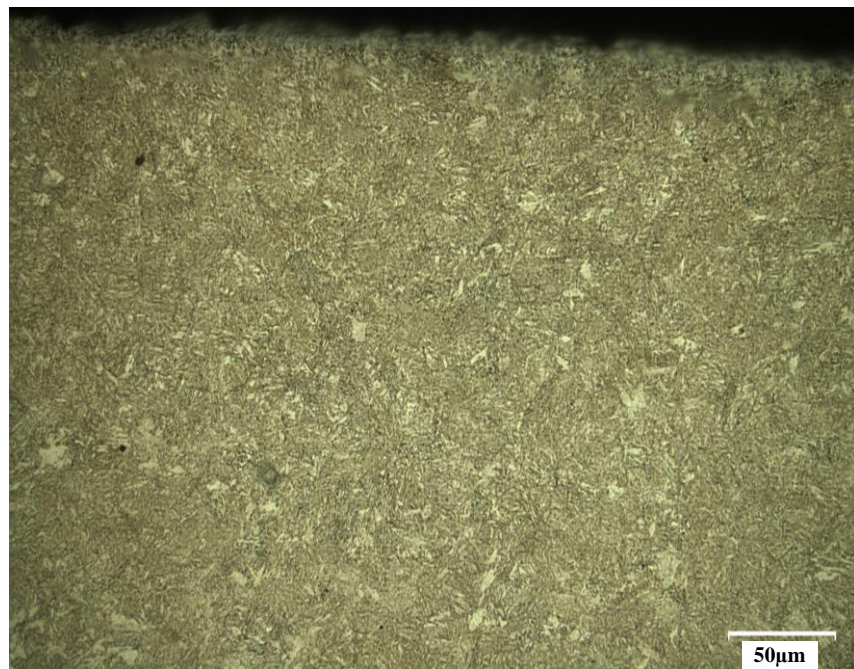


Figure 5. 5 Optical micrographs (1000X) taken from case region of the carburized (900°C/5hrs) samples after tempering at 600°C for 3 hrs.

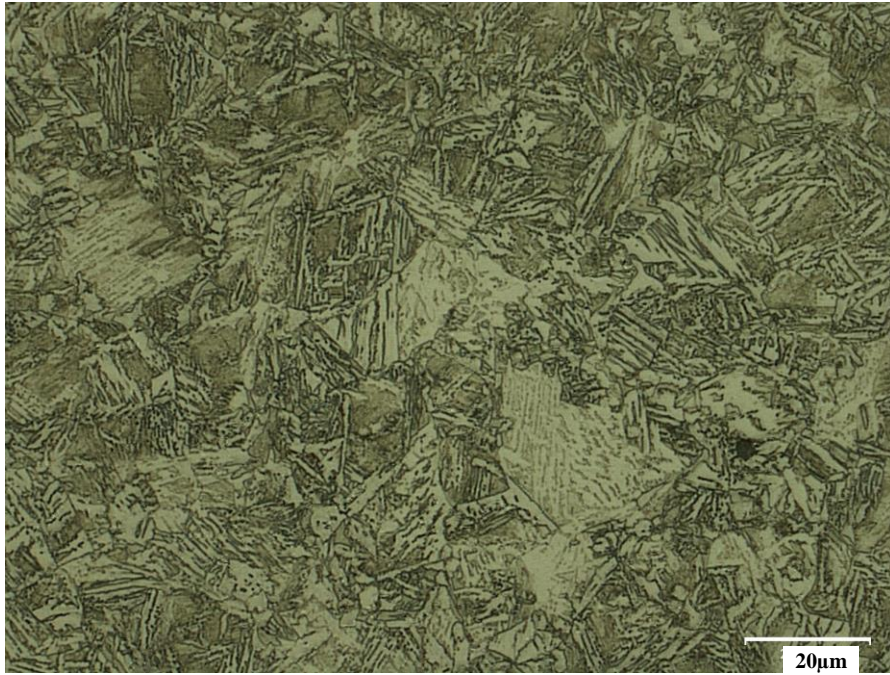


Figure 5. 6 Optical micrographs (2800X) taken from core region of the carburized (900°C/5hrs) samples after tempering at 180°C for 3 hrs.

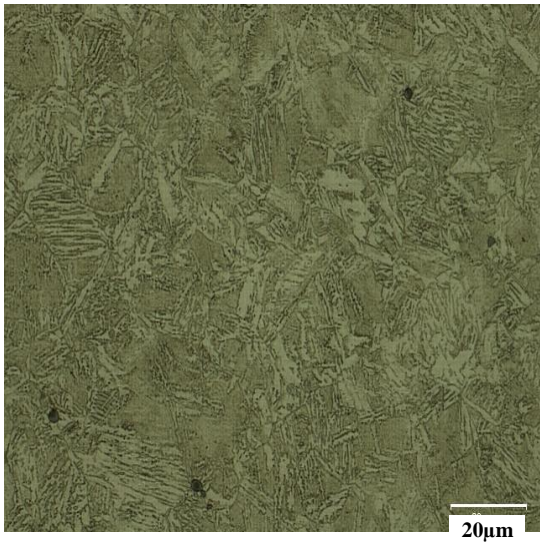


Figure 5. 7 Optical micrographs (2800X) taken from core region of the carburized (900°C/5hrs) samples after tempering at 240°C and 600°C for 3 hrs.

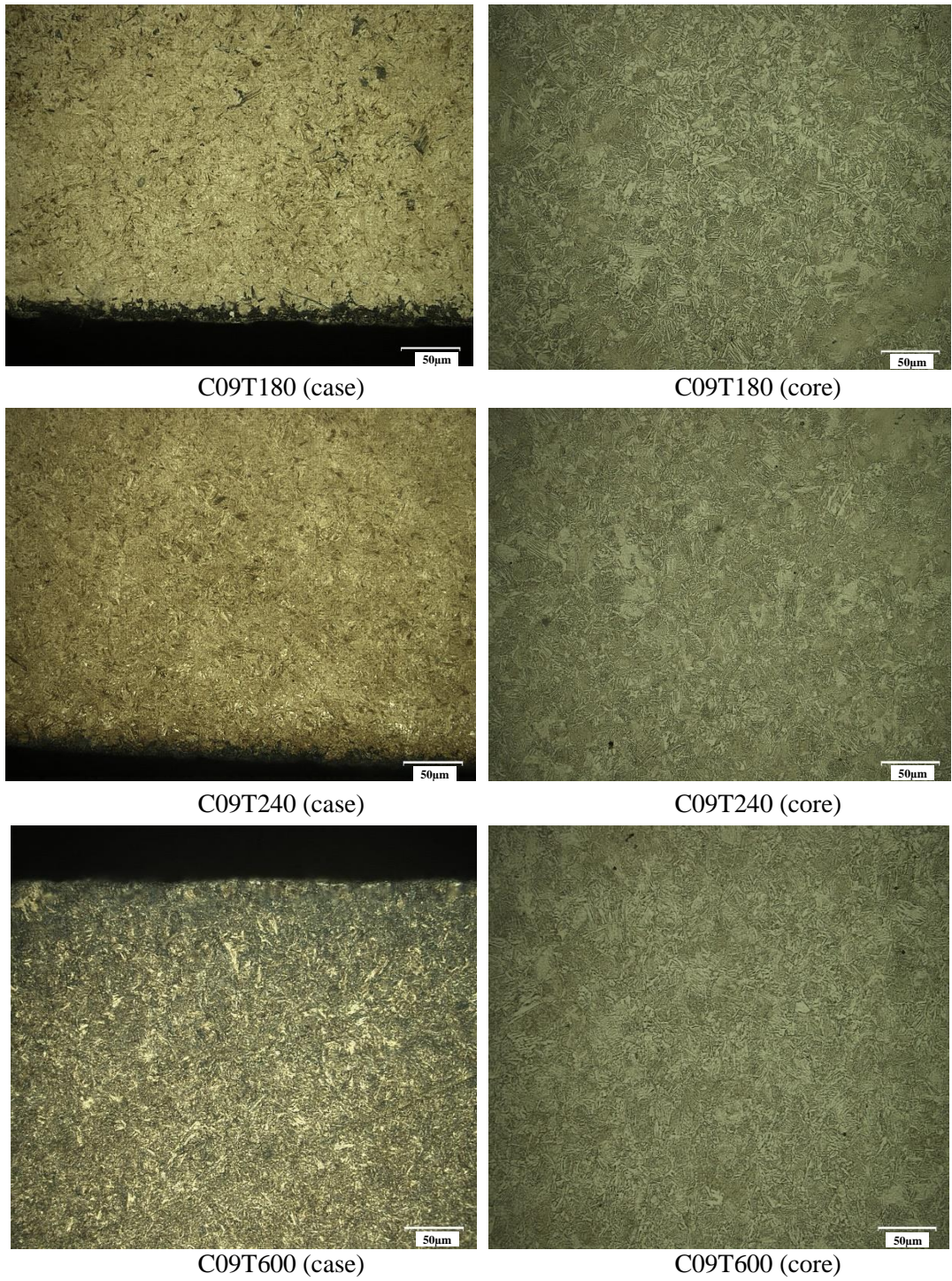


Figure 5. 8 Optical micrographs (1000X) taken from case and core region of the carburized (900°C/9hrs) samples after tempering at 180°C, 240°C and 600°C for 3 hrs.

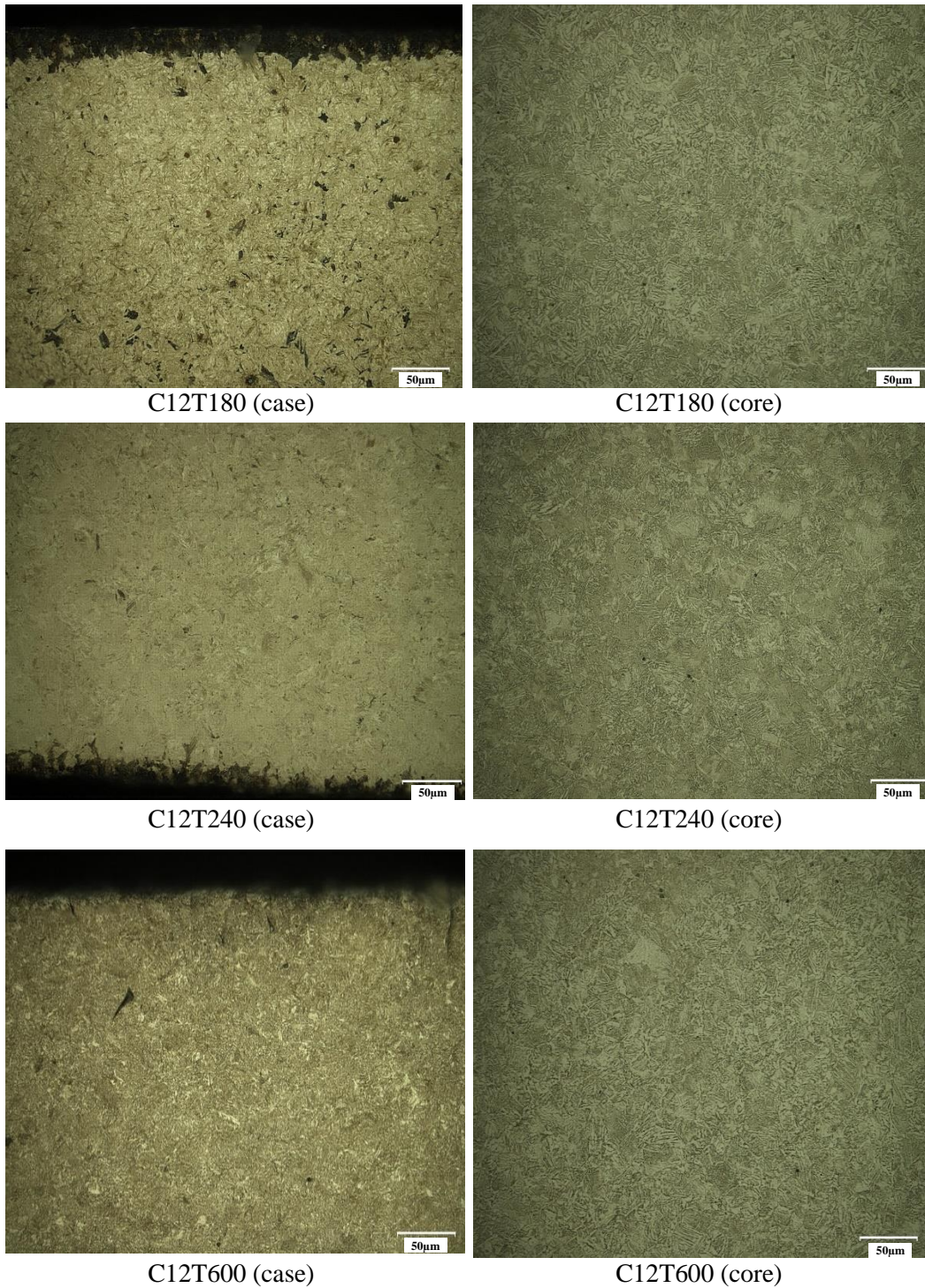


Figure 5. 9 Optical micrographs (1000X) taken from case and core region of the carburized (900°C/12hrs) samples after tempering at 180°C, 240°C and 600°C

5.2. Case Depth Analysis

The case depth is an indication of the process success. Case depth depends various parameters such as carburizing time, carbon diffusivity in austenite phase, carbon potential of furnace etc. According to literature, case depth should be determined by doing elemental carbon analysis, micro-hardness measurements and measuring the residual stress values down to a certain depth [65, 66, and 102].

5.2.1. Depth Profile of Carbon Content

Surface layer removing of the five, nine and twelve hours carburized specimens were prepared by machining with 100 μm steps. From surface to core, step wedge samples surface was analyzed elementally. Figure 5. 10 shows the depth profile of percent carbon with four different carburizing condition.

Literally, surface hardened steel have optimum amount of carbon content that is generally about 0.8-0.9%C. This surface carbon amount gives the maximum hardness value. Effective mechanical properties of hardened sample are obtained up to some critical distance from surface that is called effective case depth. This effective case depth is also defined as 50 HRC (500 HV) hardness value. It is known from to the relation between carbon content and hardness value in literature that 50 HRC hardness corresponds to the steel, which includes approximately 0.4 weight percent carbon. As seen in Figure 5. 10, surface carbon content of nine and twelve hours carburized samples are nearly the same, whereas five hours carburized one has lower surface carbon content which is nearly 0.8 wt. %. Moreover, as expected, normalized specimen has a uniform carbon content along its thickness. Corresponding effective case depth values of 5, 9 and 12-hr carburized specimens are 400 μm , 850 μm and 1100 μm , respectively.

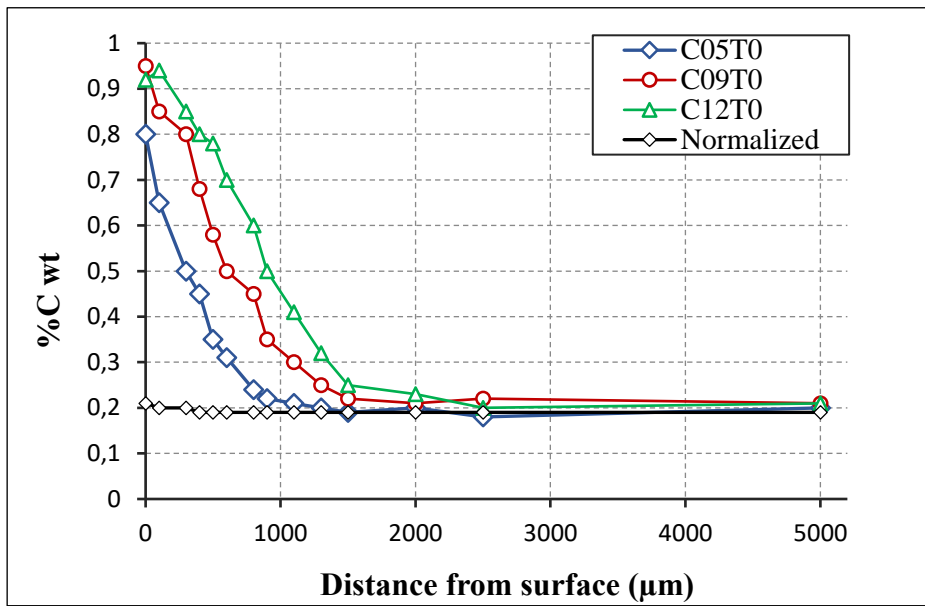


Figure 5. 10 Variation of depth profile of % C in SAE/AISI 8620 steel with carburizing time at 900°C

5.2.2. Depth Profile of Micro-Hardness

Micro-hardness values of thirteen samples which were exposed to different heat-treatment condition were taken from both case and core region in many times. Case hardness values was intentionally taken from the 150 µm below the surface to compare the MBN emission signals accurately since skin depth measurements indicated this value as an information depth. Moreover, average values of them were tabulated on the Table 5. 1.

The depth profile of hardness is very important for evaluating the success of carburizing and tempering processes. As seen from Figure 5. 11, case hardness values increase with increasing carburizing time as expected from the theoretical knowledge and the results of microstructural and chemical composition analysis. In 5 hour carburized and not tempered specimens, 680 HV (approximately 58 HRC) case

hardness value was obtained as an average whereas 12 hour carburized and not tempered specimens have 820 HV (approximately 63 HRC) case hardness value. This increase is caused by the higher dissolution of carbon in the austenite phase at the carburizing boost stage in the controlled atmosphere furnace. This result is also coincided with the surface carbon amounts of these specimens. The longer boost stage causes the more amount of dissolution of carbon and the diffusion into to deeper region.

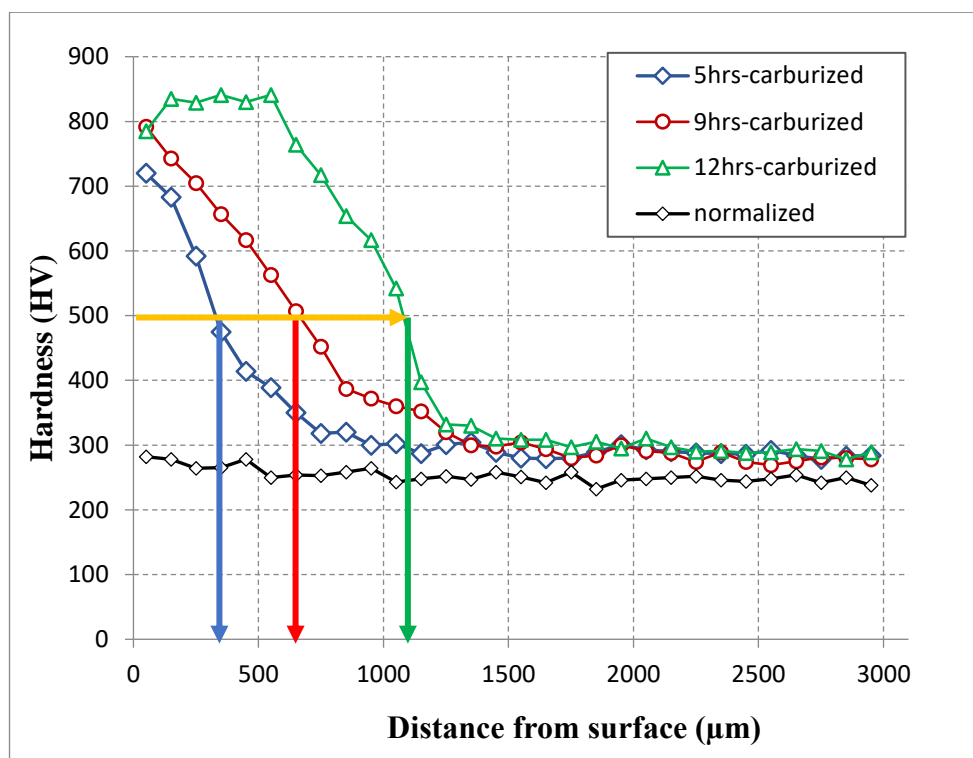


Figure 5. 11 Variation of depth profiles of hardness in SAE/AISI 8620 steel with carburizing time at 900°C

Table 5. 1 Average micro-hardness value of core and case regions of the heat-treated samples

Sample Code	Case Hardness (Average) HV	Core Hardness (Average) HV
Normalized	230	218
C05T0	680	280
C05T180	566	265
C05T240	510	268
C05T600	368	240
C09T0	702	280
C09T180	656	263
C09T240	669	250
C09T600	394	248
C12T0	820	290
C12T180	747	280
C12T240	600	310
C12T600	366	252

As going from the surface to the core region, decrease in the hardness values was observed as expected from the theoretical knowledge. This decrease is caused by the decrease in the martensite volume fraction in the microstructure. Amount of percent carbon is main factor to obtain higher amount of martensite and hardness value. As amount of weight percent carbon increases, hardenability of steel also increases. When the relation between % C and hardness values are considered, seen in Figure 5. 10 and Figure 5. 11, intercompatibility of them is observed. Moreover, microstructures of these samples prove this result.

On the surface of 12-hr carburized specimen, the highest carbon potential, 1.1 wt %C, was achieved due to longer carburizing time. It is known that, hardenability of steel increases as carbon amount of material increases up to some critical level. This critical level depends on the martensite start (M_s) and finish (M_f) temperatures that are also significantly influenced by carbon amount. After some certain amount of carbon, austenite phase cannot be transform into martensite phase since temperature reduces below room temperature even below 0°C. In this case, some amount of austenite phase is retained in the final microstructure at room temperature. Because of the presence of retained austenite, hardness values of that related region is lowered. This specific case was observed in the 12-hr carburized specimen at the surface and near surface region. In these regions, wt % C and hardness values were measured as 1.1%C and 780 HV, respectively. However, at about 200 μm depth, hardness reaches maximum value which is nearly 830 HV and then starts to decrease (Table 5. 1). Effective case depth is defined as distance from surface to layer that has 550 HV in ISO 2639 Standard [98]. This certain hardness value corresponds to 350 μm , 600 μm and 1050 μm in 5-hr, 9-hr and 12-hr carburized samples, respectively.

The results of tempered samples showed that expected decrease in the sample, which has the highest tempering temperature, was observed. Upon tempering, martensite losses its tetragonality which lowers the lattice distortion, dislocation density and residual stress. After the combined effects of these three reasons, reduction in the hardness values of tempered samples was observed. At 180°C, only dislocation density, however, at 240°C all three factors become effective for hardness reduction since 240°C is above the M_s temperature some of the retained austenite transformed to transformed to martensite. At 600°C, martensite morphology totally changes. Needle or plate like martensite shape converts into the spheroidized form that means softening of the structure.

During carburizing, carbon is embedded into surface of the specimen in order to obtain high hardenability in those surface regions whereas core region is maintained at the base carbon level. This provides harder region at surfaces of the material due to the higher martensite amount. Martensite is harder since it is generated by diffusionless shear phase transformation and this transformation causes lattice distortion and internal stresses inside the material. Moreover, martensite is supersaturated solid solution in ferrite, which leads to solid solution strengthening effect. Totally, high dislocation density caused by lattice distortion, high internal stress and strengthening by solid solution yield the high resistance to local plastic deformation which is called hardness. It is well known the fact that carburizing provides high surface hardness and longer carburizing time leads to improve this hard layer into the deeper region from the surface; i.e., it increases the case depth of the carburized samples. The other heat treatment process, which was also used in this study, is tempering. It also influences the hardness of the material by changing internal stress state of the material and morphology of martensite. Upon tempering, martensite losses its tetragonality which lower the lattice distortion and dislocation density and confined internal stress are relieved after some critical temperature.

5.2.3. Depth Profile of Residual Stresses

Depth profile of residual stresses is another prominent criterion to access desired properties. XRD and MBN methods provide information about a limited depth that are 10 μm and nearly 150 μm , respectively. To measure residual stresses in the deeper region, higher energy beams such as synchrotron and neutrons are necessary. However, these techniques are quite expensive and their accessibility is limited. Thus, XRD measurements can be applied by successive layer removal. Layer removal is generally performed by electro polishing method. However, underlying stresses are altered after each layer removal due to local relaxation. This leads to change in the actual residual stress value at related depth locally. Hence, some mathematical

corrections on the measured residual stress values are required [99]. For a plate shaped sample, Sikarskie [100] suggested that

$$\sigma_{z1} = \sigma_{m(z1)} + \left(-4 \times \sigma_m(H) \left(\frac{\Delta z_1}{H} \right) \right) + \left(\sigma_m(H) + 2H\sigma'_m \left(\frac{\Delta z_1}{H} \right)^2 \right) \quad \text{Eq. 15}$$

Where H is the original plate thickness, σ_m is the measured stress, z_1 is the new exposed surface position and Δz_1 is the thickness of the layer removed. To apply Eq. 15, stress values were correlated due to the relaxation of some amount of residual stresses. However, this equation does not correspond the layer removal processes used in this study. It is based on the layer is removed from whole surface, but in this study, only small region was removed by electro polishing since further layer removal from some critical depth EP leads to increase roughness of the surface. The resulting roughness causes to relax locally the in-plane residual stresses. Etching also causes the formation of other defects, such as etching pits. For these reasons, applying correction on XRD residual stresses did not give the sensible results. Corrected depth profiles of XRD residual stresses were shown in Figure 5. 12. It is seen that residual stress state dramatically alters when the method proposed by Moore and Evans [99] is applied upon 300 μm .

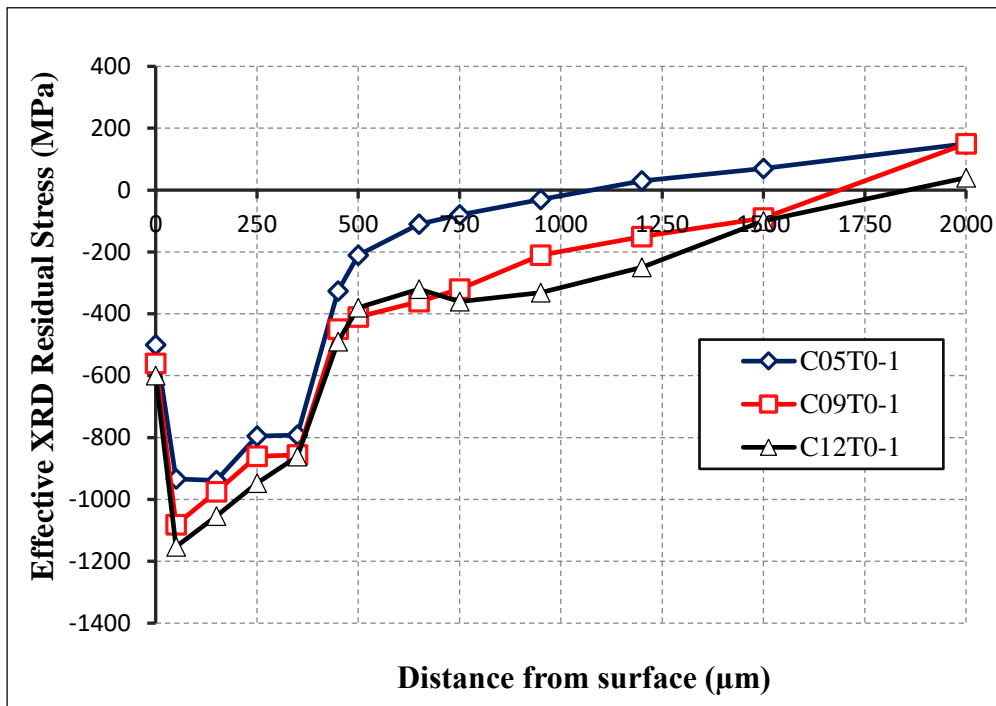


Figure 5. 12 Depth profiles of the effective RS obtained by XRD method for the carburized AISI/SAE 8620 steel at 900°C for different carburizing times (5, 9 and 12 hrs)

The maximum compressive residual stress was seen at the underneath the surface of the carburized sample rather than at the surface. Hence, slight increases were observed for all three samples. Compressive type residual stress state continued down to 1100, 1600 and 1950 µm from the surface for 5, 9 and 12-hr carburized specimens, respectively. This situation is based on the time-dependence of diffusion mechanism. As carburizing time increases, the penetration depth of C-atoms increases. In addition, compressive residual stress state lasts up to this deeper layer. As it is seen from Figure 5. 12, the effective case depths of the carburized specimens are 400, 850 and 1100 µm for 5-hr, 9-hr and 12-hr carburizing, respectively. These values were obtained from the depth profiles by assuming that the residual stress of the normalized sample was the base level. When these values were compared the other case depth results obtained from hardness and carbon depth profiles, they were also coherent with each other.

5.3. Residual Stress State Analysis

5.3.1. XRD Results

To ensure repeatability and accuracy of results, five measurements were taken from each back and front surface of samples with three directions which are called phi angles; 0°, 45° and 90°. The mean of the five measurements were taken as the overall residual stress value at the surface of the samples. Residual stresses were calculated by X-Tronic software by using d vs. $\sin^2 \psi$ method. During calculation, biaxial stress state was assumed.

Figure 5. 13 shows the least square lines fitted to the data obtained from the XRD pattern. It exhibits a regular d vs. $\sin^2 \psi$ behavior, which suggests the use of the equation stated below. Residual stresses, which exist in the direction of 45° and 90°, could also be controlled to ensure that they show also regular fit behavior.

$$\frac{d_{\phi} - d_0}{d_0} = \frac{1+\nu}{E} \sigma_{\theta} \sin^2 \phi - \frac{\nu}{E} (\sigma_{11} - \sigma_{22}) \quad \text{Eq. 16}$$

The calculated residual stress distribution for three different phi angles is tabulated on Table 5. 2. This table also shows the measurement error originated from the XRD device. The stresses were calculated by using elliptical method and it was assumed that out of plane stress (σ_{33}) should be equal to zero. In order to assume that condition, the calculated compressive residual stresses in the martensite phase should be balanced with tensile residual stresses in the austenite phase.

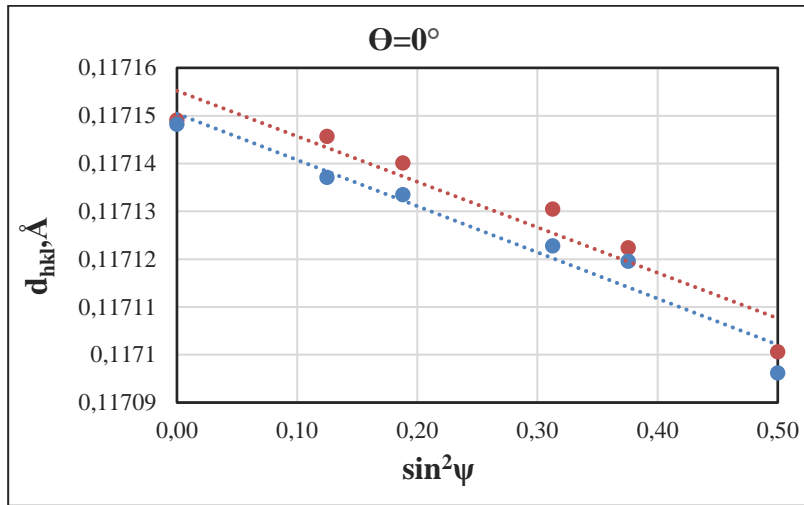


Figure 5. 13 d vs. $\sin^2\psi$ curve fitted to the diffraction data of $\Phi=0^\circ$ (900°C/5hrs carburized sample)

Table 5. 2 XRD residual stress measurement results three phi angles; 0° , 45° and 90°

Specimen Code	$\phi=0^\circ$		$\phi=45^\circ$		$\phi=90^\circ$	
	MPa	Error	MPa	Error	MPa	Error
Normalized	-247	$\pm 16,1$	-240	$\pm 12,6$	-262	$\pm 8,24$
C05T0	-473	$\pm 11,3$	-480	$\pm 12,0$	-472	$\pm 6,78$
C05T180	-385	$\pm 13,7$	-360	$\pm 12,3$	-377	$\pm 7,51$
C05T240	-395	$\pm 12,1$	-383	$\pm 12,6$	-398	$\pm 11,4$
C05T600	-347	$\pm 8,9$	-377	$\pm 6,1$	-341	$\pm 9,3$
C09T0	-518	$\pm 7,6$	-531	$\pm 8,4$	-534	$\pm 9,4$
C09T180	-424	$\pm 6,5$	-426	$\pm 10,3$	-424	$\pm 8,9$
C09T240	-552	$\pm 13,9$	-543	$\pm 16,0$	-502	$\pm 9,4$
C09T600	-346	$\pm 8,1$	-368	$\pm 8,6$	-340	$\pm 12,4$
C12T0	-566	$\pm 11,3$	-564	$\pm 11,4$	-565	$\pm 7,3$
C12T180	-517	$\pm 10,8$	-539	$\pm 14,7$	-598	$\pm 9,3$
C12T240	-488	$\pm 7,9$	-489	$\pm 8,1$	-470	$\pm 10,2$
C12T600	-372	$\pm 6,3$	-381	$\pm 7,9$	-403	$\pm 12,4$

Changing phi angles creates no significant difference on the residual stress values, however, the values show increasing tendency with increasing carburizing time for the untempered condition. The highest compressive residual stress value was observed in the case of 12-hr carburized specimens due to the increase in the martensite content. Tempering at 180°C has no considerable effect on the stress state. Nevertheless, further increase in tempering temperature causes a remarkable amount of stress relieving. When 5-hr carburized sample is considered, if tempering temperature alters from 180°C to 600°C, surface stress values decrease from -470 MPa to -350MPa. At 600°C, residual stresses are relieved remarkably and microstructure changes, i.e., cementite precipitates in ferrite coarsens and spheroidizes.

The phase fraction analysis by JmatPro software showed that the amount of retained austenite is nearly 5, 10 and 15 weight percent for 5, 9 and 12-hr carburized specimens, respectively. They were shown in Appendix A in Figure A. 1, Figure A. 2 and Figure A. 3. In contrast to 5 and 9-hr carburized samples, 12 hours-carburized samples contain significant amount of retained austenite. If the amount of retained austenite exceeds 15 wt %, a remarkable decrease is observed in case hardness. However, for applications involving contact loading, the optimum service life is found when the retained austenite content is in the range from 30 to 40% [3]. To determine residual stress in the retained austenite, special software in XRD measurement device should be used.

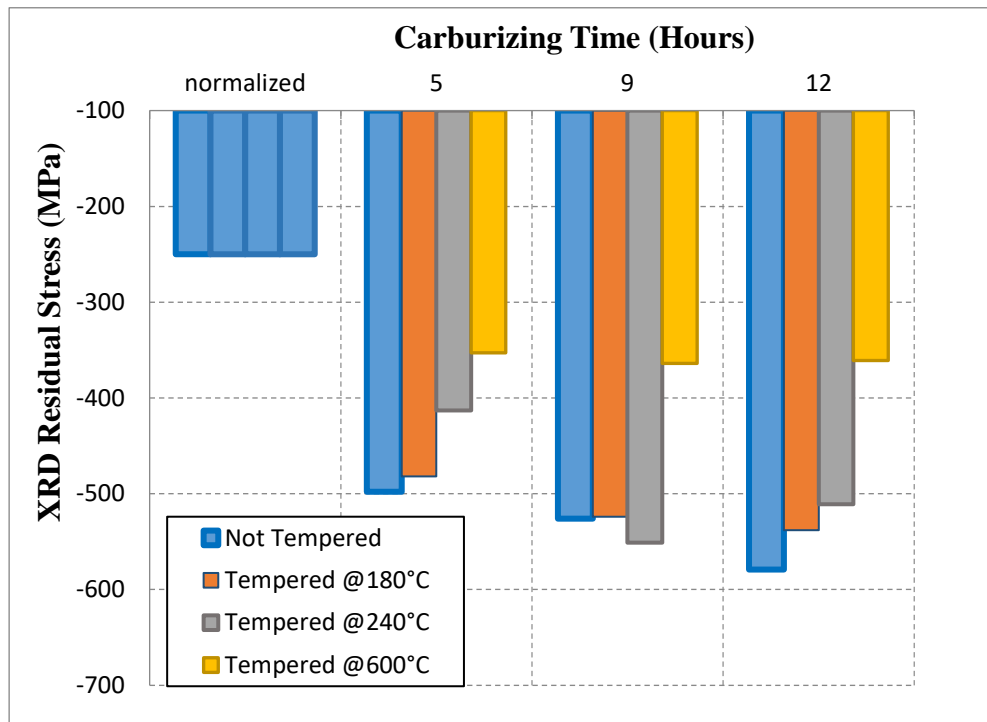


Figure 5. 14 Effects of carburizing time and tempering temperature on the surface residual stress of the ca SAE/AISI 8620 samples

5.3.2. MBN Measurement Results

Two channels exist in the Barkhausen device; Rollscan and μ Scan. They have different filtering range and excitation frequency to magnetize the specimen.

5.3.2.1. Rollscan Results

Measurements using by Rollscan channel are more appropriate for industrial practice in order to evaluate rapidly the homogeneity of surface quality and several properties such as hardness, microstructure and stress state. The magnetizing frequency of the Rollscan software is 125 Hz. It outputs the magnetic noise activity as MBN emission parameter (MP) value.

Without Pre-Calibration

Rollscan measurements give combined information about total influencing parameters such as grain size, dislocation density, grain and phase orientation and residual stress state. Although obtained value from this sensor is very complicated, general comparison among different heat-treated specimens could be made without applying any calibration method. The first inference could be that higher MBN activity is resulted in mechanically soft materials due to the lower dislocation density. Hence, high MBN emission values observed in the normalized specimen indicate that the microstructure has a soft magnetic property, whereas a low magnetic emission level corresponds mechanically and magnetically hard material. After optimization of magnetization and measurement parameters by magnetic saturation calibration method, raw data were recorded as MBN emission parameters given in Table 5. 3. The highest MBN emission level was observed in the normalized specimens since they have minimum hardness among all samples. Moreover, dislocation density and some impurity atoms like excess carbon act as pinning sites to the movement of domain walls. Normalizing process results in a uniform microstructure, thus the MBN measurements taken from nine different positions did not show significant deviations. However, the other specimens showed some differences with respect to the measurement positions.

The effect of carburizing time on MBN activity is shown in Figure 5. 15. The highest level of MBN emission (about 200 MP) was observed in the normalized sample. When the 900°C-carburizing was applied for 5 hours, the MP value reduced to 60. As increasing carburizing time up to 9 hours, the MP value further reduced. However, further increase in the carburizing time up to 12 hours did not show the same tendency. The reason is that 12-hr carburized specimens did not made up of completely martensitic microstructure. As seen in CCT diagram of 12-hr carburized specimens, they included some amount of retained austenite, which is softer than martensite

phases and causes relatively low dislocation density. Because of this, MBN emission parameters of 12-hr carburized specimens are higher than that of 9-hr carburized specimens.

The influence of tempering temperature on domain wall activity was considered for three carburizing conditions and the MBN emission are given in Figure 5. 16, Figure 5. 17 and Figure 5. 18 for 5-hr, 9-hr and 12-hr carburizing, respectively. Changes in the microstructure due to tempering make easier the domain wall movement, and hence higher MBN emission is expected. In all carburizing conditions, tempering at 180°C has no significant effect on the MBN emission. However, further increase in the tempering temperature causes considerable changes. For 5-hr carburized samples, tempering at 240°C leads to increase MBN parameters for nearly 30 MP. At 600°C, this tendency was not observed although this temperature level causes high amount of stress relaxation and dislocation density reduction. Similar to 5 hour carburized specimens, the other carburized specimens did not show the linear increasing behavior neither. This should be caused by the complicated mechanisms of domain wall movement since their movement depends three considerable factors; residual stress state, microstructures and dislocation density. Moreover, tempering processes change all these factors with a different fraction. When it is desired to observe their effects individually, a proper and controllable optimization and calibration method are required.

Table 5.3 Raw MBN emission values for different measurement directions at the surface with standard deviation

Specimen Code	$\phi=0^\circ$		$\phi=45^\circ$		$\phi=90^\circ$	
	MBN level	Std. Deviation	MBN level	Std. Deviation	MBN level	Std. Deviation
Normalized	200,3	±2,9	200,0	±5,0	201,0	±3,7
C05T0	85,0	±10,2	84,0	±14,5	86,7	±14,1
C05T180	56,7	±18,5	57,0	±14,0	61,7	±19,4
C05T240	106,7	±14,1	102,0	±14,7	100,0	±17,0
C05T600	82,8	±12,4	80,0	±13,9	82,8	±14,1
C09T0	55	±18,2	50,0	±19,3	50,0	±18,2
C09T180	61,7	±16,3	60,0	±10,2	58,3	±14,7
C09T240	62,5	±17,5	65,0	±18,7	67,5	±12,5
C09T600	31,7	±14,1	28,0	±16,7	25,0	±16,2
C12T0	90	±12,4	102	±15,3	100	±12,4
C12T180	120,3	±27,2	123,0	±23,2	125,3	±30,6
C12T240	45,0	±12,4	40,0	±16,5	42	±17,1
C12T600	61,7	±14,6	60,0	±14,3	60,0	±16,2

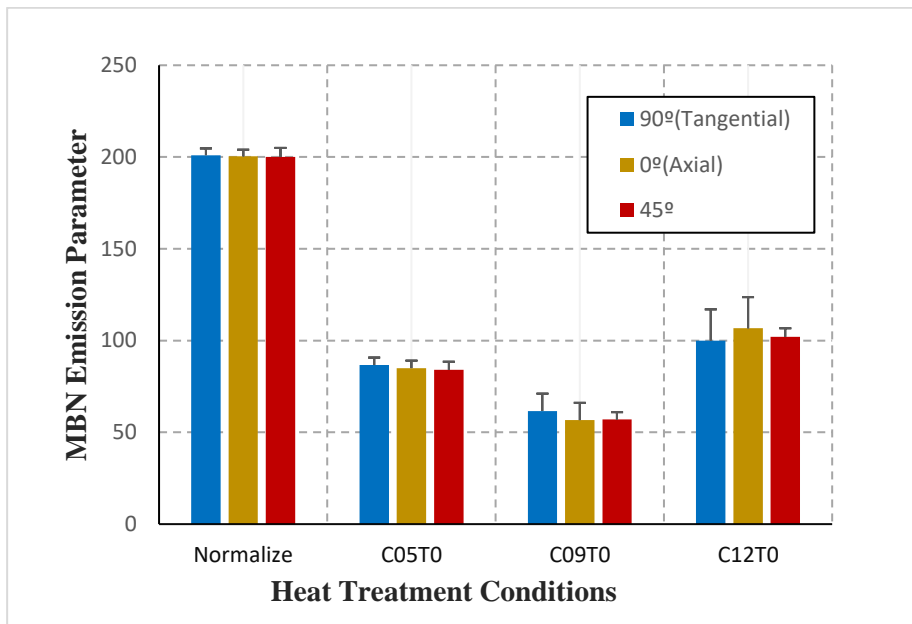


Figure 5. 15 Effect of carburizing time at 900°C on the average MBN activity for AISI/SAE 8620 steel (different measurement directions at the surface)

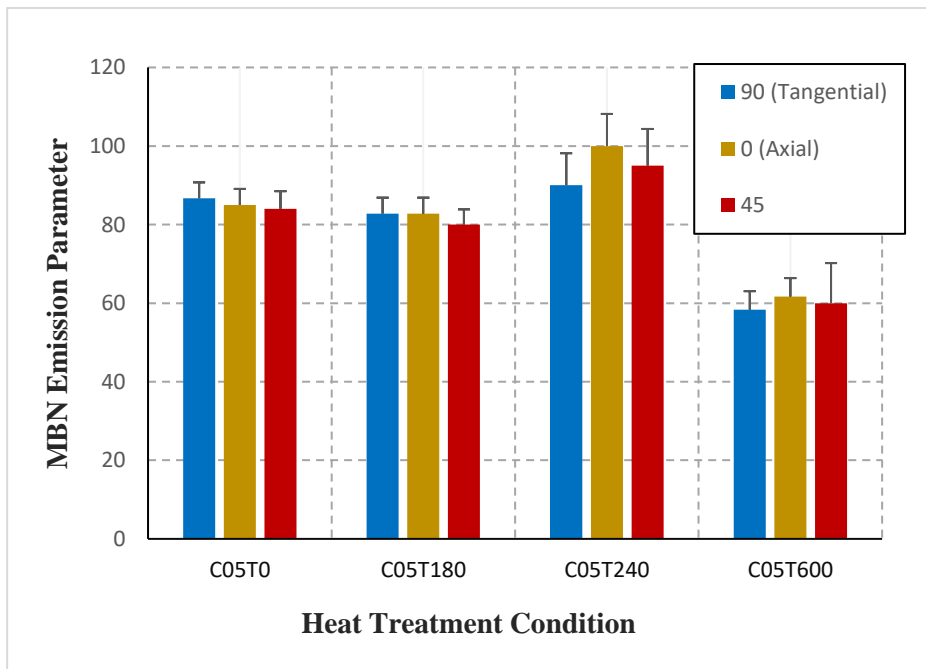


Figure 5. 16 Effect of tempering temperature on the Average MBN activity for the carburized AISI/SAE 8620 steel (900°C/5hrs)

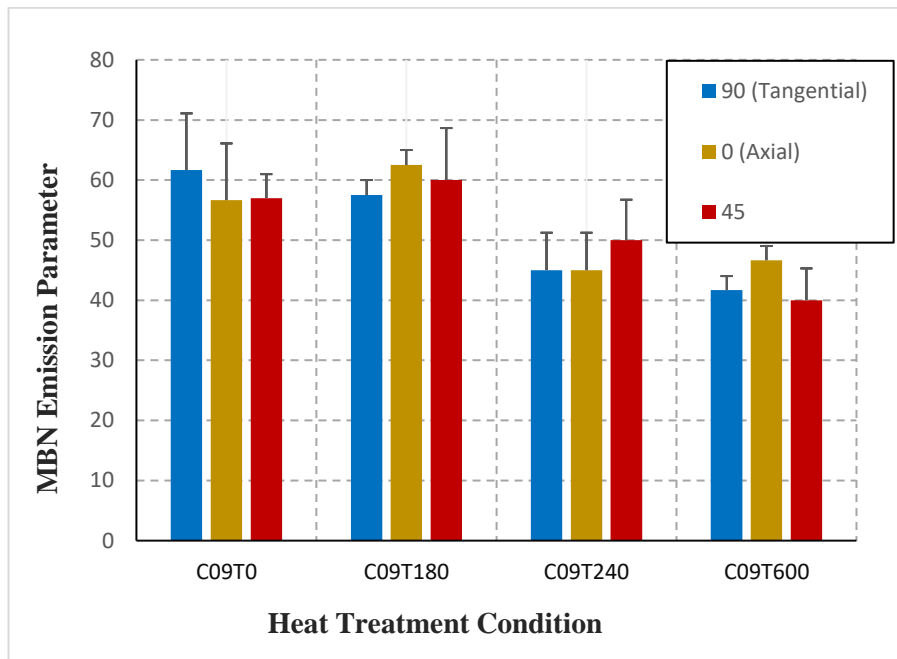


Figure 5. 17 Effect of tempering temperature on the Average MBN activity for the carburized AISI/SAE 8620 steel (900°C/9hrs)

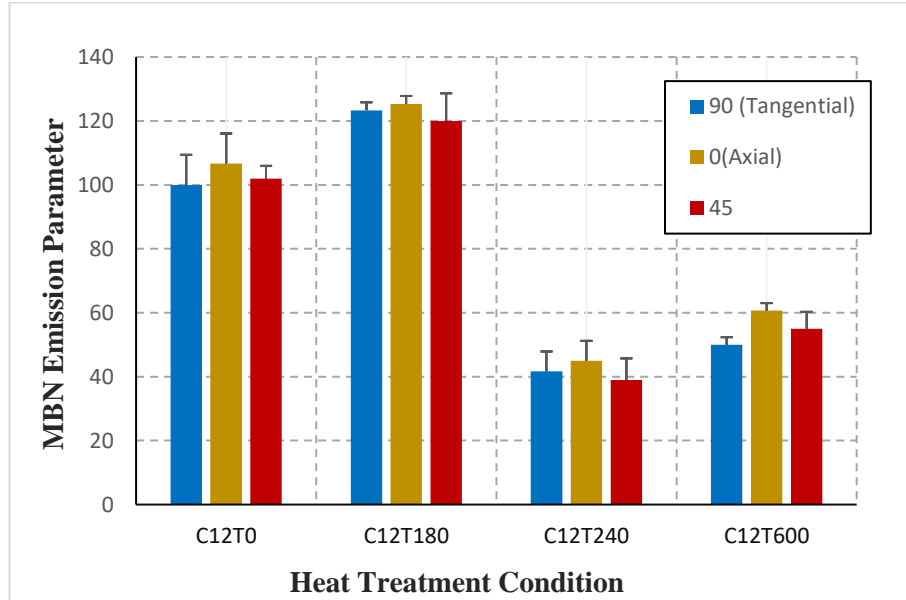


Figure 5. 18 Effect of tempering temperature on the Average MBN activity for the carburized AISI/SAE 8620 steel (900°C/12hrs)

With Pre-Calibration

Although qualitative comparison without pre-calibration is possible, understanding of the effect of individual parameters quantitatively such as residual stress state requires some special calibration methods. In this study, tension and compression tests were applied by measuring both strain and MBN emission at the surface simultaneously.

The previous study in our research group, which was examined by the *Hızlı et al.* [102], is related to the monitoring of residual stress state in the carburized 19CrNi5H steel specimens. In that study, instead of applying the mechanical calibration, optimization of magnetic parameters and then correlation between RMS values obtained from MBN measurement and the residual stress values obtained from the XRD measurements were carried out in order to predict the accurate residual stress state. It was stated that when the MBN parameter optimization is carried out correctly, good correlation between MBN RMS values and XRD residual stress measurements should be obtained. The Pearson's correlation factors were obtained between the range of 0.90 and 0.92. On the other hand, it was stated that there was still a considerable amount error in the correlation. It was explained by the differences in the information depth and volume between these two techniques. Moreover, the uncertainty could be deduced that MBN emission signal is dependent on the other factors in the steel specimens. Hence, it was concluded that it is necessary to find more controlled way to calibrate the MBN signals and then to predict residual stress accurately. In addition to two techniques, in that study, ESPI assisted hole-drilling measurement software was also used to measure the accurate residual stress values semi-destructively. The results obtained from those techniques showed that a good correlation between those techniques were observed. It could be inferred from the results that the quantitative residual stress values could be directly obtained from the XRD and ESPI assisted hole-

drilling software, whereas residual stress state could be predicted by means of RMS values from MBN system.

To obtain closer residual stress values obtained from MBN and XRD measurements, the special way to calibrate the MBN signals was carried out. First, Calibration specimens were used to make a connection between raw MBN signals and residual stress values. For this purpose, thirteen calibration specimens ($l_0=148$ mm, $d_0=13$ mm) were prepared for each heat treatment condition. Then, they were hold at 600°C for 1 hour in order to relieve residual stresses. Due to the composite microstructure of the carburized specimens, the surfaces and cores were expected to show different behavior under applied load. Since MBN measurements were taken from near surface region, near surface elongation and strains are relevant for this calibration. Therefore, a strain gauge was attached to the surface while MBN probe was on the other side of the surface. Instantaneous surface strain values were converted to the surface stress values by using Hooke's law equation. Moreover, corresponding MBN parameter values were read from the device. Then, surface stress values were plotted with respect to corresponding MBN parameter values (Figure.5.19- 5.22). Using these calibration curves, raw MBN emission parameters measured on the rectangular heat-treated specimens were transformed to the residual stress values (Table 5. 4).

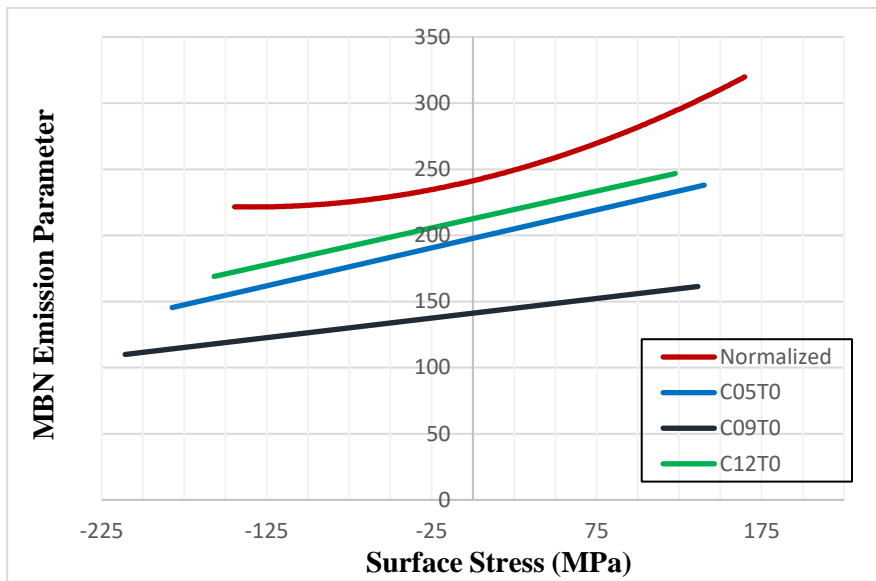


Figure 5. 19 MBN vs stress calibration curves of carburized AISI/SAE 8620 steel specimen (900°C/5, 9, 12hrs)

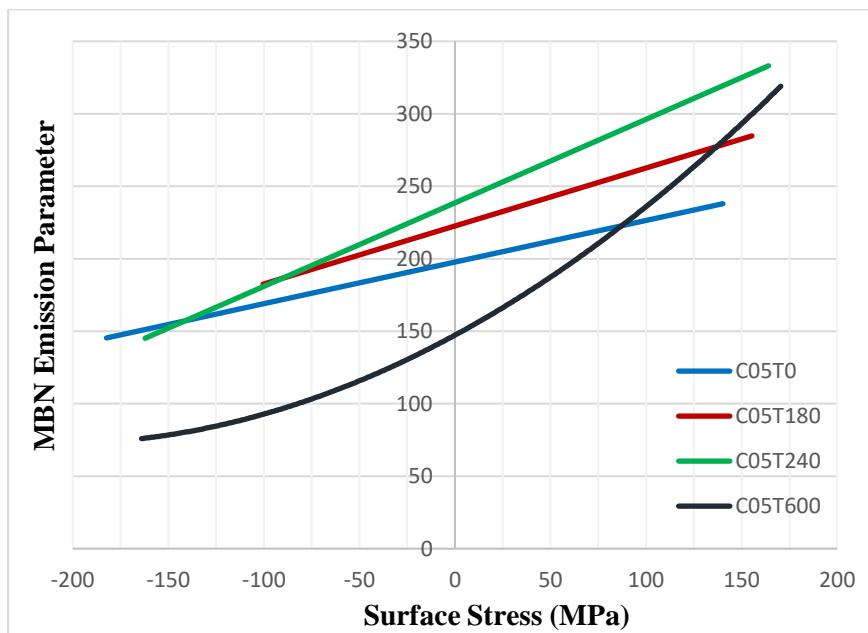


Figure 5. 20 MBN vs stress calibration curves of carburized and tempered AISI/SAE 8620 steel specimens (900°C/5hr)

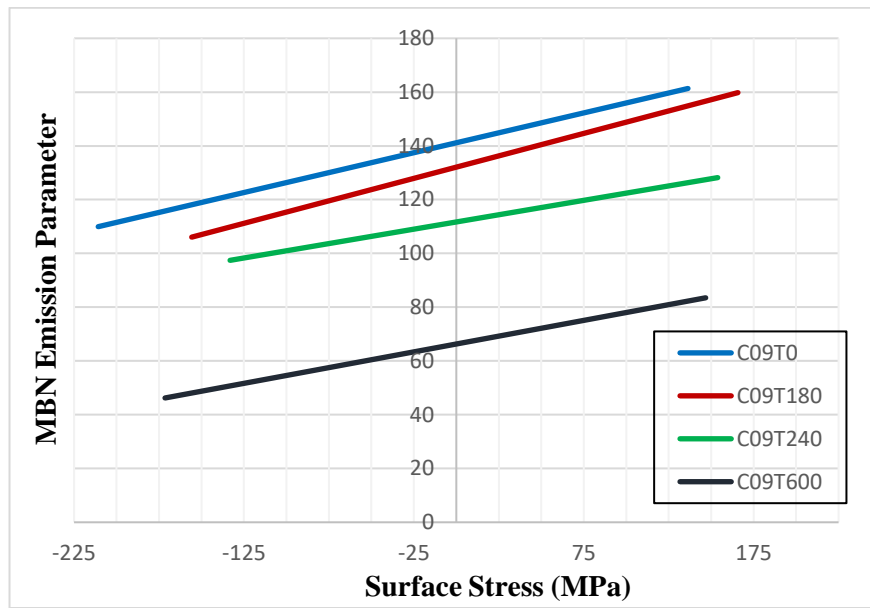


Figure 5. 21 MBN vs stress calibration curves of carburized and tempered AISI/SAE 8620 steel specimen (900°C/ 9 hrs)

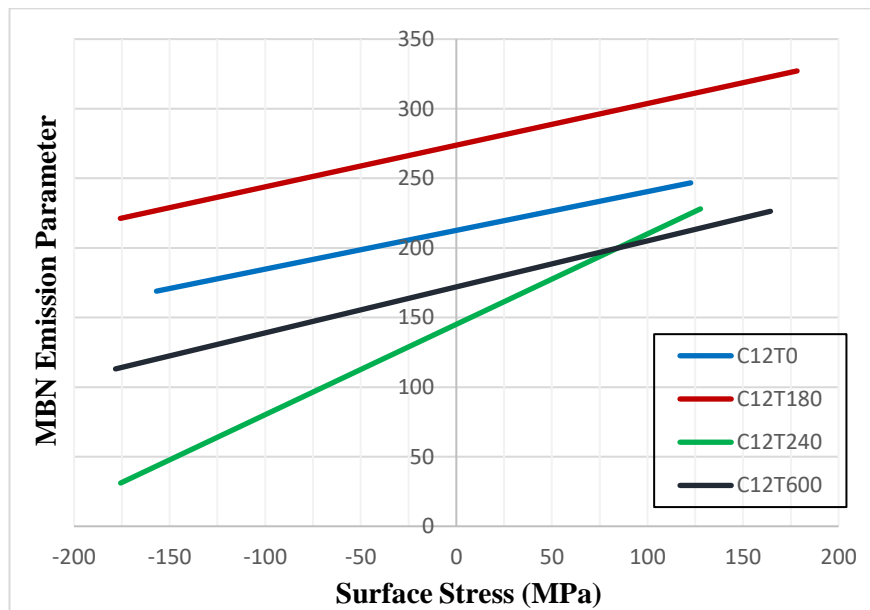


Figure 5. 22 MBN vs stress calibration curves of carburized and tempered AISI/SAE 8620 steel specimen (900°C/12hrs)

Table 5. 4 Residual stress values of specimens converted from MBN emission parameter by using calibration curves

Specimen Code	$\phi=0^\circ$		$\phi=45^\circ$		$\phi=90^\circ$	
	MBN RS (MPa)	Std. Deviation	MBN RS (MPa)	Std. Deviation	MBN RS (MPa)	Std. Deviation
Normalized	-313	± 5	-310	± 10	-314	± 7
C05T0	-404	± 45	-400	± 45	-395	± 45
C05T180	-410	± 40	-415	± 45	-400	± 45
C05T240	-220	± 30	-210	± 30	-215	± 35
C05T600	-266	± 12	-250	± 14	-254	± 14
C09T0	-575	± 80	-600	± 80	-600	± 80
C09T180	-425	± 50	-420	± 35	-430	± 45
C09T240	-460	± 80	-450	± 85	-465	± 70
C09T600	-236	± 55	-240	± 60	-250	± 55
C12T0	-610	± 60	-620	± 65	-613	± 60
C12T180	-500	± 80	-495	± 70	-490	± 85
C12T240	-230	± 20	-240	± 30	-235	± 35
C12T600	-290	± 45	-294	± 42	-294	± 48

5.3.2.1.1. MBN Residual Stress vs XRD Residual Stress

Although MBN and XRD methods gave the same tendency, the stress values determined by the MBN method were not exactly the same with those obtained by the XRD measurements. The highest difference, i.e. 80 MPa, was observed in the tempered specimens, (Figure 5. 23).

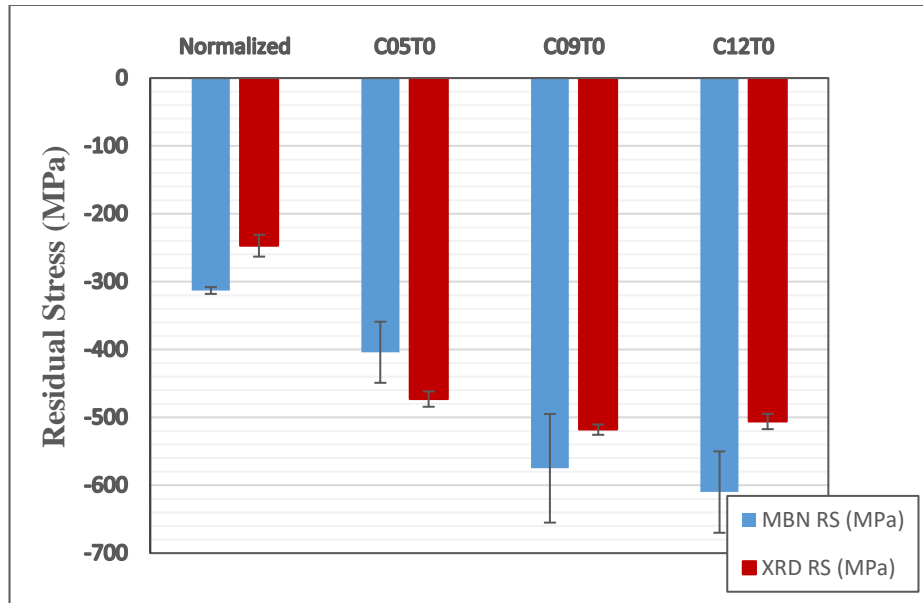


Figure 5. 23 Comparison of the residual stress values obtained by MBN and XRD methods.

This difference is most probably caused that regions where MBN signals were gathered by MBN probe might have non-homogeneous and different phases. Moreover, the information depth of these two techniques also differ from each other. XRD method give the stress values that were obtained from 10 μm depth from surface whereas MBN emission parameters were gathered from nearly 150 μm below the surface. Moreover, there are additional factors that affects the domain wall movements during MBN measurements.

5.3.2.2. μ Scan Results

5.3.2.2.1. RMS Results of Signal Envelope

MBN measurements were reported at the selected points by μ Scan mode. μ Scan detector gives the some special and more characteristic knowledge about magnetic behavior of samples. One of the most significant information is about root mean square (RMS) values obtained from noise signal envelope. RMS signal envelopes that correspond to the RMS voltage as a function of magnetic field strength were given in Figure 5. 24 and Figure 5. 25. Although signals were obtained with both negative and positive direction of magnetization, only $RMS_{positive}$ signals are plotted due to the symmetry of signals with respect to magnetization direction.

RMS values of noise signals are strongly related to domain wall motion. When magnetic domains are moved easily, noise like signals show the higher amplitude of the envelope that means they give higher RMS values. Compressive residual stresses obstruct the movement of the 90° domain wall and it causes to reduce MBN activity. Because of this phenomena, RMS values of signal decreases with increasing compressive residual stress condition. As shown in the Figure 5. 24, the highest RMS value was observed in normalized specimens whereas twelve hour carburized specimens showed the lower MBN activity under the same excitation magnetization frequency. It is expected results from the microstructures analysis and hardness measurement values which is the another important influencing factor of MBN activity. Hardness values of these specimens were increased by enhancing dislocation density caused by lattice distortion. Not only largest compressive residual stress but also highest dislocation density caused the lowest RMS value in the as-quenched form of the 12-hours carburized specimens.

Moreover, the other information deduced from this signal envelope is about microstructure. When hard magnetic phases exist in the microstructure such as martensite, domain walls would start to movement at the higher magnetization value; i.e.; these phases required much more magnetic field strength to orient their domains. Hence, amount of martensite phases in the case region increases, the signal peaks shift to the higher magnetic field strength values. To observe the effects of microstructures, peak positions should be compared in Figure 5. 24. Higher amount of martensite is expected in the specimens, which were exposed to carburizing atmosphere for longer time. Hence, 12 hour carburized specimen may have higher amount martensite. However, microstructural analysis showed that after some critical time carburizing time does not have significant effect in increasing martensite amount since specimens have already reach sufficient carbon amount to obtain 100% martensite in microstructure at the critical carbon level. Both nine and twelve hours carburized specimens have nearly the same amount of martensite. Hence, the differences between the shifts of their peaks are not considerable. However, when normalized and carburized specimens are compared, microstructural effects can be seen clearly. In the normalized specimens, the peak of the signal envelope coincides with nearly the initial point that is zero relative magnetic field strength since hard magnetic phases does not exist and domains start to orient themselves easily at the low magnetic field strength level.

Tempering process has considerable effect on the MBN RMS values. The crystal structure of martensite losses its tetragonality and dislocation density reduces during tempering which causes localized relaxation of stresses. Figure 5. 25 shows that tempering causes reduction in RMS values for all carburizing conditions.

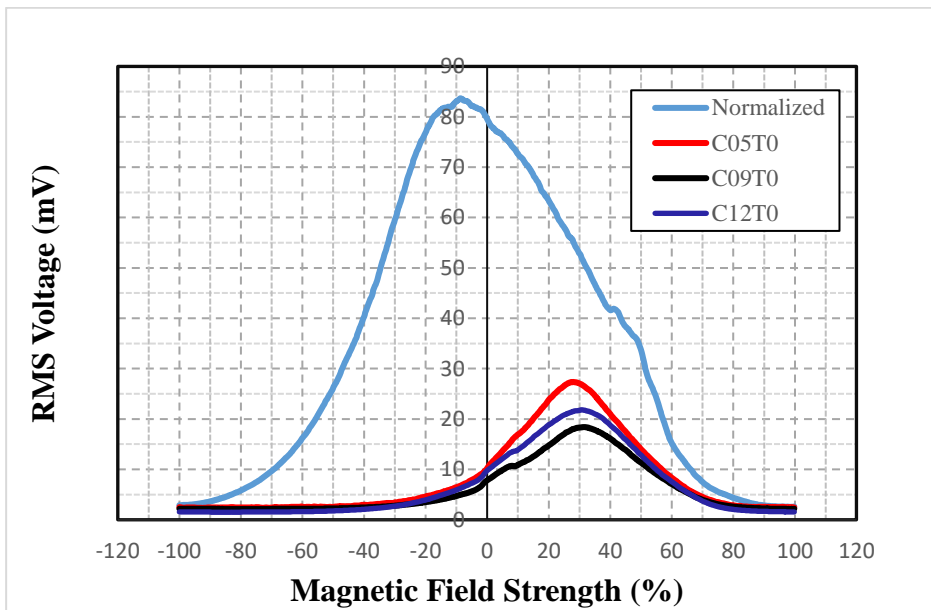


Figure 5. 24 RMS signal envelope of normalized and carburized specimens

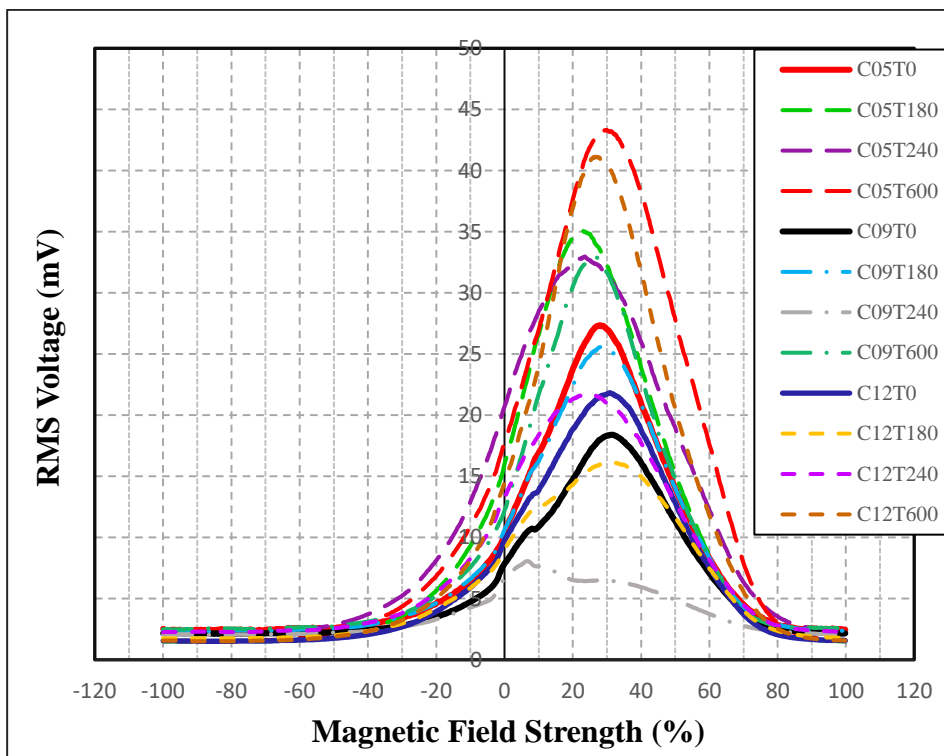


Figure 5. 25 RMS signal envelope of the carburized and tempered specimens

5.3.2.2.2. Hysteresis Curves

Figure 5. 26 shows that mechanically soft normalized specimen has the lowest coercivity and the highest relative permeability in comparison to carburized specimens. As the carburizing time increases, coercivity values do not alter whereas relative permeability and hysteresis loss values change. It is expected situation since coercivity is not sensitive to small variations in the stress values; however, it is strongly dependent on the microstructure and hardness.

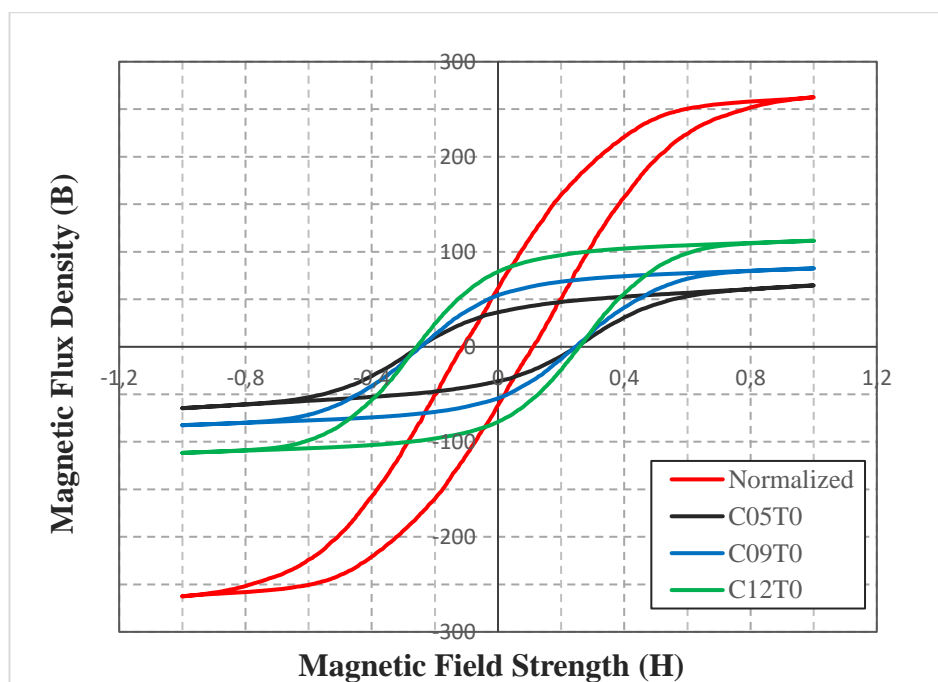


Figure 5. 26 Representative hysteresis curves of the specimens

When the magnetic field applied the alternative directions, a representative magnetic hysteresis loop is obtained. This irreversible process is dependent to the dynamic behavior of domains. Dynamic behavior of domains is considered as the nucleation, annihilation and growth of domains. Moreover, dislocations, grain sizes and their

boundaries and precipitates influence this behavior. Hence, the number of domain walls instantaneously moved in the free path decide the MBN peak height. Saquet et al [77] indicated the theory about the change of the local magnetic moment (δm) causing MBN emission was given by:

$$\delta \vec{m} = \beta * (S * \delta \vec{l}) \quad \text{Eq. 18}$$

where β is a constant related to the atomic magnetic moment and type of domain wall, S is the surface of the moving domain wall and δl is the wall displacement between pinning obstacles. MBN activity is mainly created by the motion of 180° domain walls. So the moment is influenced mainly by wall displacement related to microstructure and pinning sites. Small martensite needles in the as-quenched specimens decide the average size of the domains that limit the domain wall displacements. This condition lowers Barkhausen noise emission.

Tempering has also influence the morphology of the martensite phases by changing the S value and causes an increase in the MBN activity. When tempering temperature increases, the microstructure coarsens, which makes larger domain wall displacements possible. In addition, the surface of moving domain walls (S) will increase, as domains get larger due the coarsening of microstructure [101]. Therefore, the MBN activity is expected to improve as tempering temperature increases. Figures 5. 27-5. 29 show the representative hysteresis curves of 5, 9 and 12-hr carburized specimens, respectively. Coercivity changes in small quantities since hardness values and microstructures of samples had been changed in addition to stress state. The most severe changes were observed in the area of hysteresis loop that are mainly influenced by the domain wall

movement and MBN activities. The higher the tempering temperature is, the lower the hysteresis loss is due to the reduction of pinning sites and compressive residual stress.

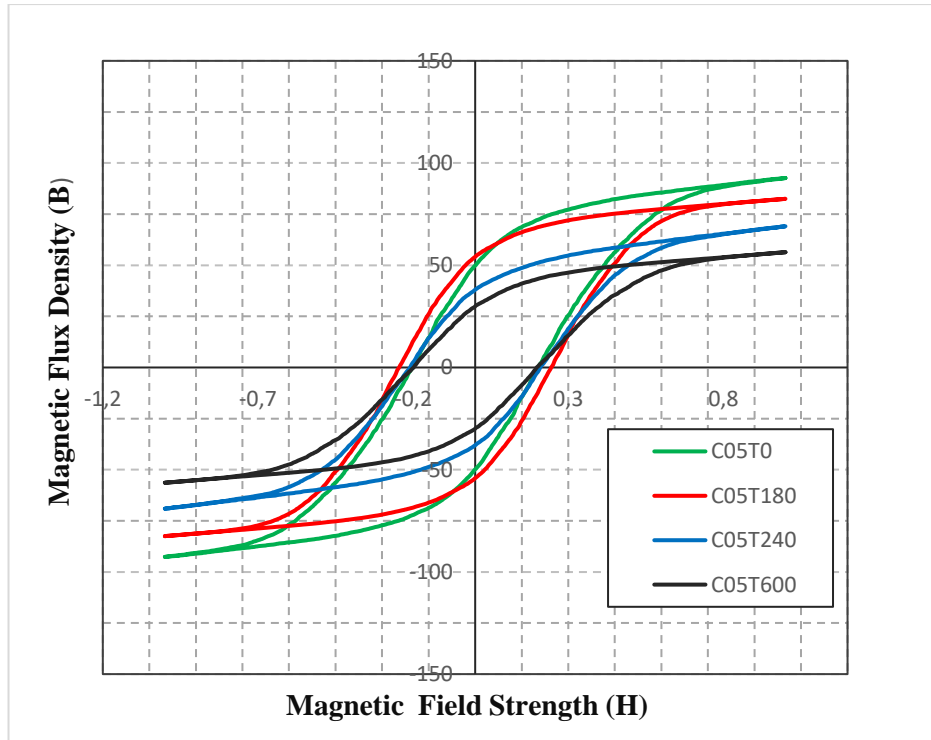


Figure 5. 27 Representative hysteresis curves of the carburized (900°C/5hr) and tempered specimens

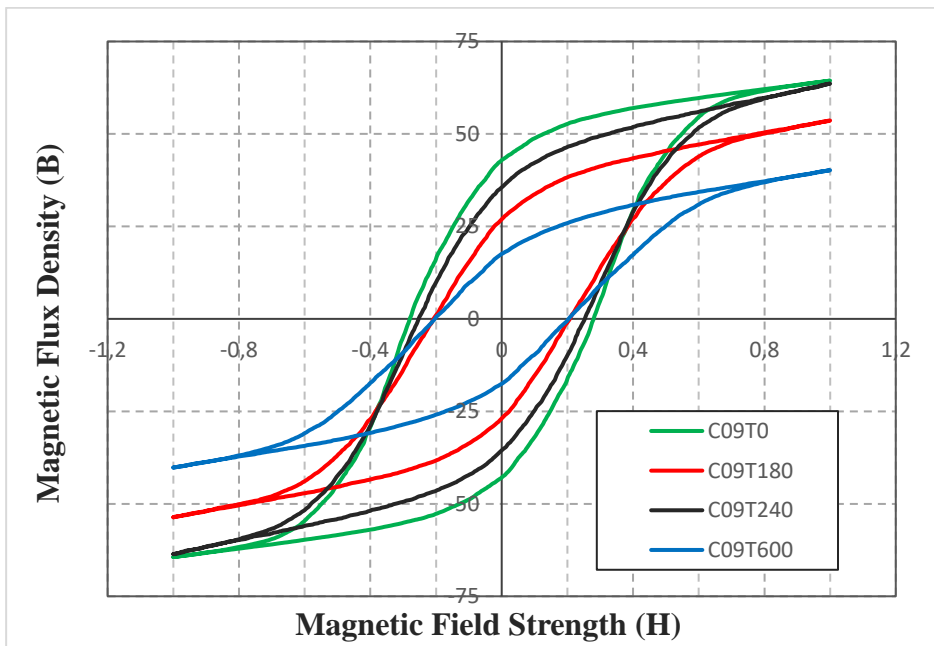


Figure 5.28 Representative hysteresis curves of the carburized (900°C/9hr) and tempered specimens

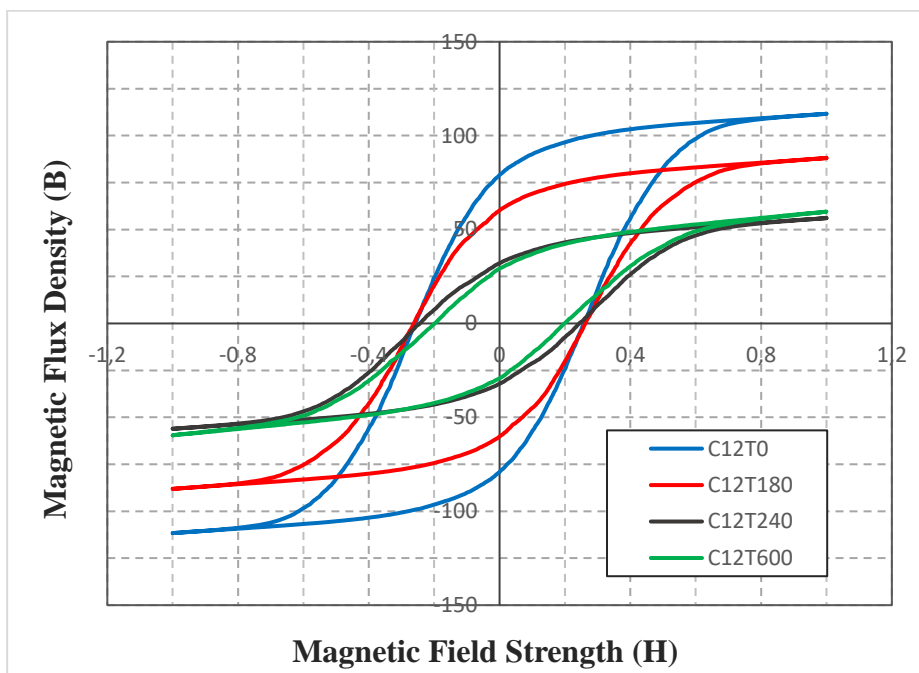


Figure 5.29 Representative hysteresis curves of the carburized (900°C/12hr) and tempered specimens

Table 5. 5 Remanence, coercivity and differential permeability values of the carburized (900°C) and tempered AISI/SAE 8620 steel specimens

Sample Code	Remanence (B_r) Tesla	Coercivity (H_c) kA/m	Relative Permeability
Normalized	50,4	0,046	633
C05T0	45,2	0,22	281
C05T180	50,2	0,21	255
C05T240	42,1	0,22	224
C05T600	25,3	0,22	215
C09T0	48,7	0,28	165
C09T180	25,2	0,26	123
C09T240	30	0,20	150
C09T600	20,73	0,21	125
C12T0	78,67	0,26	302
C12T180	65	0,26	269
C12T240	32	0,24	133
C12T600	28	0,19	147

CHAPTER 6

CONCLUSION

Different residual stress states in the AISI/SAE 8620 steel were obtained by following various routes of carburizing and tempering. First, the normalizing process was applied to all specimens. Then, three sample series were prepared by carburizing at 900°C for 5 hours, 9 hours and 12 hours. Next, sample groups were exposed to four different conditions such that not tempered, and tempered at 180°C, 240°C and 600°C. All samples were examined in respect to microstructure, hardness and percent carbon content by the conventional optical metallography and Scanning Electron Microscopy, hardness testing and the optical emission spectrometry. Two measurement techniques were used in order to characterize the residual stress state, namely Magnetic Barkhausen Noise (MBN) and X-Ray Diffraction (XRD). To improve the accuracy of the measurements, specific calibration procedures were applied.

The following conclusions can be drawn from this particular study;

- Martensite phase forms in the case hardened region after carburizing and quenching. Carbon content decreases from 0.9 wt% to 0.2 wt% C as going from case to core with a corresponding decrease in hardness. Tempering changes the microstructure, especially the amount of retained austenite in the case hardened region. 9-hr and 12-hr carburized specimens have nearly 10 wt% and 15 wt%

retained austenite, respectively. Due to tempering, it transforms to the other phases.

- XRD measurements showed that compressive residual stresses exist at the surfaces of all specimens. The magnitude of compressive residual stress increases with increasing carburizing time at 900°C. Tempering reduces the magnitude of the residual stress, and the degree of reduction increases with increasing tempering temperature.
- Magnetic Barkhausen Noise measurements show the similar tendency with the results of the XRD method. Although identical qualitative results were obtained from both methods, quantitative differences exist within the ± 80 MPa range. These variations are probably due to assumptions, different information depths of the techniques, and existence of several influential parameters in MBN measurement such as combined effects of residual stress and microstructure.
- The relative MBN-RMS value is compatible with the residual stress value measured by XRD. It decreases with increasing carburizing time at 900°C; and decreases with increasing tempering temperature. As martensite content increases, the MBN peak position shift to the higher magnetic field strengths. It is inferred from the representative hysteresis curves of the specimens that mechanically hard samples have higher coercivity. However, it should be considered that both microstructural features and stress state effect the coercivity and the area of the hysteresis loop. When compressive residual stress increases coercivity does not change significantly whereas relative permeability and hysteresis loss of curves are strongly influenced. The hysteresis loss decreases with increasing tempering temperature due to the

reduction of compressive residual stress and also dislocations acting as pinning sites for domain movement.

- From the industrial point of view, the MBN technique is a strong candidate for nondestructive qualitative monitoring of residual stress variations in the carburized and tempered steels. Its application is suitable for automation and much faster than the XRD technique while both techniques give similar tendency for residual stress variations. With an appropriate pre-calibration procedure that considers the effects of microstructure, MBN technique may also give reliable quantitative results.

6.1. Recommendation for Further Studies

Although a progress has been achieved in measurement of residual stress by using MBN technique, there are still some challenges that make the field open to the researchers from different disciplines. These can be related to mechanical metallurgy for the stress state calculations, micromagnetics to understand deeply the local magnetic behavior of specimens, material science for the advanced phase transformation and kinetics, physics and electronics to understand the mechanism of MBN device and probes.

Calibration of MBN system is very critical. In order to eliminate the effects of shape factor on calculation of residual stress values, the calibration samples should have the same shape and dimensions with those on which MBN measurements were taken. Specimens should be thicker in order to distinguish case to the core region clearly. In addition, finite element simulation tools should be used for better analyses of the results.

Although the MBN results indicate the similar tendency with XRD method, closer values can be obtained by reducing assumptions in stress calculations. In XRD measurement, out of plane stress condition was assumed and the other two principal stresses were considered. On the other hand, examining of d vs. $\sin^2\psi$ graph used for the stress calculation indicated ψ -splitting in the material, which means that there exist strains induced by out-of-plane stress. By determining the interplanar spacing and after stress values as exact as possible, three stress tensor could be determined by using triaxial stress state. When considering MBN measurement and calibration in respect to calculation of stress tensor, uniaxial stresses were applied and only one principal stresses was considered in the stress calculation. To obtain more realistic stress values, biaxial stresses should be applied and measured.

Since MBN signal is affected by microstructure, hardness and residual stress state, the variation of MBN activity should be investigated on the specimen series prepared by changing only one parameter.

REFERENCES

1. Nitschke-Pagel T., Dilger K, Eslami-Chalandar H. (2011). Determination of Residual Stresses in Welded Structural Steels with Help of Micromagnetic Measurements. *Materials Science Forum*. Vol.681, 194–201.
2. Totten G., Sverdlin A.V., Ness A.R., (2006) *Steel Heat Treatments, Fundamental Concepts in Steel Heat Treatment*, Taylor&Francis Group.
3. Krauss G. (1989). *Steel Heat Treatment and Processing Principles in ASM Handbook*, Vol.4, Heat Treating, ASM International, Ohio.
4. Hosford W.F, (2005), *Physical Metallurgy*. Taylor & Francis Press, Boca Raton.
5. Honeycombe, R., Bhadeshia, H.K.D.H., (1995). *Steels Microstructure and Properties*. London.
6. Grosch J. (1993). Quenching and Carburizing, Proceedings of the Third International Seminar of the International Federation for Heat Treatment and Surface Engineering, *Fundamentals of Carburising and Toughness of Carburised Components* Institut für Werkstofftechnik, Technische Universität, Berlin, Germany
7. Sharma R. (1996). *Principles of Heat Treatment of Steels*, New Delhi: New Age International, 211-216.
8. Stickels A. and Mack C.M., (1989). *Carburizing: Processing and Performance*, ed. G. Krauss, ASM International, Materials Park, OH.
9. Boyer H.E., (1987), *Case Hardening of Steel*, ASM International, Materials Park, OH.
10. Thelning K. (1984). *Steel and Its Heat Treatment*. Butterworths, London. 17-90.
11. Cavaliere P. Zavarise G., Perillo M. (2009). Modeling of the Carburizing and Nitriding Processes, *Computational Materials Science*, Vol. 46 ,26–35

12. Dossett J. (2014). *Steel Heat Treating Fundamentals and Processes*. Materials Park, OH: ASM International Vol.4A. 528-580.
13. Mc Adams W.H., (1954), *Heat Transmission*, New York, McGraw-Hill, 43-50.
14. Grabke H. J. (1990). Härterei-Technische Mitteilungen, Vol.45.
15. Edenhofer B. (2000) Case-hardening: Process with New Evolutions and Perspectives, Proceedings of the 5th ASM Heat Treatment and Surface Engineering Conference, Jun 7-9, Gothenburg, Sweden, ASM International
16. Goldstein J.I., Moren A.E. (1978). Diffusion Modeling of the Carburization Process. Metallurgical and Materials Transactions, Vol. 9, 1515-1525.
17. Blazek K.E., Cost P.R. (1976). Carbon Diffusivity in Iron-Chromium Alloys. Transactions of the Japan Institute of Metals, Vol.17, 630-636.
18. Asimow R.M. (1964). Analysis of the Variation of the Diffusion Constant of Carbon in Austenite with Concentration, Transactions of AIME, Vol.230, 611-613
19. Stolar P., Prenosil B. (1984), Kinetics of Transfer of Carbon from Carburizing and Carbonitriding Atmospheres, Metallic Materials, Vol. 22, 348-353.
20. Munts V.A., Baskatov A.P. (1980), Rate of Carburizing of Steel, Metal Science and Heat Treatment, Vol.22, 358-360
21. Agren J. (1986). Rev. Expression for the Diffusivity of Carbon in Binary Fe-C Austenite, Scripta Metallurgica, Vol. 20, 1507-1510
22. Nayar A. (2000). *The Steel Handbook, Properties of Steel*, McGraw-Hill, New Delhi, 516.
23. Wisti M., Hingwe M. (1991). *Tempering of Steel*, ASM Handbook Vol.4, 291-299
24. Vatavuk J., Canale L.C.F. (2008). Steel Failures due to Tempering and Isothermal Heat Treatment. In Failure Analysis of Heat Treated Steel Components, ASM International, 285 – 309.

25. Canale L.C.F., Mesquita R.A., Totten G.E. (Eds.) (2008). In Failure Analysis of Heat Treated Steel Components, ASM International, Materials Park, OH, 285–310.
26. Speich G.R., Leslie W.C (1972). Tempering of Steel. Metal Translation. Vol.3 (5), 1043–1054.
27. Bain E.C., Paxton H.W. (1966). *Alloying Elements in Steel*. ASM International, Metals Park, OH.
28. Rossini N.S., Dassistia M., Benyounisb K.Y., Olabib A.G. (2012), Methods of Measuring Residual Stresses in Components, Material Design, vol.35.
29. Totten G., Howes M., Inoue T. (2002). Handbook of residual stress and deformation of steel. Materials Park, OH: ASM International. 189-208.
30. Lu J. (1996). Handbook of Measurement of Residual Stresses. Lilburn, GA: Fairmont Press.
31. Hızlı H., Gür C.H., (2015) Nondestructive Monitoring of the Effects of Carburizing on 19CrNi5H Steel by Magnetic Barkhausen Noise Method, 11th Int Conf on Barkhausen Noise & Micromagnetic Testing, 18-20 June, Kuşadası, CD Proc., No. 19
32. Schajer G. (2001). Practical Residual Stress Measurement Methods, A John Wiley & Sons, Ltd., Publication, 152-174.
33. ASTM E2860 – 12, Standard Test Method for Residual Stress Measurement by X-Ray Diffraction for Bearing Steels
34. Cullity B.D., (1977), Elements of X-ray Diffraction, 2nd ed., Addison Wesley, 447-476.
35. Hauk V. (1997), Structural and Residual Stress Analysis by Nondestructive Methods: Evaluation, Application, Assessment, Elsevier Science, 55.
36. Norton J.H, and Rosenthal D. (1944), Stress Measurement by X-ray Diffraction. Proceedings of the Society for Experimental Stress Analysis 1(2), 73-76.

37. Norton J.H. and Rosenthal D. (1944). Application of the X-ray Method of Stress Measurement to Problems Involving Residual Stress in Metals. Proceedings of the society for experimental stress analysis 1(2), 81-90.
38. Noyan I.C., Cohen J.B. (1987), Residual Stress Determination by Diffraction-Measurement and Interpretation, Springer, New York.
39. Murray C.E., Noyan I.C. (2010), Applied and Residual Stress Determination Using X-Ray Diffraction, Practical Residual Stress Measurement Methods, ed. G.S. Schajer, Wiley & Sons.
40. Barkhausen H. (1919), Two Phenomena Revealed with the Help of New Amplifiers, Phys.Z, vol.23, 225.
41. Cullity B.D., Graham C.D., (2008). *Introduction to Magnetic Materials*, 2nd Ed. by the Institute of Electrical and Electronics Engineers, Wiley Press.
42. Jiles D.C. (1991), *Introduction to Magnetism and Magnetic Materials*, Chapman & Hall, London.
43. Chikazumi S. (1964). *Physics of Magnetism*. Wiley, New York.
44. Shilling J.W., Houze G.L. (1974), Magnetic Properties and Domain Structure in Grain-oriented 3% Si-Fe. IEEE Transactions on Magnetics, 195-221.
45. Carey R., Isaac E.D. (1966), Magnetic Domains and Techniques for Their Observation. Academic Press, New York,
46. Neelkanta P.S. (1995). Handbook of Electromagnetic Materials: Monolithic and Composite Versions and Their Applications. CRC Press, Boca Raton, Florida.
47. Buttle D.J., Moorthy V., Shaw B., Edited: Lord J.D. (2006), *Measurement Good Practice Guide No.88 Determination of Residual Stresses by Magnetic Methods*.
48. Fiorillo F. (2005), *Characterization and Measurement of Magnetic Materials* (Electromagnetism), Academic Press , 25.
49. ASM Metals Handbook Vol.17 (1989), Nondestructive Evaluation and Quality Control, 9th edition, 317 – 320.

50. DeBlois R.W.(1958) Magnetization processes: Reversals and Losses. Journal of Applied Physics, Vol.29, 459-467.
51. Dobmann G., Kern R., Altpeter I., Theiner W. (1988) Quantitative Hardening-Depth Measurements up to 4mm by means of Micromagnetic Microstructure Multiparameter Analysis. Review of Progress in Quantitative Nondestructive Evaluation, Vol.7B, 1471-1475.
52. Cullity B.D., Graham C.D., (2008). *Introduction to Magnetic Materials*, 2nd Ed. by the Institute of Electrical and Electronics Engineers, Wiley Press. 320.
53. Lo C., Scruby C., Smith G. (2004). Dependences of Magnetic Barkhausen Emission and Magnetoacoustic Emission on the Microstructure of Pearlitic Steel. Philosophical Magazine, Vol. 84, 1821-1839.
54. Moorthy V., Vaidyanathan S., Jayakumar T., Raj B. (1997). Microstructural Characterization of Quenched and Tempered 0.2% Carbon Steel Using Magnetic Barkhausen Noise Analysis. Journal of Magnetism and Magnetic Materials, Vol. 171(1-2), 179-189
55. Zhu B. (2001). Non-linear, Irreversible Magnetization Processes in Magnetic Materials: Instrumentation, Measurements, Modeling and Application, Retrospective PhD.Theses and Dissertations in Iowa State University, 468.
56. Mix, P. (2005). *Introduction to Nondestructive Testing: A Training Guide* (2nd ed.), John Wiley & Sons.
57. Si P., Zhang Y., Qin S., Kong Y. (1992). Carbon Transfer Characteristics and Its Application on Gas Carburizing. Heat Treatment of Metals, 6, 51-55.
58. Munts V.A., Baskakov A.P. (1983). Mass Exchange in Carburization and Decarburization of Steel. Metal Science and Heat Treatment, Vol. 25(1-2), 98-102.
59. Yan M.F., Liu Z., Zu G. (2001). Study on Absorption and Transport of Carbon in Steel during Gas Carburizing with Rare-Earth Addition. Materials Chemistry and Physics. Vol. 70 (2), 242-244.

60. Collin R., Gunnarson S., Thulin D. (1972). Mathematical Model for Predicting Carbon Concentration Profiles of Gas-Carburized Steel. *Journal of the Iron and Steel Institute (London)*, Vol.210, 785-789.
61. Karabelchtchikova O., (2007). *Fundamentals of Mass Transfer in Gas Carburizing, Retrospective Theses and Dissertations in Worcester Polytechnic Institute, Metallurgical Transactions.*
62. Harris F.E. (1943), Case Depth: An Attempt at a Practical Definition, *Metal Progress*, Vol.44, 265-272.
63. Asi O., Can A.C. (2001). The comparison of the residual stresses between carburized and only quenched steels, *Journal of Engineering Sciences*, Vol. 201, 183-187.
64. Schroder R., Scholtes B., Macherauch E. (1984). Rechnerische und Röntgenographische Analyse der Eigenspannungsbildung in Abgeschreckten Stahlzylindern. *Hart.-Tech. Mitt.*, Vol.39, 280–292
65. Hildenwall, B., Ericsson T. (1980). Residual stresses in the soft pearlite layer of carburized steel. *J. Heat Treating*, Vol.1, 3-13
66. Coleman. W. S., M. Simpson (1957). Residual Stresses in Carburized Steels. In *Fatigue durability of carburized steel*. American Soc. Metals, Cleveland.
67. Knuuttila, M. (1982). Computer Controlled Residual Stress Analysis and Its Application to Carburized Steel. *Linköping Studies in Science and Technology*. Dissertation No. 81, Linköping.
68. Motoyama, M., H. Horisawa (1971). Residual Stress Measurements in Case Hardened Steels. SAE 710281, Soc. Automotive Eng.
69. Ericsson, T., S. Sjöström, M. Knuuttila, B. Hildenwall (1984). Predicting Residual Stresses in Cases. In D. E. Diesburg (Ed.) *Case-hardened steels: Microstructural and Residual Stress Effects*. Met. Soc. AIME, Warrendale.
70. Shea, M. (1983). Influence of Quenchant Temperature on the Surface Residual Stress and Impact Fracture of Carburized Steel. *Journal Of Heat Treating*, Vol. 3(1), 38-47

71. Vataavuk J., Zicari di Monte M., Couto A.A. The Effect of Core and Carburized Surface Microstructural Stability on Residual Stress Evolution during Tempering *Journal of ASTM International*, Vol. 6, No. 9.
72. Parrish, G. (1999), *Carburizing: Microstructures and Properties*, ASM International, Materials Park, Ohio, USA,.
73. Burnett JA (1985), Prediction of Stress History in Carburized and Quenched Steel Cylinders, *Material Science and Technology*, Vol. 1, 863–871
74. Sorsa, A., Leiviskä, K., Santa-aho, S., Lepistö, T. (2012). Quantitative Prediction of Residual Stress and Hardness in Case-hardened Steel Based on the Barkhausen Noise Measurement. *NDT & E International*, Vol. 46, 100-106.
75. Savas S., Gür C.H. (2010), Monitoring Variation of Surface Residual Stresses in the Shot Peened Steel Components by Magnetic Barkhausen Noise Method, *INSIGHT – J British Inst. of NDT*, Vol.52, 672-677.
76. Suominen, L., Tiitto K. (1994), Use of X-Ray Diffraction and Barkhausen Noise for the Evaluation of Stresses in Shot Peening, *Proc. of 4th Int. Conf. on Residual Stresses*, Baltimore-USA, 443-448.
77. Saquet, O., Chicois, J. ,Vincent, A. (1999), Barkhausen Noise from Plain Carbon Steels: Analysis of the Influence of Microstructure. *Materials Science and Engineering A*, Vol.269, 73-82.
78. Hug A, Kleber X, Merlin J, Petitgand H. (2005), Use of Magnetic Barkhausen Noise Measurements for Multi-phase Steels Characterization. In: *Proceedings of the 5th International Conference on Barkhausen Noise and Micromagnetic Testing*, 37–45.
79. Gupta H, Zhang M, Parakka A.P. (1997). Barkhausen Effect in Ground Steel. *Acta Metal*, Vol.45, 21.
80. Thompson S.M, Tanner B.K (1993). The Magnetic Properties of Pearlitic Steels as a Function of Carbon Content. *Magnetic Material*, Vol.123, 83–98.
81. Neslusan M., Hrabovská T., Čilliková M., Mičietová A. (2015). Monitoring of Hard Milled Surfaces via Barkhausen Noise Technique. *The Manufacturing*

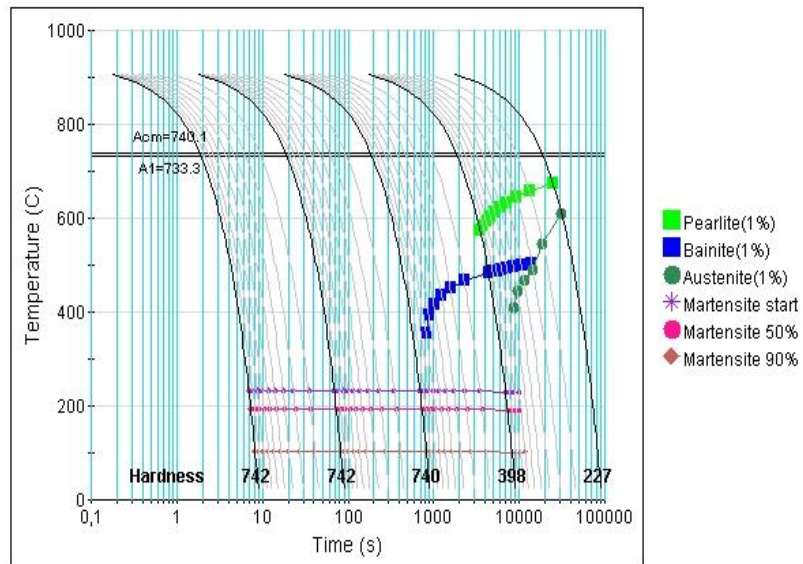
- Engineering Society International Conference, MESIC. *Procedia Engineering* Vol.132 , 472 – 479.
82. Hajko V, Potocký L., Zentko A. (1982). *Magnetization Processes*, ALFA, Bratislava.
83. Sipahi L. (1994). Effects of Creep Damage, Shot Peening, and Case Hardening on Magnetic Barkhausen Noise Analysis. *IEEE Transactions on Magnetics*, Vol.30, 4830–4832.
84. Santa-aho S., Vippola M., Lepistö T., Lindgren M. (2009). Characterization of Case Hardened Gear Steel by Multiparameter Barkhausen Noise Measurements. *Insight - Non-Destructive Testing and Condition Monitoring*, Vol. 51, 212–216.
85. Kinser E., Lo C., Barsic A., Jiles D. (2005). Modeling Microstructural Effects on Barkhausen Emission in Surface-modified Magnetic Materials. *IEEE Transactions on Magnetics*, Vol. 41, 3292–3294.
86. Mészáros I., Szabó P. (2005). Complex Magnetic and Microstructural Investigation of Duplex Stainless Steel. *NDT & E International*, Vol. 38, 517–521.
87. Stewart D., Stevens K. , Kaiser A. (2004). Magnetic Barkhausen Noise Analysis of Stress in Steel. *Current Applied Physics*, Vol. 4, 308–311
88. Jagadish C., Clapham L., Atherton D. (1990). Influence of Uniaxial Elastic Stress on Power Spectrum and Pulse Height Distribution of Surface Barkhausen Noise in Pipeline Steel. *IEEE Transactions on Magnetics*, Vol. 26, 1160–1163.
89. Davut, K., Gür, C.H. (2007). Monitoring the Microstructural Changes During Tempering of Quenched SAE 5140 Steel by Magnetic Barkhausen Noise, *Journal of Nondestructive Evaluation*, Vol.26, 107-113.
90. Blaow, M., Evans J.T., Shaw, B.A. (2007), The Effect of Microstructure and Applied Stress on Magnetic Barkhausen Emission in Induction Hardened Steel, *Journal of Materials Science*, Vol.42, 4364-4371.

91. Davut K., Bayramoglu S., Gürer G., Gür C.H. (2007). Nondestructive Characterization of Spheroidised AISI 1060 Steel by Magnetic Barkhausen Noise Measurements, Proceedings of 6th International Conference on Barkhausen Noise and Micromagnetics Testing, Valenciennes, France.
92. Joule J.P. (1842). On a New Class of Magnetic Forces. *Annals of Electricity, Magnetism, and Chemistry*, Vol. 8. 219–224
93. Villari E. (1865). Ueber die Aenderung des Magnetischen Moments, Welche der Zug und das Hindurchleiten Eines Galvanischen Stroms in Einem Stabe von Stahloder Eisen Hervorbringen, *Ann. Phys.*, Vol. 202, No. 9, 87–122.
94. Krause T.W., Pattantyus A., Atherton D.L. (1995). Investigation of Strain Dependent Magnetic Barkhausen Noise in Steel, *IEEE Trans. Magn.*, Vol. 31, No. 6, 3376–3378.
95. Silva Jr S.F., Mansur T.R. (2000), Determining Residual Stresses in Ferromagnetic Materials by Barkhausen Noise Measurement. In: 15th WCNDT Roma.
96. Wojtas A., Suominen L., Shaw B., Evans J. (1998). Detection of Thermal Damage in Steel Components after Grinding Using the Magnetic Barkhausen Noise Method, *NDT.net*, Vol.3.
97. Sorsa A., Santa-aho S., Vippola M., Lepisto T., Leiviska K.,(2014), Utilization of Frequency-domain Information of Barkhausen Noise Signal in Quantitative Prediction of Material Properties, in *AIP Conference Proceedings*, Vol. 1256, 1256–1263.
98. ISO 2639 Standard Test Method for Determination and Verification of Case Depth by Microhardness Test.
99. Moore M.G., Evans W.P. (1958), Mathematical Correction for Stress in Removed Layers in X-Ray Diffraction Residual Stress Analysis, *SAE Trans.*, Vol. 66.
100. Sikarskie D.L. (1967), On a Series Form of Correction to Stresses Measured Using X-ray Diffraction, *Trans. Metal Soc. AIME*, Vol. 239, 577-580.

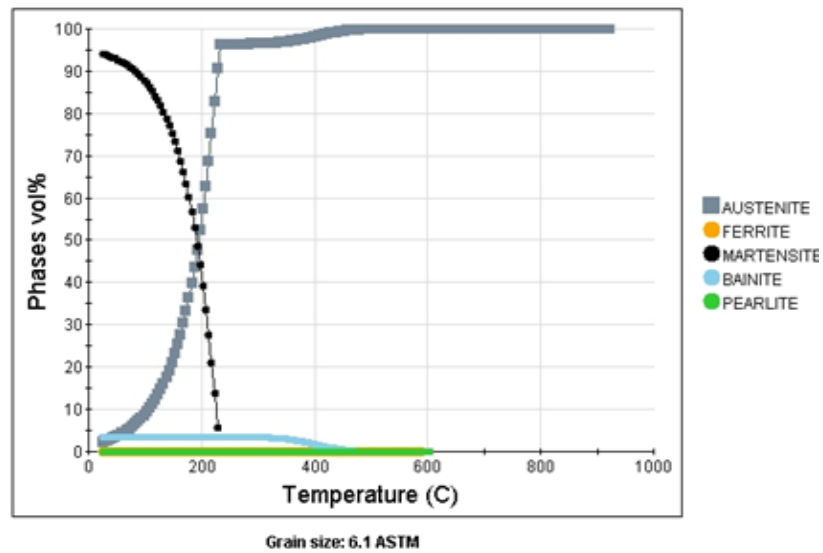
101. Ojala M., Saynajakangas S. (1972). New Electronic Grain Size Analyzer for Technical Steel. *Journal of Physics E, Sci. Instrum.*, Vol.5, 669-672.
102. Hızlı H. (2016), Nondestructive Monitoring of the Variations in Microstructure and Residual Stress in Carburized Steels, Master Theses, Dissertations in Middle East Technical University.
103. MatWeb - The Online Materials Information Resource. (n.d.). Retrieved from <http://www.matweb.com/search/DataSheet.aspx?MatGUID=bf59dbd8d6cc417db42d148dee7a0f12&ckck=1>

APPENDIX

A. CCT DIAGRAMS OBTAINED BY JMATPRO SOFTWARE



a



b

Figure A. 1 Simulated a) CCT diagram and b) phase % vol. distribution diagram of 5 hour-carburized specimens

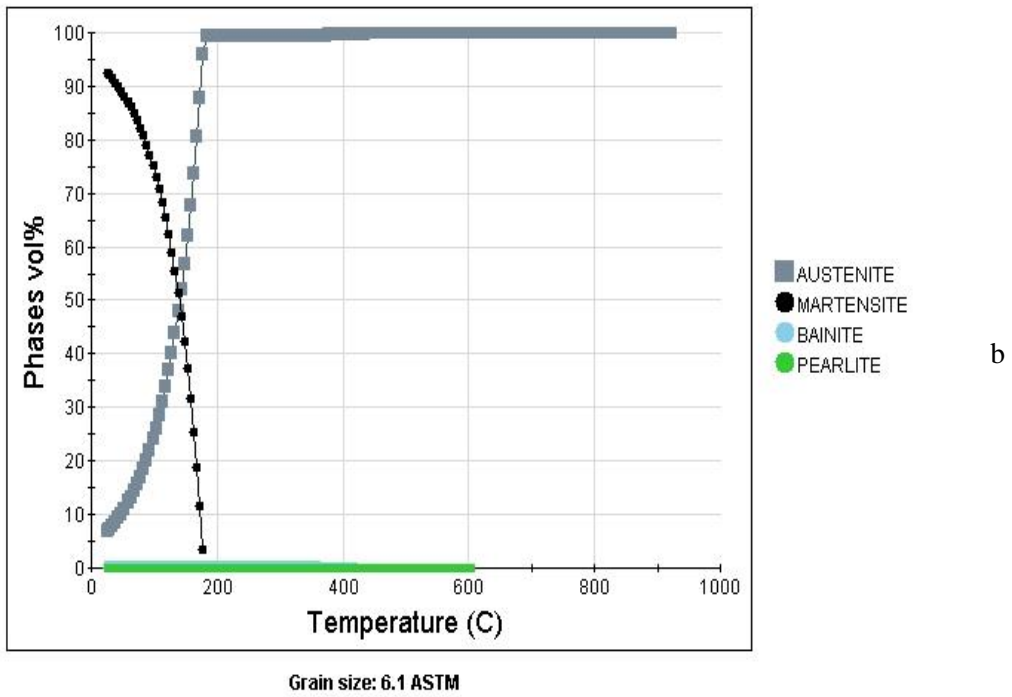
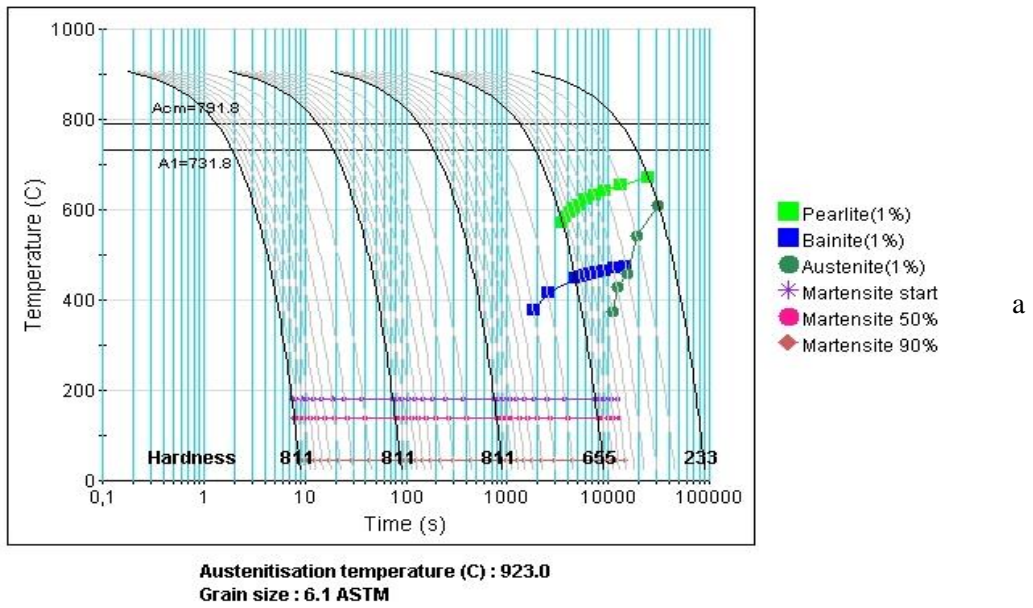
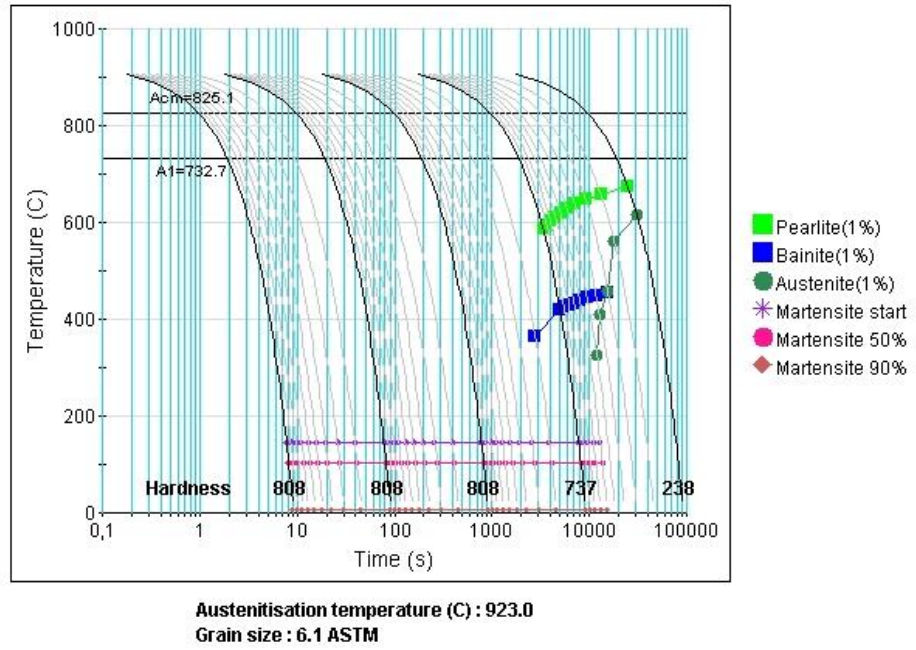
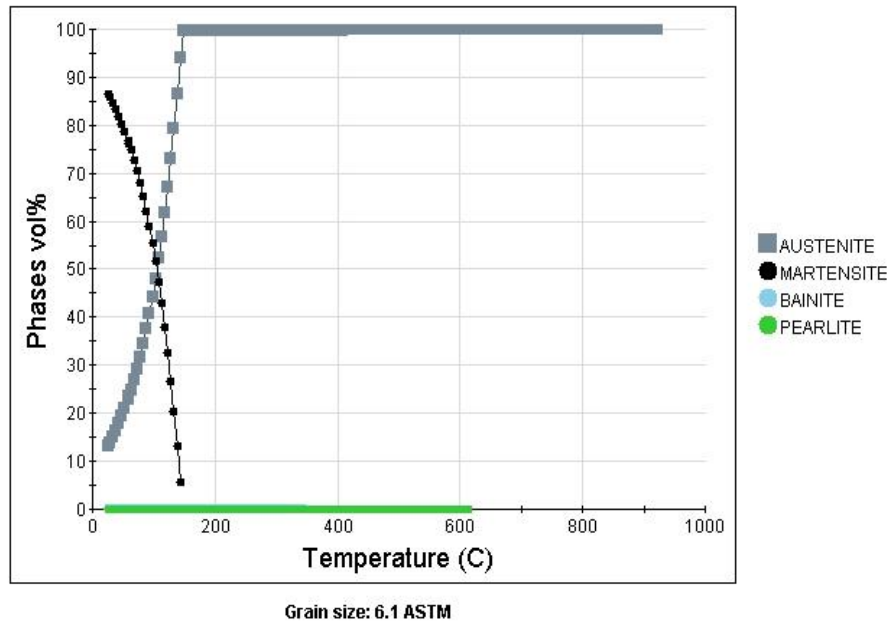


Figure A. 2 Simulated a) CCT diagram and b) phase % vol. distribution diagram of 9 hours-carburized specimens



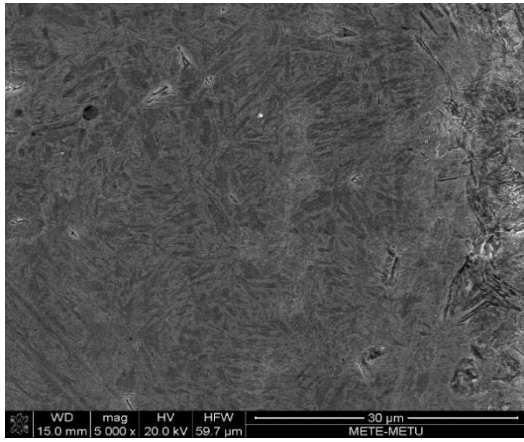
a



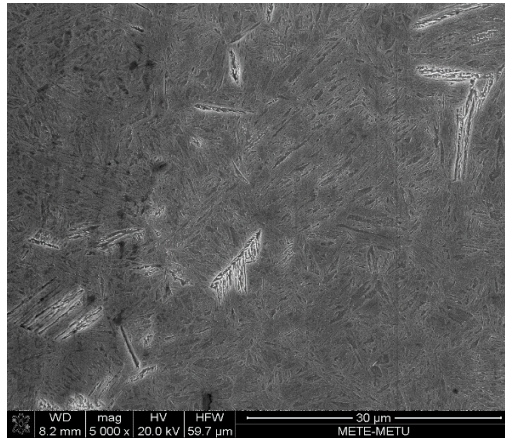
b

Figure A. 3 Simulated a) CCT diagram and b) phase % vol. distribution diagram of 12 hours-carburized specimens

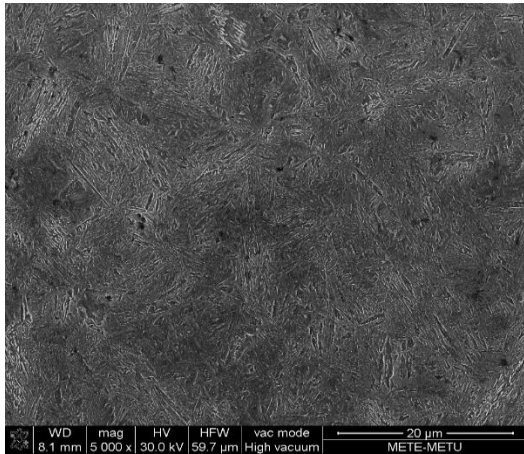
B. SCANNING ELECTRON MICROSCOPE IMAGES



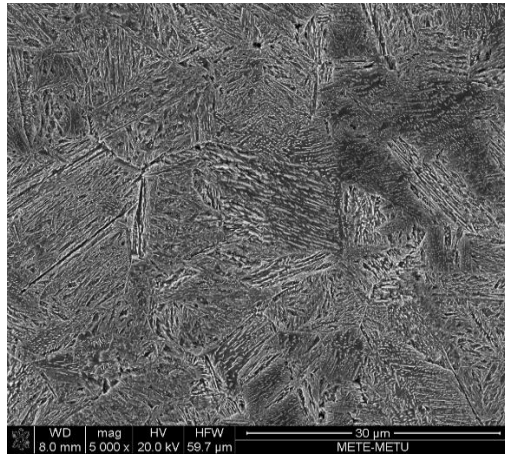
a) C0T0(case)



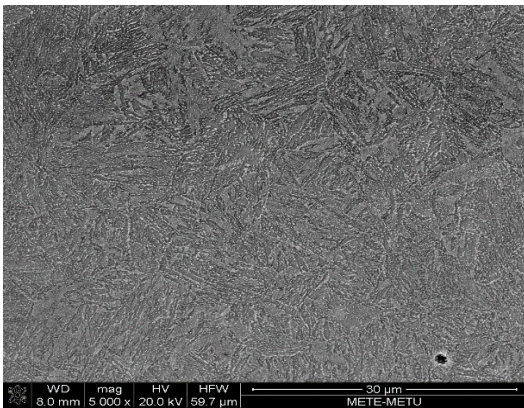
b) C05T180(case)



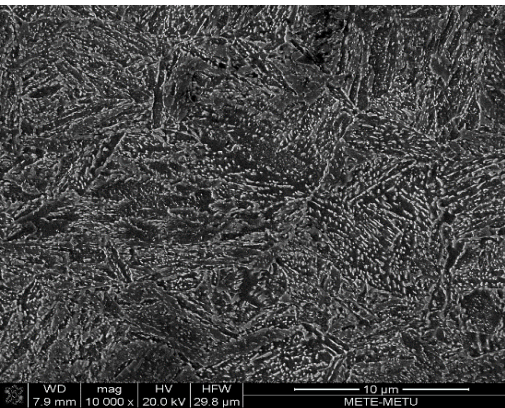
c) C05T240(case)



d) C05T240(core)

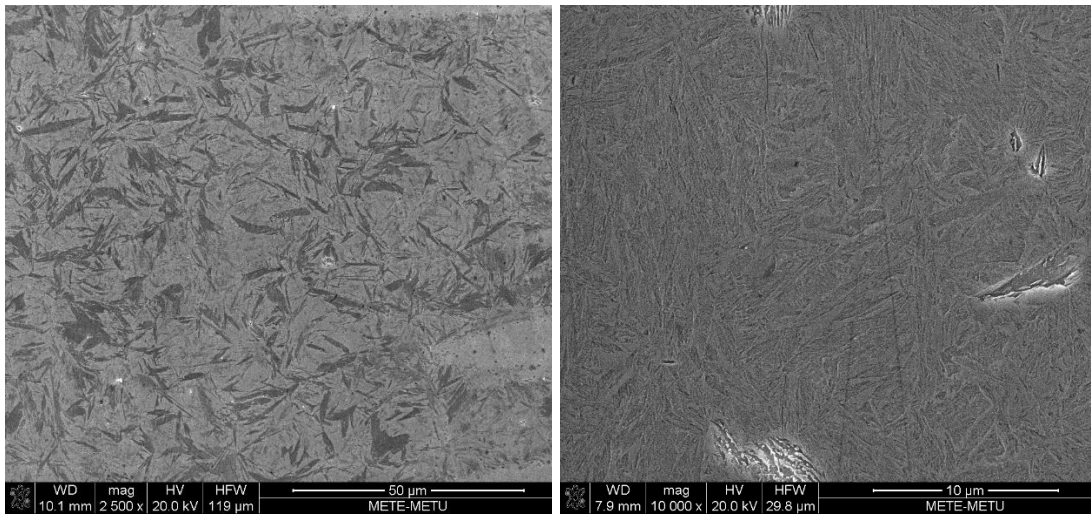


e) C05T600(case)



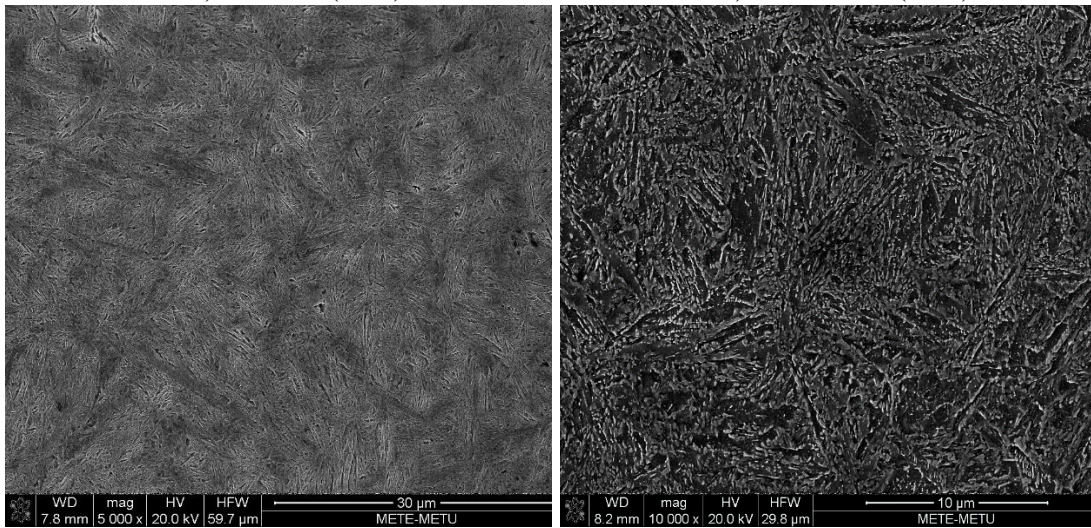
f) C05T600(core)

Figure B 1 SEM micrographs of carburized samples (900°C/5hrs) that were tempered at different temperature for 3 hrs.



a) C09T0(case)

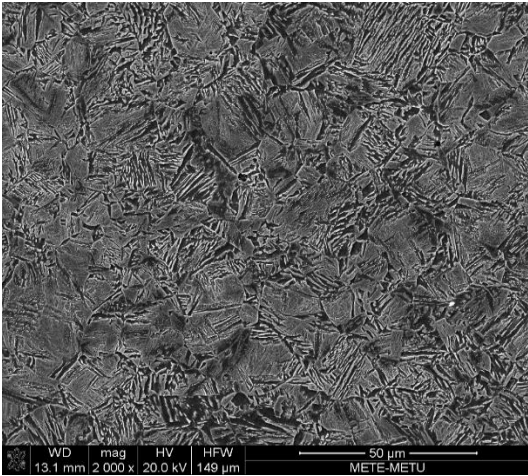
b) C09T180 (case)



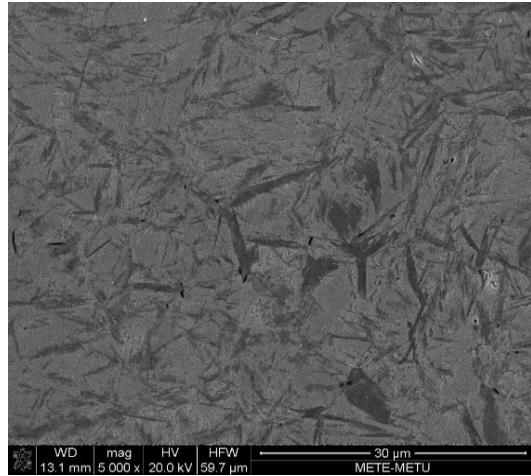
c) C09T240 (case)

d) C09T600 (case)

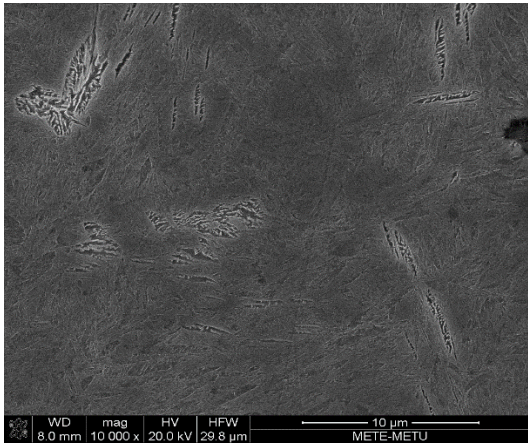
Figure B 2 SEM micrographs of carburized samples (900°C/9hrs) that were tempered at different temperature for 3 hrs.



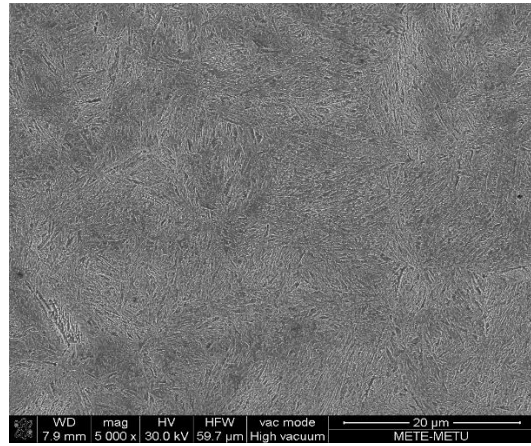
a) C12T0(core)



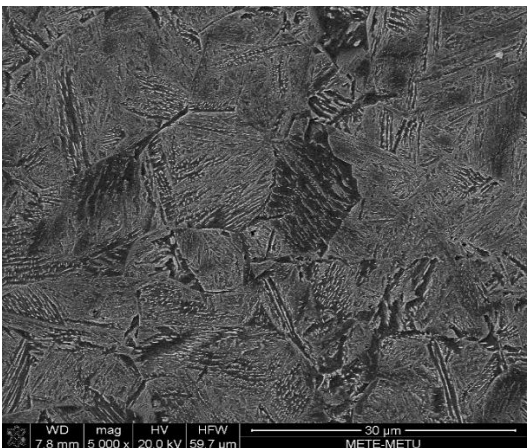
b) C12T10 (case)



c) C12T180 (case)



d) C12T240 (case)



e) C12T240 (core)

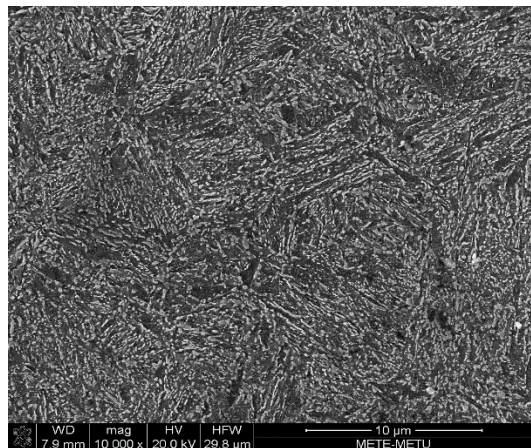


Figure B 3 SEM micrographs of carburized samples (900°C/12hrs) that were tempered at different temperature for 3 hrs.

C. CORRELATION AMONG RMS, HARDNESS, MBN AND RESIDUAL STRESS

After calculating the residual stress values obtained from MBN method, two correlation were constructed for the carburized SAE/AISI 8620 steel. First, RMS values and hardness values were correlated. The correlation graph is shown in Figure C.1. Data points were separated with respect to tempering conditions. Best linear curve is fitted by considering all data. The R^2 value is calculated as 0,90. It is observed from the correlation that higher R^2 value is obtained if the best linear curve is fitted for each tempering group.

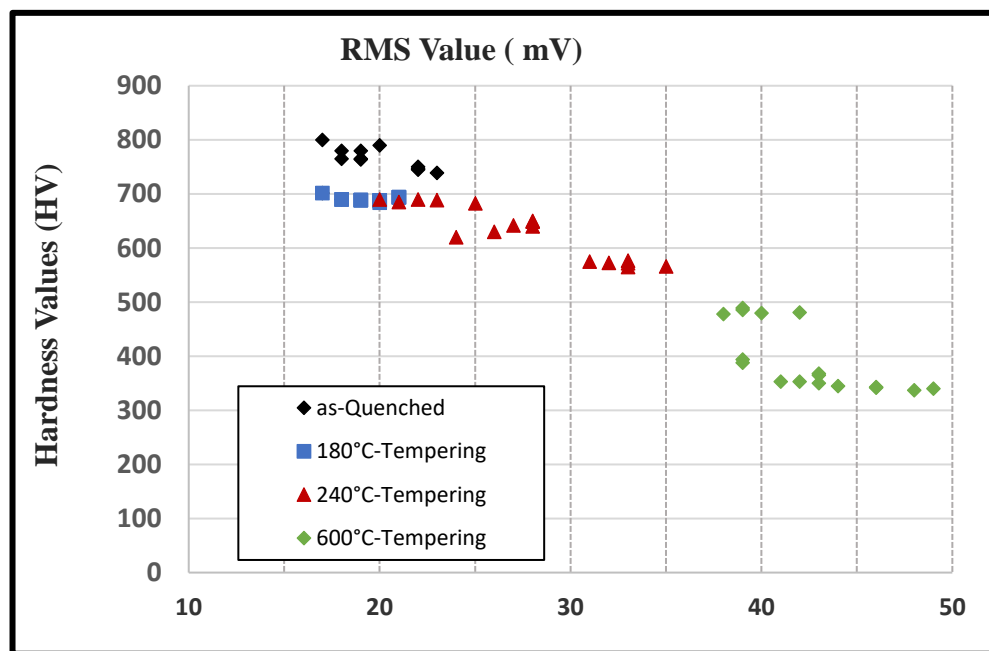


Figure C 1 Correlation between relative RMS values of MBN measurements and Hardness values taken from the same position

The other correlation is calculated between RMS values and calculated MBN residual stress values. The R^2 factor, i.e, correlation goodness, is relatively lower than that of the first correlation; 0,85. However, each tempering group shows the higher similarity.

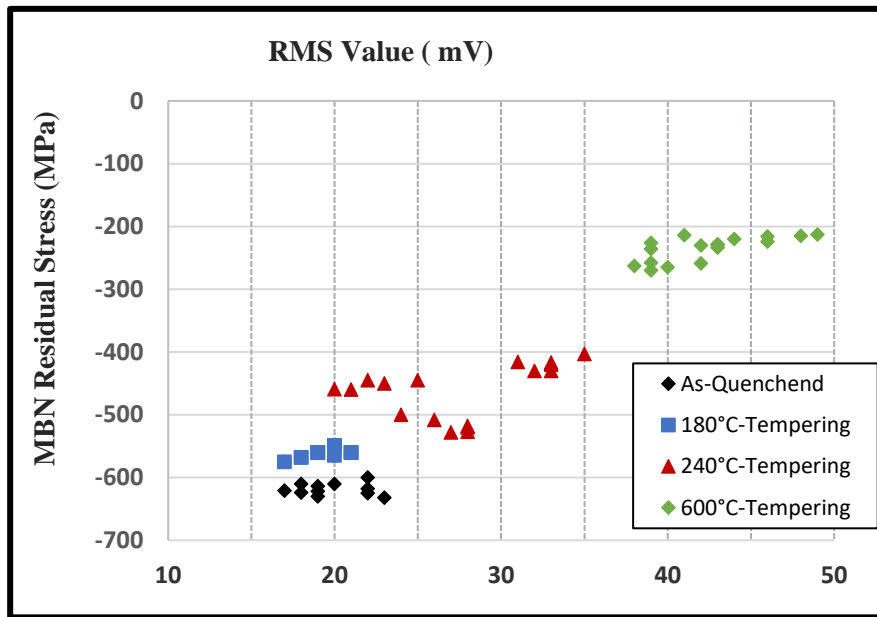


Figure C 2 Correlation between relative RMS values of MBN Residual Stress measurements taken from the same position

D. CALCULATION OF MAGNETIC PERMEABILITY AND INFORMATION DEPTH OF MBN MEASUREMENTS

Magnetic permeability of normalized and carburized specimens were measured in order to analyze frequency and corresponded the skin depth. Measurements were done by using Cryogenic Limited PPMS in METU Central Laboratory. From the material database software [103], conductivities were taken as 4.27×10^6 and 5.56×10^6 for normalized and carburized specimens, respectively. By using Eq. 13, the penetration depth of specimens were calculated. They are shown in the Table D 1.

Table D 1 Electrical and magnetic properties of normalized and carburized (900°C/12 hrs) AISI/SAE 8620 steel specimens

	Normalized	Carburized (12h)
Relative permeability (μ_r)	110	50
Conductivity ($\text{ohm}^{-1} \cdot \text{m}^{-1}$)	4.27×10^6 [103]	5.56×10^6 [103]
Excitation frequency (Hz)	125	125
Max. decrease in amplitude (kHz)	20	80
Penetration Depth (μm)	164	107